GEORG-AUGUST-UNIVERSITÄT
GÖTTINGEN

Fakultät für
Physik

Master's Thesis

Wiederinbetriebnahme des ATLAS Diamond Beam Monitors

Recommissioning of the ATLAS Diamond Beam Monitor

prepared by

Ben Brüers

from Oldenburg

at the II. Physikalisches Institut

Thesis number:	II.Physik-UniGö-MSc-2018/01
Thesis period:	4th August 2017 until 2nd February 2018
First referee:	Prof. Dr. Arnulf Quadt
Second referee:	Priv.Doz. Dr. Jörn Große-Knetter

Abstract

Der Atlas Diamond Beam Monitor (DBM) ist ein Teleskoptracker, welcher im Inneren des Atlas Experiments installiert ist. Er verwendet pixilierte Diamant- und Siliziumsensoren. Ziele des DBM sind Luminositäts- und Strahluntergrundmessungen. Kurz nach der ersten Inbetriebnahme 2015 konnten 11 der 24 Detektormodule nicht mehr betrieben werden. In dieser Arbeit werden einige mögliche Gründe hierfür untersucht. Nach der Installation von Sicherheitsmechanismen, um weitere Ausfälle zu verhindern, wurde der DBM 2017 wieder in Betrieb genommen. Diese Arbeit widmet sich der Wiederinbetriebnahme des DBM im Atlas Detektor und des DBM Testaufbaus, welcher sich in einem oberirdischen Labor am Cern befindet und seit 2016 funktionsunfähig war. Zudem werden die Ergebnisse des DBM Betriebs im Jahr 2017 vorgestellt.

Stichwörter: Pixeldetektoren, Diamant, Diamond Beam Monitor, DBM, Wiederinbetriebnahme, Atlas Experiment, Teilchenphysik, LHC, CERN, Masterarbeit

Abstract

The Atlas Diamond Beam Monitor (DBM) is a telescope tracker installed inside of the Atlas experiment. The DBM uses diamond and Silicon pixel detectors. Goals of the DBM are luminosity and beam background measurements. Shortly after initial commissioning in 2015, 11 of the 24 detector modules could not be operated any more. Some of the possible reasons why are studied in this thesis. After installation of safety mechanisms to prevent further module failures, the DBM was recommissioned in 2017. This thesis discusses the recommissioning of the DBM in Atlas and of the DBM testsetup, which is located in a surface lab at Cern and was not functioning any more as from 2016. The results of operation in 2017 are presented.

Keywords: Pixel detectors, Diamond, Diamond Beam Monitor, DBM, Recommissioning, Atlas experiment, Particle Physics, LHC, CERN, Master's thesis

Contents

1. Introduction

The questions of where humanity comes from, what its goal and task is, have always been concerning people. Closely related is the question what the world is made of, how it functions and how it drives humans. Physics addresses these questions. Ancient Greeks, with their idea of *atomos*, were probably the first to claim that the world is made of small fundamental building blocks, constructing all kinds of matter. Throughout history, this idea was more and more followed up. At first, the different chemical elements were classified. Atoms were found to consist of electrons and a nucleus, which is made of protons and neutrons. Studies of the protons and neutrons showed that they have a substructure and are made of quarks. It seems that the closer one looks, the more one sees.

With the advent of Quantum Mechanics, the idea of locatable particles began to totter, but it was soon understood that a particle describes an object that is point-like and a wave at the same time. Based on this idea, *Quantum Field Theories* were developed to predict the behaviour of quantised fields. The *Standard Model of Particle Physics* aims at describing all of the fundamental particles and their interactions in the universe by such fields. It is introduced in Chapter 2. Many predictions of the Standard Model have been verified and candidates for all fundamental particles predicted by it have been found. Yet, the Standard Model fails to describe some of the phenomena observed in the universe. It does not describe for example, why there is so much more matter than antimatter, nor does it describe *Dark Matter* or *Dark Energy*, which are fundamental concepts in cosmology. Several extensions of the Standard Model exist which try to overcome at least some of the shortcomings.

The ATLAS experiment's goal is to study the Standard Model and possible extensions experimentally. To do so, it detects particles resulting from collisions of protons at centre-of-mass energies of up to 13 TeV, provided by the *Large Hadron Collider*. The ATLAS detector is composed of several sub-detectors and presented in Chapter 4. One of the sub-detectors is the *Diamond Beam Monitor* (DBM). Its primary goal is high resolution determination of the luminosity, which then allows to calculate precise cross-sections of particle interactions. Secondary goal of the DBM are beam background measurements.

The DBM consists of eight telescopes, which are installed evenly on both sides of the ATLAS detector. Each telescope is made of three pixel detector chips and as sensor material 18 times diamond and six times Silicon are used. The basics of pixel detectors are explained in Chapter 3. The telescopes allow for tracking of particles and their tilt towards the interaction point simplifies the determination of signal and background for the proposed measurements.

Shortly after initial commissioning in 2015, 11 of the 24 pixel detector chips were not communicating any more. Possible reasons are different failure scenarios of the 25 µm thick, bare Aluminium wires, called *wirebonds*. Studies concerning these failures are discussed in Chapter 7. Wirebonds are used to connect the pixel detector chips to further read-out components. After safety mechanisms to prevent breaking wirebonds had been installed, it was decided to recommission the DBM. However, issues in the powering and data acquisition infrastructure prevented this. Debugging was supposed to be carried out on the DBM test setup, located in a surface lab at CERN, which was defective since 2016, though. The DBM setup and its status at the beginning of 2017 are described in more detail in Chapter 5.

This thesis is about the recommissioning of the DBM and the DBM test setup. The recommissioning was carried out during the *End-of-Year Extended Technical Stop* (EYETS) of the Large Hadron Collider. The EYETS was beneficial for recommissioning, as the magnetic field of the ATLAS detector was switched off, minimising the danger of breaking wirebonds. Recommissioning of the DBM and the DBM test setup are explained in Chapter 6. Operation of the DBM in 2017 is also presented. Finally, the results are summarised in Chapter 8.

2. The Standard Model of Particle Physics

2.1. Overview

The *Standard Model of Particle Physics* (SM) is a model aiming at a description of the fundamental properties of matter. It explains matter as consisting of several particles, which interact with each other. Currently, it incorporates three of the four known fundamental forces: the electric, weak and strong force, but not the gravitational one. In the SM, forces are mediated by particles, the *bosons*, which have integer spin. The force particles interact with the so-called *fermions*, which are half-integer spin particles. Some of the force mediators can also interact among each other.

Mathematically, the SM is realised as a *Quantum Field Theory* (QFT) which is Poincaré (i.e. translation and Lorentz-group) and local gauge invariant with gauge group $U(1)_Y \times SU(2)_L \times SU(3)_C$. The gauge groups describe particle interactions. Therefore, they constrain the number of bosons. Interactions concerned with the $U(1)_Y \times SU(2)_L$ part are called electroweak and interactions related to the $SU(3)_C$ are called strong. The electroweak interactions combine the electromagnetic and the weak force. The subscripts on the groups relate to properties of the interactions. The Y indicates the quantification of the $U(1)_Y$-interactions in terms of the quantum number Y, the *hypercharge*. It can be decomposed into $Y = 2(q - T_3)$, with q the electric charge of a particle and T_3 the third weak isospin component. The latter is also relevant for interactions described by the $SU(2)_L$. The subscript L on the $SU(2)_L$ indicates "left-handedness" meaning that only left-handed fermions can be involved in interactions with the associated bosons. The C on the $SU(3)_C$ stands for the necessity of a non-zero quantum number *colour charge* for particles interacting strongly.

The particles of the SM are summarised in Figure 2.1. The fermions of the SM are given by 6 quarks (u, d, c, s, t, b), 3 charged leptons (e, μ, τ) of charge $q = -1$ (in multiples of the positron charge) and 3 electrically neutral leptons, the neutrinos $(\nu_e, \nu_\mu, \nu_\tau)$. The bosons are given by 3 weak force mediators (the W^+, W^- and Z^0-boson), one electromagnetic (γ,

the photon) and one strong force carrier (g, the gluon). All fermions carry weak isospin and can be divided into up-type fermions with weak isospin $T_3 = +\frac{1}{2}$ and down-type fermions with weak isospin $T_3 = -\frac{1}{2}$. The up-type quarks carry an electric charge of $q = +\frac{2}{3}$ and the down-type quarks have a charge of $q = -\frac{1}{3}$. The quarks are the only fermions that carry a colour charge, which is not fixed for a quark and conventionally can be either red, green or blue. To each of the fermions an antifermion of opposite charge is assigned. For the bosons, the weak isospin and charge of the $W^{\pm}$ is $T_3 = \pm 1$ and $q = \pm 1$. The Z^0, γ and g carry neither charge, nor isospin. Gluons are the only bosons that carry colour.

Because all fermions have a weak isospin different from zero, they all have the ability to interact via the weak force. The charged fermions can further interact electromagnetically and the quarks can participate in the strong interaction. By these constraints the neutrinos will only interact weakly. The interaction of gauge bosons among each other, as well as couplings of same type bosons, such as triple or quartic gauge couplings, are possible. All massive particles of the SM participate in interactions with the Higgs boson and actually acquire their mass through the Higgs field within the formalism of the SM.

2.2. The electroweak interactions

The electroweak interactions are described by the *Glashow-Weinberg-Salam (GWS) theory* [1–3]. It concatenates the electromagnetic and weak interactions, which were before known as distinct phenomena. In the GWS-theory, the massive gauge bosons of the SM, called vector bosons and the fermions acquire mass through the *Higgs mechanism*. It is necessary, as simple mass terms would violate the local gauge invariance requirement. It is attributed to Brout and Englert [4], Higgs [5] and Guralnik, Kibble and Hagen [6], based on the previous work of Goldstone [7] and Nambu [8]. In principle, the Higgs mechanism is the Goldstone theorem for local gauge invariance. It leads to the introduction of an additional field, the Higgs field, which has a vacuum expectation value $v \neq 0$. The field breaks gauge symmetry spontaneously, in the sense that while the Lagrangian obeys it, the vacuum state does not. Particles interacting with the Higgs field acquire a mass, which is proportional to the coupling constant of the particle to the field, without violating gauge symmetries.

Excitations of the Higgs field should be seen as a massive particle with spin 0, the Higgs boson. A particle potentially being the Higgs boson was discovered in 2012 by the ATLAS and CMS experiments [9, 10].

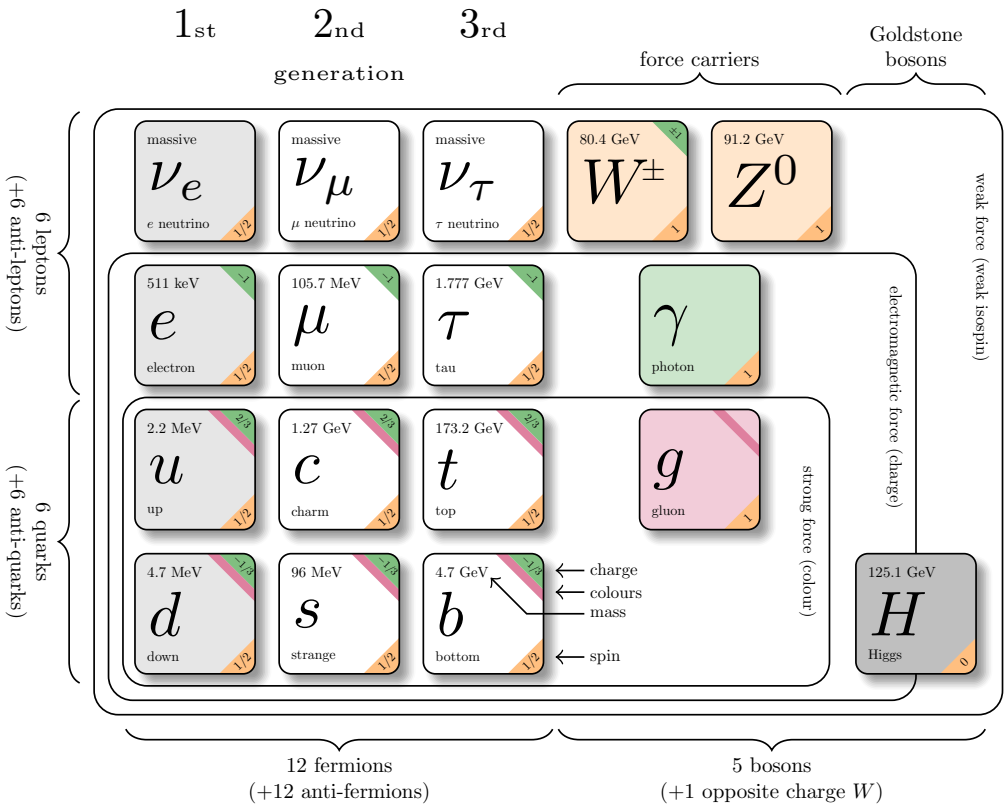

Figure 2.1.: The particles involved in the SM[1].

2.2.1. Coupling structure in the electro-weak force

QED

The QFT of electromagnetics is called *Quantum Electro Dynamics* (QED). QED is incorporated into the GWS-theory. It is parity conserving (everything is the same under reversal of spatial coordinates) and the coupling strength is proportional to the charge q of a particle. The force mediator of QED is the photon and as it is not charged, it does not allow for any photon self-couplings. This is reflected by QED being an Abelian theory.

The weak charged force

For the weak charged force, experiments by Wu [11] and Goldhaber [12] showed that parity is *maximally* violated. Hence, the weak charged force only interacts with (right)

[1]Copyright: Graphics adapted from Carsten Burgard, CC BY 2.5, `http://www.texample.net/tikz/examples/model-physics/`, accessed: 29.01.2018, 11:00 am.

left handed chiral (anti-)particles. Chirality is the eigenvalue of γ^5. In fact, all fields of the $SU(2)_L$ couple to (right) left handed chiral (anti-)particles. The observations are reflected in the weak coupling by the structure of the coupling to fermions being vector - axialvector (V-A) like. Since the $W^{\pm}$ changes the isospin by ± 1, the left-handed particles are arranged in doublets for the weak charged interaction

$$\begin{pmatrix} \nu_e \\ e \end{pmatrix}_L, \begin{pmatrix} \nu_\mu \\ \mu \end{pmatrix}_L, \begin{pmatrix} \nu_\tau \\ \tau \end{pmatrix}_L, \begin{pmatrix} u \\ d \end{pmatrix}_L, \begin{pmatrix} c \\ s \end{pmatrix}_L, \begin{pmatrix} t \\ b \end{pmatrix}_L .$$

Right handed particles form singlets $(e)_R, (\mu)_R, (\tau)_R, (u)_R, (d)_R, (c)_R, (s)_R, (t)_R, (b)_R$. Note that there are no right handed neutrino singlets, as they have not been observed, yet.

All leptons interact in the charged weak interaction within one generation. For quarks, this is not true. Their generation mixing was observed, for example in kaon decays $K_s \to \pi_0\pi_0$ [13]. This is implemented by not declaring the quark mass eigenstates as the charged weak quark eigenstates, but linear combinations of the former. The linear combinations are described by the Cabibbo-Kobayashi-Maskawa (CKM) matrix [14, 15]. The CKM matrix is unitary and can be described by three mixing angles and a complex phase. The complex phase relates to the CP-violation in the charged weak interaction, which was discovered in 1964 by Christenson, Cronin and Fitch [13]. The diagonal entries (in-generation-mixing) are the largest in magnitude [16].

The neutral weak force

In contrast to the $W^{\pm}$, the coupling of the Z^0 is not maximally parity violating. While also carrying the V-A structure, it thus allows for interactions of left- and right-handed particles with a Z^0. For neutrinos, however, as the charge $q = 0$, this is not fulfilled and they can only interact with their left-handed chiral component.

2.3. The strong interaction

To each particle contributing to the strong interaction, a colour charge is assigned. The underlying gauge group is the $SU(3)_C$ and the corresponding QFT is called *Quantum Chromo Dynamics* (QCD). The eight generators of the $SU(3)_C$ are associated with eight gluons of different colour combinations. There are 6 fermions, the quarks, in QCD. Gluon self-interactions are possible in QCD, as gluons carry colour. Thus, QCD is not an Abelian gauge theory, in comparison to for example QED. The couplings in QED and QCD are also fundamentally different. While in QED, with rising distance of two charged particles,

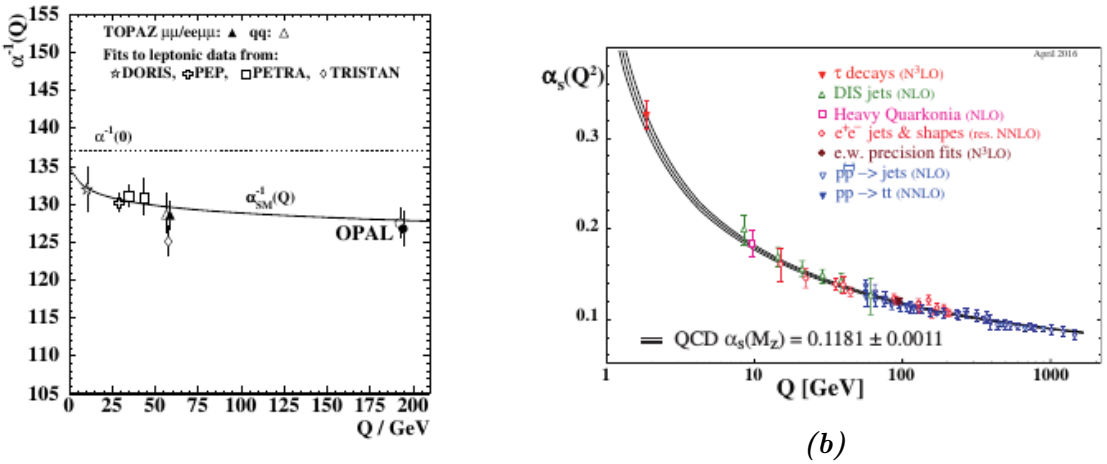

Figure 2.2.: (a) The inverse electromagnetic coupling constant [17]. (b) The strong coupling constant [16].

their force on each other decreases, this is the opposite in QCD. The (strong / QCD) force between two coloured particles is small at small distances and gets larger, when the distance increases. Formally, this results in a different energy dependence of the coupling constants α_{QED} and α_{QCD}, which are plotted in Figure 2.2. Here, the four-momentum square Q^2 describes the energy transfer of two scattering particles. The distance picture from before relates to the description in terms of Q^2, by understanding a larger energy transfer as smaller separation distance and vice versa.

From Figure 2.2, one sees that if Q^2 becomes small, then so does α_{QED}, while α_{QCD} becomes large. At small energy transfers or large distances of the colour charges, the coupling of QCD diverges. This is used to explain, why only colour neutral quark compound particles, but no colour charged quark compound particles have been observed. Colour neutral particles compound of colour charges are called *hadrons*. The non-observation of individual colour charges is denoted *colour confinement*.

Hadrons formed by two quarks are called *mesons* (for example π^0, $\pi^{\pm}$, ρ etc.) and those made out of three quarks are called *baryons* (for example the proton). *Tetraquarks* (four quark compounds) and *pentaquarks* (five quark compounds) have also recently been observed [18, 19]. The colour confinement can lead to multiple sprays of hadrons forming around an emerging quarks in particle collisions. These sprays are called *jets*.

The coupling α_{QCD} is small at large Q^2, and therefore processes can be handled perturbatively. This is called *asymptotic freedom*. At small Q^2, this perturbative treatment is however not possible, which led to the introduction of lattice QCD.

3. Pixel detectors

3.1. Energy loss of charged particles in matter

When traversing matter, charged particles lose energy. The average energy loss per penetration depth by excitation and ionisation is quantified by the so-called *Bethe-Bloch-formula*

$$\left\langle -\frac{\mathrm{d}E}{\mathrm{d}s} \right\rangle = 4\pi N_A r_e^2 m_e c^2 \cdot \rho \frac{Z}{A} \cdot \frac{z^2}{\beta^2} \left(\ln\left(\frac{2m_e c^2 \gamma^2 \beta^2}{I} \right) - \beta^2 - \frac{\delta}{2} \right). \tag{3.1}$$

Here N_A is the Avogadro constant, r_e the classical electron radius, ρ the density of the penetrated material, $\frac{Z}{A}$ the ratio of atomic to mass-number, z the charge of the incoming particle, I a constant characterising the ionisation behaviour of the penetrated material, δ a constant describing the absorption of the electric field of the nucleus of the penetrated material by its atomic electrons. Important properties of the penetrated material in this formula are ρ, $\frac{Z}{A}$, I, δ. The ratio $\frac{Z}{A}$ is about $\frac{1}{2}$ for most materials and I only enters logarithmically. Hence, by rewriting $\rho \mathrm{d}s = \mathrm{d}x$, an expression is obtained, which is approximately independent of the penetrated material. For the incoming particle, the most important parameters are velocity and charge. The higher the charge, the more energy is lost and the higher the velocity, the less energy is lost.

Besides the energy loss by excitation and ionisation, there are several other forms of energy loss, such as Bremsstrahlung. Taking all into account, the total energy loss results in what is shown in Figure 3.1. Here, the energy-loss per penetration depth of an anti-muon traversing copper is plotted against the product of velocity and the Lorentz-factor γ. The energy-loss rises rapidly at first, decreases proportionally with β^{-2} and reaches its minimum at around $\beta\gamma \simeq 3$. It then slightly rises and as from $\beta\gamma \simeq 1000$ rises rapidly. Until this point, the energy-loss is mainly given by excitation and ionisation. Beyond this point, which is called the critical energy E_c, the energy-loss is dominated by Bremsstrahlung.

For applications, one is usually interested in measuring all particles traversing a detector, in particular those with minimum energy-loss. Therefore, a detector needs to be

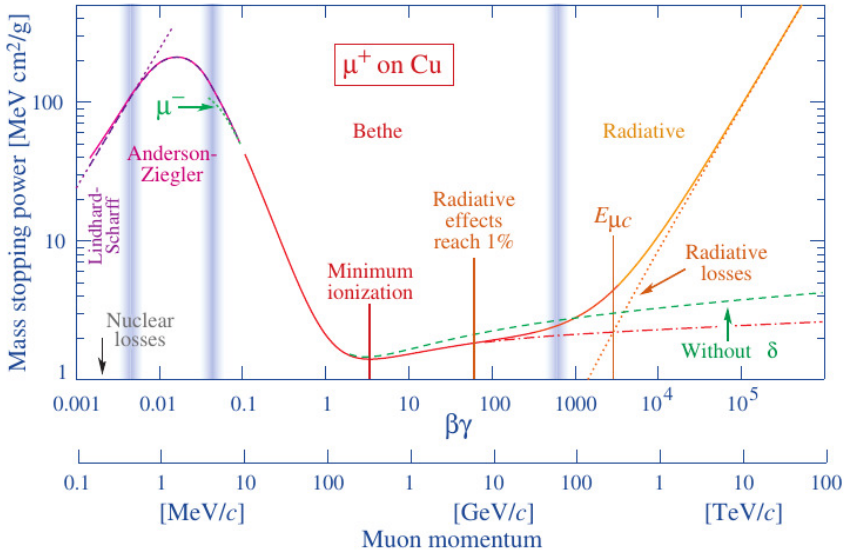

Figure 3.1.: The average energy-loss per penetration depth $\left\langle -\frac{\mathrm{d}E}{\mathrm{d}x} \right\rangle$ of an anti-muon traversing copper [16].

sensitive enough to measure these. The point of minimum energy-loss can be calculated using the Bethe-Bloch-formula.

3.2. Tracking performance

In a homogeneous magnetic field B a particle with charge q is bent on a circular orbit of radius R by the Lorentz force. If the particles penetrate N equally spaced detectors providing position information in the magnetic field, then the curvature $\kappa := \frac{q}{|q|}\frac{1}{R}$ can be calculated with standard deviation [20]

$$\sigma_\kappa = \frac{\sigma_{\text{res.}}}{L^2}\sqrt{\frac{720(N-1)^3}{(N-2)N(N+1)(N+2)}}. \tag{3.2}$$

Here $\sigma_{\text{res.}}$ quantifies the position resolution of the detectors. If they provide binary response and have a pitch of l, then $\sigma_{\text{res.}} = \frac{l}{\sqrt{12}}$. Binary response means that the possible signals of each position measurement unit are hit or no hit. The knowledge of κ allows to calculate the momentum of a particle in the plane of the magnetic field.

For detectors at colliders, the *pointing resolution* describes, how well a track can be extrapolated back to its origin vertex. It is mainly influenced by the position resolution and the amount of multiple scattering. Multiple scattering describes the scattering of

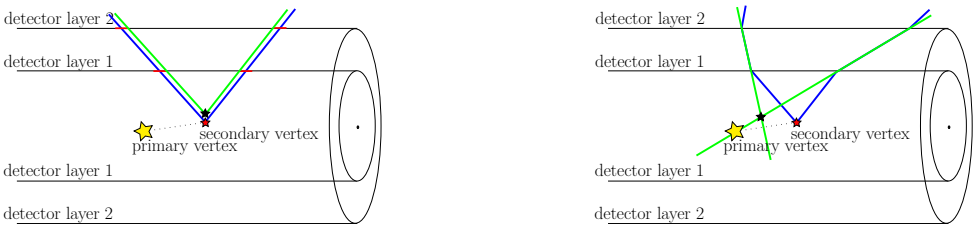

Figure 3.2.: The pointing resolution for the example of a secondary vertex reconstruction with a two layer detector. The influence of the position resolution can be seen in (a). Multiple scattering altering the reconstructed vertex is shown in (b). The actual secondary vertex is marked by a red star, the reconstructed secondary vertex by a black star.

charged particles in the coulomb fields of atomic nuclei of a penetrated material. The scattering leads to deflections, which alter the particle track and decrease the pointing resolution. The effect of the detector resolution and multiple scattering on the pointing resolution is shown in Figure 3.2.

Assume a simplified detector, consisting of two cylindrical measurement planes at radius r_1 and r_2 from the collision point. Let their position resolutions be σ_1 and σ_2, respectively. In absence of a magnetic field, if σ_{MS} is the uncertainty introduced by the multiple scattering, the pointing resolution can be calculated by

$$\sigma_p^2 = \left(\frac{r_1}{r_2 - r_1}\sigma_1\right)^2 + \left(\frac{r_2}{r_2 - r_1}\sigma_2\right)^2 + \sigma_{\mathrm{MS}}^2. \tag{3.3}$$

3.3. General working principle of pixel detectors

The general working principle of pixel detectors is the following: a charged particle penetrates a material, loses energy and thereby deposits charge. The charge induces a signal which is amplified and read out. The name *pixel detector* reflects that the detector is divided into a fine matrix, into *pixels*. The material in which charge is deposited is called the *sensitive material*, *active material* or *sensor*. Often, the sensor is made out of Silicon and amplification, signal modification and possibly digitisation is carried out by a separate electronics chip connected to the Silicon. Pixel detectors separating sensor and signal processing into multiple chips are called *hybrid* pixel detectors, pixel detectors combining them into one chip are called *monolithic* pixel detectors. Also diamond can be used as sensor material and focus will lie on hybrid pixel detectors in the following.

3.4. Silicon as sensor material

3.4.1. Semiconductors and the *np*-diode

Most pixel detectors use Silicon diodes as sensor material. Pure Silicon is a semiconductor, which means that it is a resistor at low and a conductor at high temperatures. Semiconductors are characterised by a band gap between the conductance band (the first empty band) and the valence band (the last filled band) of conventionally less than 4 eV. Silicon has a band gap of 1.12 eV at room temperature. If an electron moves from the valence to the conductance band in a semiconductor, there will be a *hole* in the valence and a free electron in the conductance band. Both are then available for charge transport. What is often used to describe a semiconductor is the so-called *Fermi-energy*, defined as the energy at which 50 % occupation can be found.

To increase the conductivity of a semiconductor, it can be doped. That means introducing impurities into the semiconductor, which typically have one more (donors) or one less (acceptors) valence electrons than the semiconductor atoms. Examples are Phosphorus as donor and Boron as acceptor for Silicon. The Fermi-energy is raised by the donors and lowered by the acceptors. Semiconductors doped with donors are called *n-type semiconductors* and semiconductors doped with acceptors are called *p-type semiconductors*.

One can also consider the combination of an n- and p-type semiconductor. It is assumed that the transition is abrupt. Due to the alignment of the Fermi energy between the two doped parts, a current of electrons and holes is formed close to the junction. Since these are then missing on either doped side, an electric field is generated, opposing the currents of holes and electrons. When the system is in equilibrium there will be a charge carrier free region of certain width around the junction, the so-called *depletion zone*. Because of its small net charge carrier concentration it is highly resistive. The combination of a p- and an n-doped semiconductor is called an *np-diode*.

3.4.2. The diode as a sensor

For now, the considered semiconductor will be Silicon. To build a pixel detector out of an *np*-diode, one applies a voltage across it. The potential difference U is chosen such that the potential is more negative at the p-doped and more positive at the n-doped side. Thereby, the depletion zone is going to be increased, as holes will be filled and the free electrons attracted by the positive potential. The voltage applied is called *bias voltage*.

An incoming particle now deposits energy in the *np*-diode. If this is large enough, electron-hole pairs can be formed. The average energy needed for an electron-hole pair to

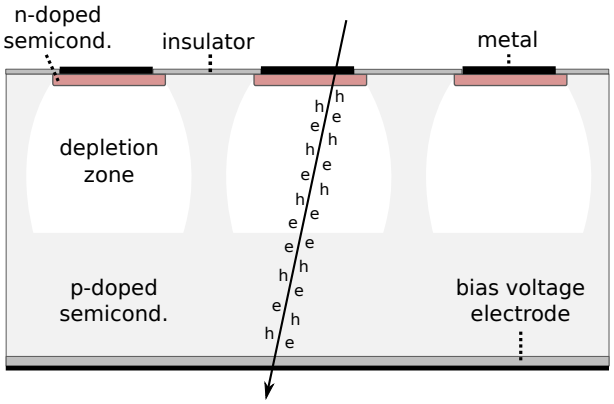

Figure 3.3.: Drawing of a realistic Silicon pixel sensor.

be formed in Silicon is 3.6 eV. It is larger than the band gap due to phonon excitations. In the depletion zone the electrons and holes are accelerated in opposite directions towards the electrodes. As described by the Shockley-Ramo theorem [21, 22] the motion of each charge carrier induces a current on either electrode which is proportional to the velocity of the charge carrier. Measuring the charge carrier induced current on one of the electrodes allows a measurement of the total charge deposited by a penetrating charged particle. Because the velocity of electrons is higher with respect to holes, their signal is more pronounced. Figure 3.3 shows a drawing of a realistic Silicon sensor, where electrons are used as signal generators.

Electron-hole pairs created outside of a depleted volume recombine and do not contribute to the signal.

For many pixel detector applications, one uses a lightly n-doped Silicon bulk, in which several highly n-doped pixels are implanted. Depletion is reached by strongly p doping the sensor side opposite of the pixels. Ideally, the diode is fully depleted, to have a large sensitive volume. The signal of induced electrons is read out at each n-pixel and further processed. This further processing is carried out by the *front-end* chip.

3.5. The front-end chip

The front-end chip carries out several steps. These are usually signal amplification, signal shaping and noise reduction, and often digitisation. The digitisation has the advantage that the signal can then be transferred loss-less. It has the potential disadvantage of information loss though. The circuit diagram of an example front-end chip pixel with charge-sensitive amplifier is shown in Figure 3.4. The sensor is simplified by the capacitor C_{det} here. The current induced by moving electrons/holes in the sensor first charges the

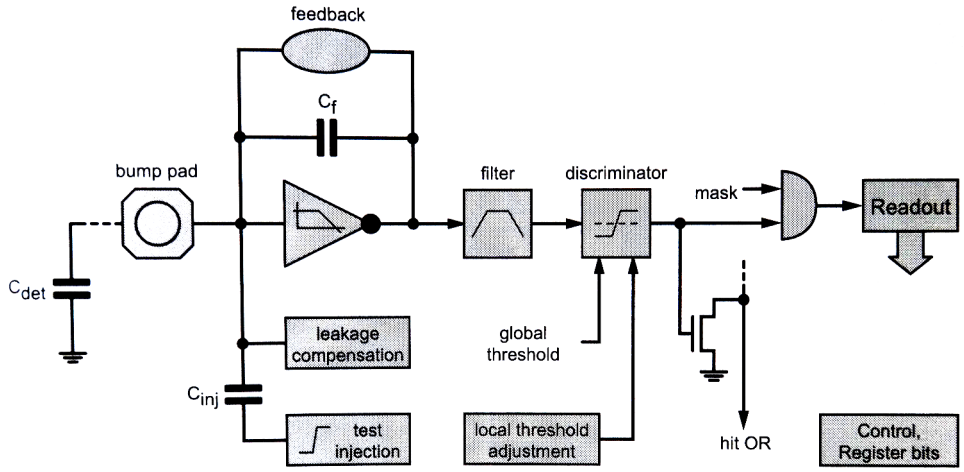

Figure 3.4.: Circuit diagram of an example front-end chip pixel with charge-sensitive amplifier (Copyright: [23]).

feed-back capacitor C_f. The voltage formed across C_f is then amplified. The resulting signal is shaped to reduce noise and then discriminated. The discriminator compares the input voltage to a reference threshold voltage. If the input voltage is above the threshold voltage, it outputs the digital signal 1, else it outputs 0. The discriminator digitises the signal and suppresses the noise floor.

Above C_f an oval labelled *feedback* can be seen. This stands generally for an electronic circuit discharging the feed-back capacitor. It is required to achieve differentiation of the signals from two subsequently penetrating particles within a certain time. Multiple implementations of the discharging circuit exist and here it is chosen to be a constant current source. From now on it is assumed that the charge time of C_f is small and that the discharge time of C_f by the constant current source is much smaller than the self-discharge time. The signal of the charge induced by a traversing particle then has a triangular shape at the output of the filter, as shown in the top of Figure 3.5a. Since the discharging of C_f is linear by the constant current, the discharge time is proportional to the signal height and hence the deposited charge. Concerning the discriminator, this means that the time a signal is above the threshold will be proportional to the initial signal height. Therefore, measuring the time interval the discriminator outputs 1 is a measure for the deposited charge. The time interval is called *Time over Threshold* (ToT) and its working principle is sketched in Figure 3.5a. ToT measurements in 25 ns bins are used by the ATLAS Pixel Detector.

The term test injection is also readable in Figure 3.4. It allows to inject a test charge into the front-end via a capacitor. As the capacitance of it is known, the amount of charge can be adjusted by applying a certain voltage to the capacitor. The test injection circuit

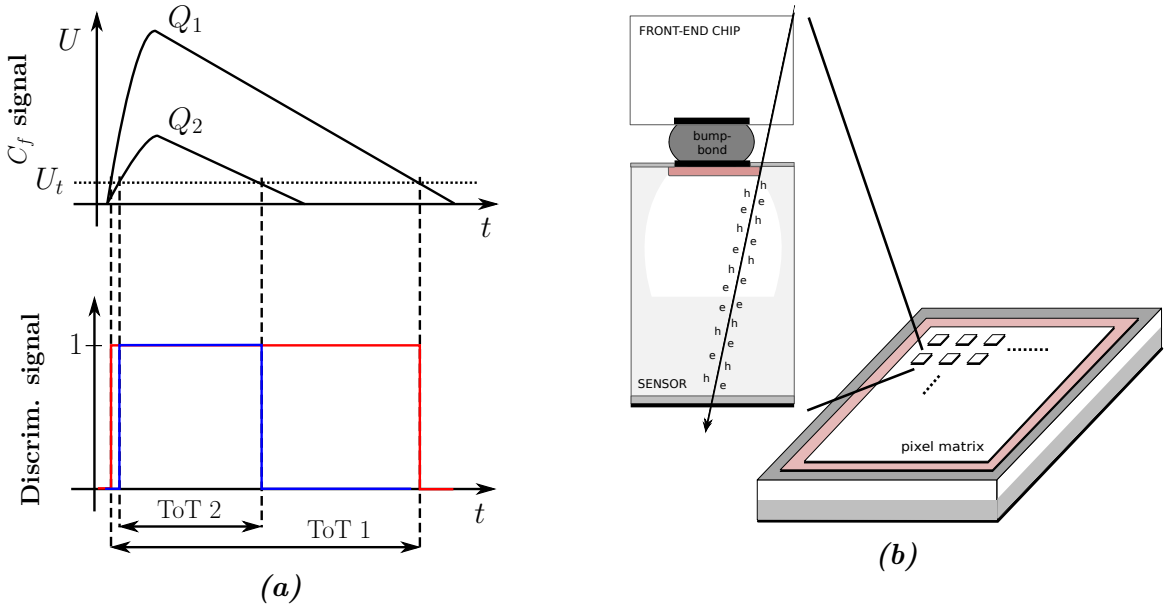

Figure 3.5.: (a) Signal after two particles traversing the detector depositing the charges Q_1 und Q_2, where $Q_2 < Q_1$ after the filter (top, labelled by C_f signal) and at the discriminator output (bottom). The discriminator threshold is denoted by U_t. The ToT is related to the amount of charge deposited. (b) A hybrid Silicon pixel detector with sensor, bump-bond and front-end chip within a schematic setup of an example pixel detector.

is used to tune the front-end chip to a specific threshold, for example to 1000 electrons, by adjusting the discriminator threshold. For a front-end chip containing several pixels, a threshold baseline can often be set globally and a fine tune carried out per pixel. If the amplifier output voltage of a read-out channel is above threshold, one says that a *hit* occurred or that a pixel *fired*.

The front-end chip is connected to the sensor by bump-bonds. These are little solder-balls which are placed between front-end chip and sensor pixel. After heating, they melt and a connection between front-end chip input and sensor pixels is established, as shown in Figure 3.5b. Also visible in Figure 3.5b is a schematic setup of an example pixel detector.

The hit information of a front-end chip is usually transferred to off-detector read-out units for further processing.

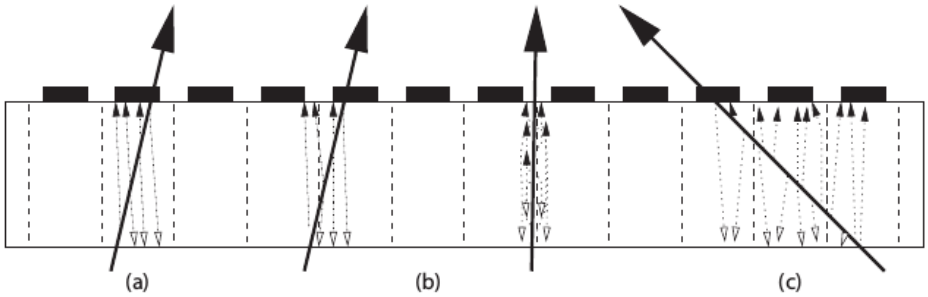

Figure 3.6.: (a) A single hit. (b) The particle traverses between two pixels and creates two hits. (c) Because of the angle of the particle through the sensor, several pixels show a hit (Copyright: [23]).

3.6. Characteristics of pixel detectors

Charge sharing

Since within the sensor of a pixel detector, two pixels are usually not separated by walls or similar, an incoming particle may cause multiple pixels to fire. This is called *charge sharing* and shown in Figure 3.6. The figure shows different situation in which charge sharing can occur, such as when tracks are bent. Charge sharing can alter the position resolution of a pixel detector.

If multiple hits are seen next to each other, this is called a *cluster*. Clusters can have different shapes and forms. The size of a cluster describes the number of pixels involved.

Charge collection distance

The *charge collection distance* (CCD) describes the average distance an electron and hole can travel, before being caught in traps. Traps are localised states in the band gap, which prevent electrons and holes from continuing to move. Traps have relaxation times. If being trapped for too long, an electron-hole pair will not contribute maximally to the signal or not at all. The CCD therefore is a measure for how much created charge will be part of the signal. It depends on the bias voltage, as the higher it is, the less the trapping probability. In formulas, the CCD of a sensor in an electric field of strength E can be calculated by using the mobility $\mu_h = \frac{v_h}{E}$ of holes and electrons $\mu_e = \frac{v_e}{E}$ and the life time τ_h of holes and electrons τ_e

$$\text{CCD} = v_e\tau_e + v_h\tau_h = (\mu_e\tau_e + \mu_h\tau_h)E.$$

The life time here describes the average time it takes before a free electron or hole is trapped. One could now assume that the CCD can infinitely rise with increasing electric field. However, it cannot, since the velocity of the charge carriers inside a material is limited by the so-called saturation velocity.

Experimentally, the CCD of a sensor of depth d can be measured by

$$\mathrm{CCD} = d\frac{Q_{\mathrm{meas}}}{Q_{\mathrm{orig}}}.$$

Thereby, Q_{meas} is the measured charge and Q_{orig} is the charge originally created. The CCD can be determined, for example by depositing charge with a laser or radioactive source.

Leakage current

In a Silicon pixel detector, a constant current flow is observed, called *leakage current*. It is caused by different phenomena. One is that electron-hole pairs can form thermally in the depletion volume leading to a steady current flowing through the pixel sensor. The leakage current is proportional to the depleted volume of the sensor and increases with the applied voltage and with the temperature. It decreases with the band-gap.

Noise

Noise describes the statistical fluctuation of a signal. There are three main sources of noise in a typical pixel detector. One is *thermal noise*. It originates from the thermal (statistical) fluctuations of charge carriers. The power spectrum is independent of frequency and only depends on the temperature. A second main form of noise is called $\frac{1}{f}$*-noise* due to its frequency dependence on negative powers of f. $\frac{1}{f}$-noise occurs if a process depends on several sub-processes which each have different time constants. An example could be trapping of charges in traps of different depths, which will all have different release times. Finally, there is *shot noise*. Shot noise results from charge fluctuations when a boundary is crossed. In the presence of a current $I = \frac{eN}{\Delta t}$ (N is the number of charges and Δt the time interval in which they pass by), the shot noise is given by $\sigma^2_{I,\mathrm{shot}} = \frac{Ie}{\Delta t}$ [24]. Leakage current thus induces shot noise.

Radiation damages

Particles traversing a Silicon pixel detector do not only create electron-hole pairs in the sensor which induce a signal. They can for example also lead to permanent sensor lattice

damages or permanent oxide charges in *metal-oxide semiconductor field-effect transistors* (MOSFETs) which are often installed in the front-end chip. Radiation damage is quantified by two parameters, depending on the damage described. These are the *NIEL* (non-ionising energy loss) equivalence fluence and the *TID* (total ionising dose). The former is a measure for the non-ionising damage, the latter for the damage caused by ionisation. The TID is especially used in connection with oxide charge damages.

Lattice damages in the sensor introduces traps, leakage current sources and changes the doping concentration. The traps reduce the CCD and output signal. So, both traps and higher leakage current decrease the signal to noise ratio (SNR). Furthermore, an increased leakage current yields a higher power dissipation of the sensor. Subsequently the temperature rises, meaning more thermal electron-hole pairs, or, an increased leakage current. The system is in danger of a *thermal runaway*. To prevent this, many detectors are cooled. The change in doping concentration can result in n-doped Silicon undergoing *type-inversion*, i.e. turning into p-doped Silicon. It can lead to full depletion not being possible any more and efficiency being reduced.

When MOSFETs are irradiated, the oxide layers are ionised. Charges can be permanently trapped, causing a different long-term electronic behaviour of the transistors than before. For example the current consumption can increase.

By heating up sensors, damages can be partially cured or *annealed*. The annealing depends on the temperature and time a sensor is exposed to it. While electron traps and leakage current are typically reduced with temperature and exposure time, the number of hole traps increases. For the type-inversion, heating anneals the effect at first. If exposed to heat for too long time though, the type-inversion can get worse. For this reason, Silicon detectors are typically cooled, even when there is no radiation.

3.7. Diamond Pixel Detectors

According to convention, diamond is an insulator with a band-gap of 5.5 eV. It consists of Carbon in an sp^3-binding. Diamond has several different properties with respect to Silicon and is very suited for extreme radiation environments. Artificial, so-called *Chemical Vapour Deposition* (CVD) diamonds are used for pixel detector applications. CVD diamonds are grown on a Silicon, diamond or, as recently shown [25], on an Iridium substrate from a mixture of methane (CH_4), molecular Hydrogen (H_2) and other gases. The hydrogen is stripped from the methane and the remaining Carbon creates the diamond. A plasma created with microwaves is used to do so. CVD diamond is made in two forms: polycrystalline (pCVD) with grain boundaries and single-crystalline (scCVD) without. A

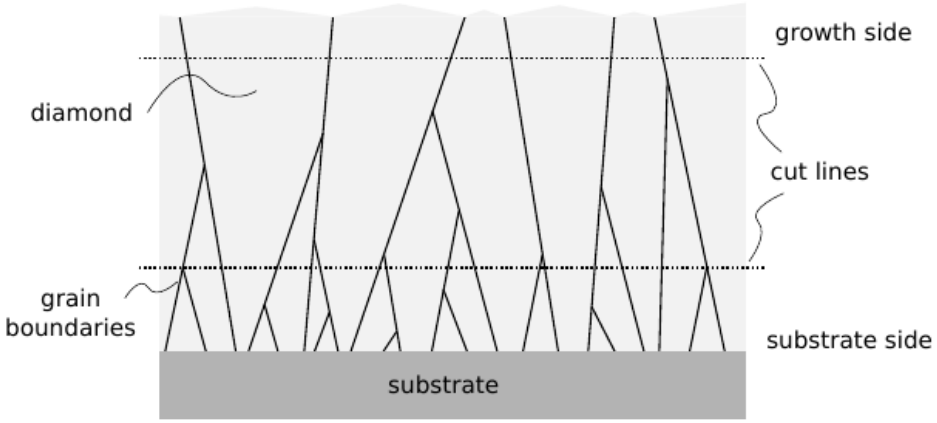

Figure 3.7.: pCVD diamond including its grain boundaries. The irregular shapes are a result of the growth process.

sketch of pCVD diamond can be found in Figure 3.7.

The properties of CVD diamond and Silicon are compared in Table 3.1. On average, the energy required to produce an *e-h-* (electron-hole) pair in diamond is nearly four times as large as for Silicon. At the same time, diamond has a higher mass density than Silicon, which according to Equation (3.1) means an average higher energy loss per penetration depth. Resulting, 36 e/h pairs are created on average per µm in diamond and 89 e/h pairs per µm in Silicon.

The charge transport in diamond offers higher mobility than in Silicon. As can be seen from the lifetime in Table 3.1, diamond has more traps than Silicon though, which makes the number of charges contributing to the signal smaller. A good figure of merit for diamond sensors is thus the CCD, combing mobility and trapping probability. Diamond does not need to be depleted, as the intrinsic charge carrier density is low. However, for charge collection and to increase the CCD, a voltage often higher than typical Silicon depletion voltages is applied across the sensor. Diamond detectors can be considered as parallel plate capacitors with a diamond dielectric.

Traps occur in pCVD in high number at grain boundaries, but are also spread throughout the rest of the crystal. The traps at the grain boundaries have long trapping times. In order to increase the CCD of a diamond sensor, *pumping* can be employed. This means irradiating the diamond sensor before usage. The irradiation produces charges, which neutralise some of the traps, increasing the CCD thereafter. UV light can be used to detrap the charges again. For this reason the signal efficiency $\eta = \frac{Q_{\text{coll}}}{Q_{\text{tot}}}$ increases in pCVD diamond after some (small) amount of irradiation.

The effect of irradiation on diamond is mostly the increased number of traps and con-

Property	Silicon	Diamond
atomic number	14	6
mass density [g/cm^3]	2.328	3.51
band-gap [eV]	1.12	5.5
intrinsic charge carrier density [cm^{-3}]	1.01×10^{10}	$\simeq 0$
resistance [Ω cm]	2.3×10^5	$\simeq 10^{16}$
permittivity $\epsilon = \epsilon_r \epsilon_0$	11.9	5.7
radiation length X_0 [cm]	9.36	12.15
av. energy to produce an e-h pair [eV]	3.65	13.1
mobility [cm^2 V^{-1} s^{-1}]		
of electrons	1450	$\simeq 1800$
of holes	500	$\simeq 2300$
av. life time before trapping		
of electrons	> 100 µs	$\simeq 100$ ns
of holes	> 100 µs	$\simeq 50$ ns
av. displacement energy [eV]	25	43
av. signal created per µm [e]	89	36

Table 3.1.: Properties of Silicon and CVD diamond compared [26–28].

sequently a reduction of the CCD. The mean free path λ of electrons and holes before being trapped as a function of the radiation fluence Φ for 25 MeV (very damaging) and 24 GeV (less damaging) protons for pCVD and scCVD diamond is shown in Figure 3.8. The two curves for pCVD and scCVD diamond have a similar shape, but are offset with respect to each other. Since they can be described by $\frac{1}{\lambda} = \frac{1}{\lambda_0} + k\Phi$ (λ_0 is the intrinsic free path and k the *damage constant*) [29], pCVD behaves like pre-damaged scCVD diamond. The dependence of λ on the proton energy is also visible in Figure 3.8. The strong lattice binding makes doping of diamond challenging. Therefore, diamond sensors are typically not doped and type inversion does not occur after irradiation. Diamonds large displacement energy in comparison to Silicon leads to a general large radiation hardness.

The wider band gap of diamond yields a lower amount of thermal noise. At the same time, a much smaller leakage current with respect to Silicon ($I_{\text{leak}} \sim T^2 e^{-\frac{E_g}{2kT}}$ with E_g the band gap energy) is observed. This still holds true after intense irradiation and reduces the shot noise and risk of thermal runaway in contrast to Silicon. Hence, diamond provides material for a low noise detector, which does not require cooling.

To compare the performance of Silicon and diamond after irradiation, it makes sense to compare the SNR of the two. It was computed in [30] and is shown in Figure 3.9. Evidently, diamond shows better performance for fluences above 10^{15} p/cm^2 for 25 MeV protons and above 7×10^{15} p/cm^2 for 24 GeV protons.

The grain structure of pCVD diamond can influence the position resolution of a diamond

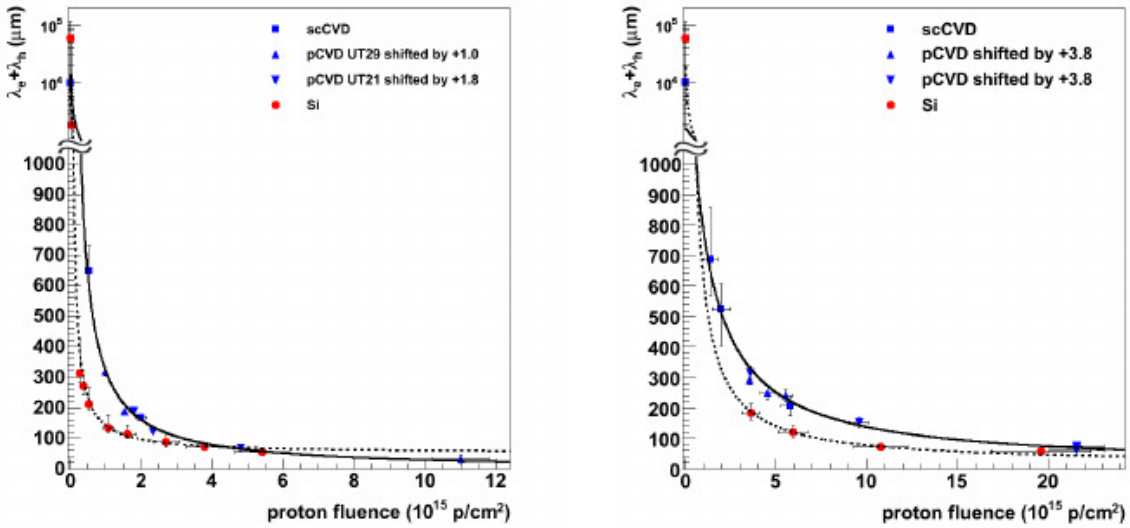

Figure 3.8.: The mean free path length of pCVD diamond, scCVD diamond and Silicon versus fluence for 25 MeV (very damaging, left) and 24 GeV protons (less damaging, right) [30].

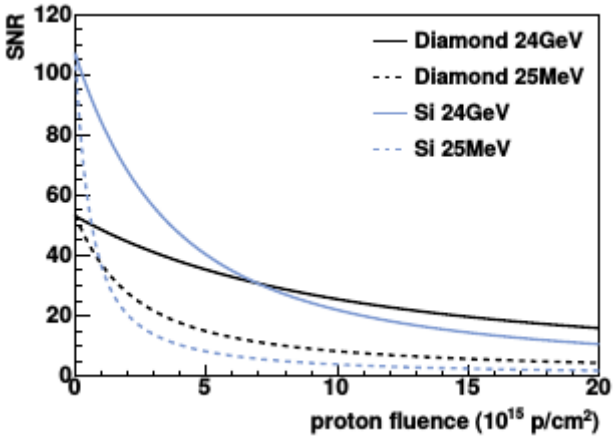

Figure 3.9.: The computed SNR for Silicon and diamond irradiated by protons of different energies. The sensors are both assumed to be 200 µm in thickness [30].

detector. Reasons are electrical polarisation of the grain boundaries resulting in deflections of the signal charges and irregular grain sizes combined with typically regular front-end chip connection structures.

4. The ATLAS Experiment

4.1. The Large Hadron Collider

The Large Hadron Collider (LHC) [31] is the largest particle physics accelerator in the world. It was designed for a maximum centre-of-mass energy of 14 TeV and a peak luminosity of $10^{34}\,\mathrm{cm}^{-2}\,\mathrm{s}^{-1}$. The LHC is installed inside the old LEP [32] tunnel about 100 m below ground and is constructed in a circle of 27 km circumference. It consists of two beam-pipes in which protons or heavy ions (for example Pb) are accelerated in opposite directions. The acceleration is achieved by superconducting radio frequency cavities. Using the Lorentz force, particles are kept on a circle by dipole magnets. The maximum centre-of-mass energy and circumference require magnetic fields with a field strength of up to 8.33 T. To achieve this, 1232 superconducting NbTi dipole magnets are used and cooled to below 2 K. Since same sign electrically charged particles are running along the two different beam-pipes, the magnetic field in the two has to point in opposite directions. Particles inside the LHC are separated into 2808 bunches of 24.95 ns spacing which can be located at 3564 positions. Each bunch contains up to 1.15×10^{11} protons which are compressed to a 4σ-bunch length of about 1.06 ns at 14 TeV.

To accelerate particles to the LHC energies, multiple pre-accelerators are used. These are the *LINAC2* (accelerates particles to 50 MeV), the *Proton Synchrotron Booster* (1.4 GeV), the *Proton Synchrotron* (PS, 25 GeV), the *Super Proton Synchrotron* (SPS, 450 GeV). The SPS then injects the particles into the LHC. The complete filling chain of the LHC takes at least 16 min and this process is called a *fill*. The energy transition from 450 GeV to 7 TeV per beam takes about 20 min. Bunches of 7 TeV protons then collide at a centre-of-mass energy of 14 TeV. The lifetime of a fill is about 15 h. It is defined as the time after which the luminosity has been decreased to $\frac{1}{e}$ of the original one. The main effects on the reduction of the luminosity are the collisions of particles, multiple coulomb scattering of the protons or Lead ions in a bunch and interactions of bunch particles with rest-gas particles of the vacuum inside of the beampipe.

The accelerated beams are collided in four interaction points (IPs). The interaction points are surrounded by detectors, to register all particles created in a collision. These

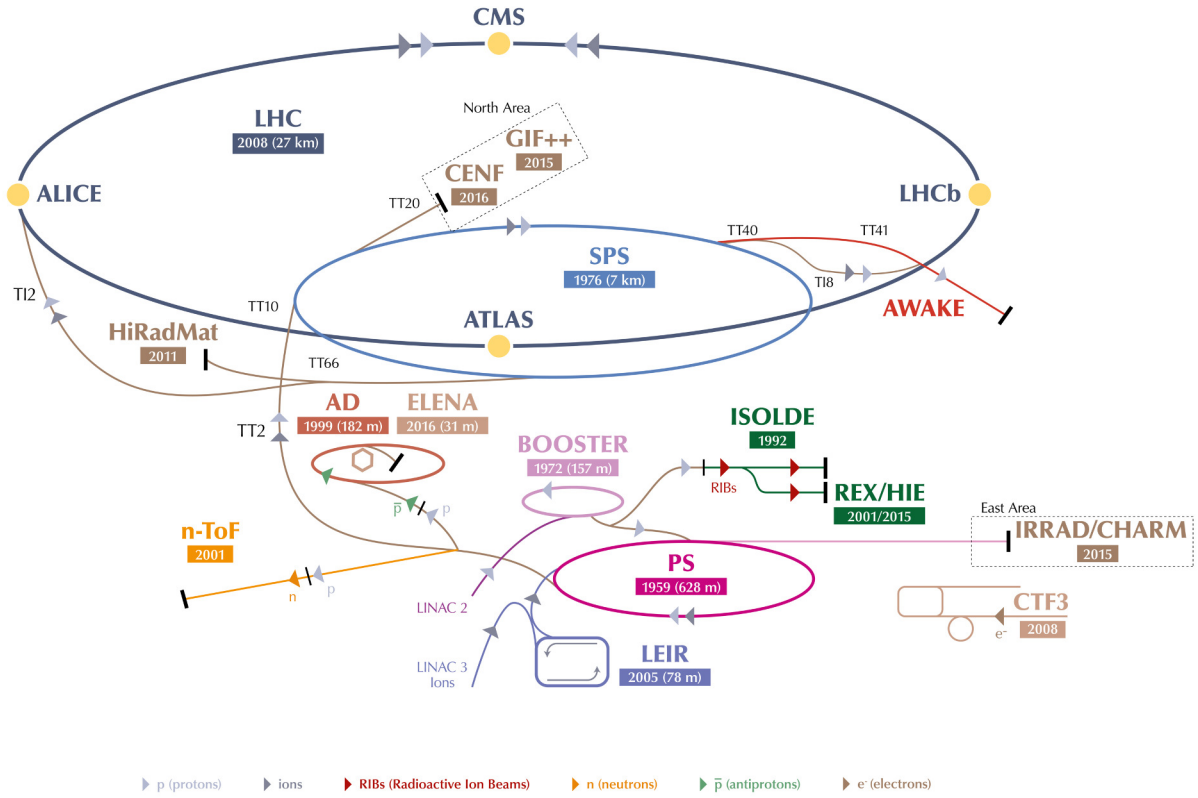

Figure 4.1.: Overview of the LHC injection accelerators and the LHC experiment positions (Copyright: CERN).

are the *A*TLAS [33], *C*MS [34], *A*LICE [35] and *LHCb* [36] experiments, which are located each at one of the IPs. ATLAS and CMS are general purpose detectors and searching mainly for the Higgs boson, Supersymmetry and other physics beyond the SM. ALICE concentrates on QCD and quark-gluon plasma studies. LHCb's focus is on CP-violation and the rare decays of B-hadrons.

An overview of the LHC injection and experiment positions can be found in Figure 4.1.

After some initial commissioning problems in 2008, the LHC re-started commissioning at the end of 2009. It was operating at a centre-of-mass energy of 7 TeV from 2010–2011 and of 8 TeV in 2012. The peak luminosity was $7.7 \times 10^{33}\,\mathrm{cm}^{-2}\,\mathrm{s}^{-1}$ [37]. After the *long shutdown 1* (LS1) from 2013–2015, the LHC went on operating at 13 TeV centre-of-mass energy and a peak luminosity of more than $10^{34}\,\mathrm{cm}^{-2}\,\mathrm{s}^{-1}$ was reached in 2016.

4.2. The ATLAS Experiment

The ATLAS experiment is one of the four LHC experiments and located at IP1 of the LHC about 100 m below the ground. It is a multi-purpose particle detector, which is 25 m in

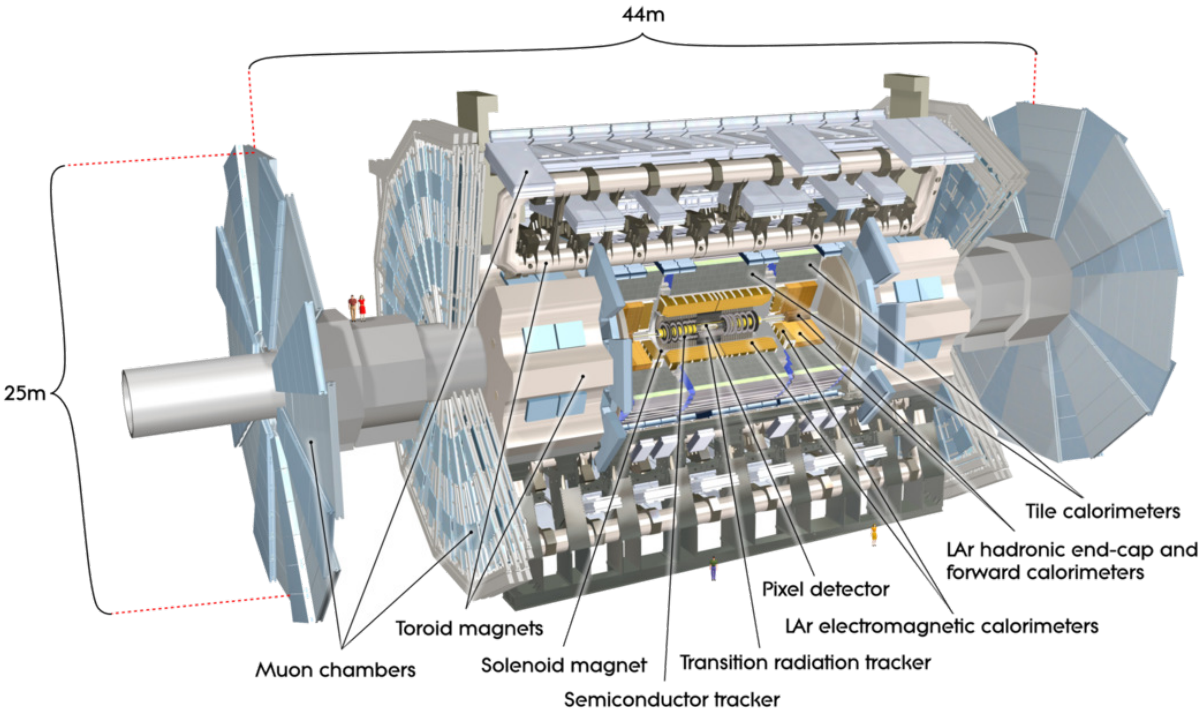

Figure 4.2.: A sketch of the ATLAS detector (Copyright: CERN).

height and 44 m in length. The detector is sketched in Figure 4.2. The main aims of the ATLAS experiment are to find and study the Higgs boson and to search for physics beyond the SM, such as SUSY or Dark Matter. Therefore, the ATLAS experiment wants to test the SM extensively. A particle suited to be the Higgs boson was discovered in 2012 by the ATLAS and the CMS experiment with a mass of about 125 GeV [9, 10]. Further study of the Higgs boson candidate is on-going. The ATLAS detector is a combination of multiple subdetectors which are described in detail in the following.

4.2.1. Coordinate system

The coordinate system of the ATLAS detector is the following: the origin is at the centre of the detector. The x-axis is defined as pointing from the origin to the centre of the LHC. The y-axis points upwards and the z-axis along the beam axis. As usual, spherical coordinates r, ϕ and θ are defined as well as the pseudo-rapidity $\eta = -\ln\left(\tan\left(\frac{\theta}{2}\right)\right)$. An η of $\pm\infty$ corresponds to the beam axis and an η of zero to the y-axis. The ATLAS detector can detect particles in a range of $0 \leq |\eta| < 4.9$ and $0 \leq \phi \leq 2\pi$.

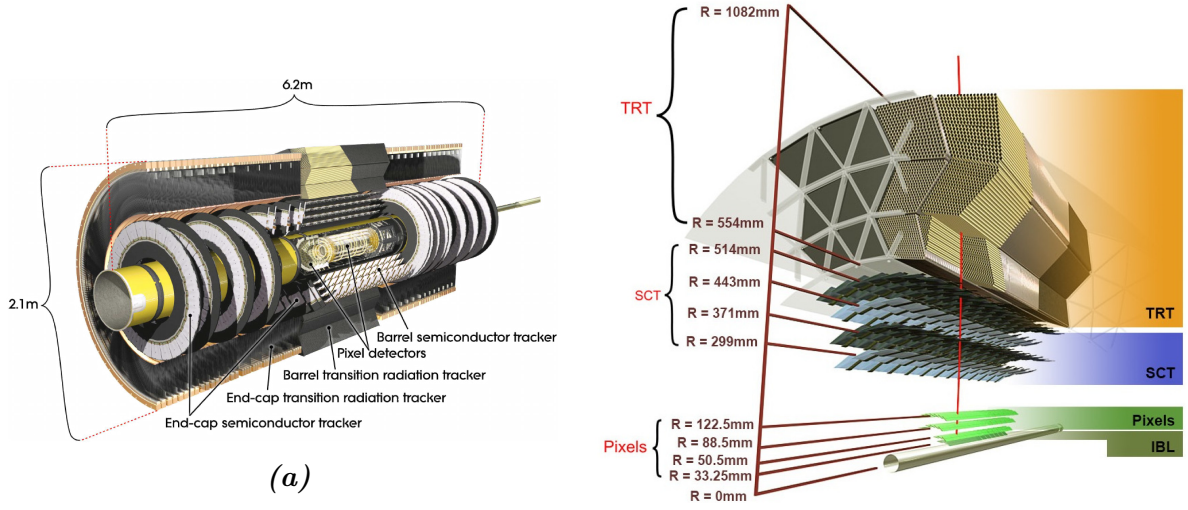

Figure 4.3.: (a) A sketch of the ATLAS ID. (b) This graphic shows the layer division of the ATLAS ID barrel (Copyright: CERN).

4.2.2. The Inner Detector

The main purpose of the Inner Detector (ID) is to measure tracks of charged particles. It incorporates the Pixel Detector, the Semiconductor Tracker (SCT), the Transition Radiation Tracker (TRT), the Beam Conditions Monitor (BCM) [38] and the Diamond Beam Monitor (DBM) [39]. Two drawings of the ID not showing the BCM and the DBM can be found in Figure 4.3a and Figure 4.3b. The DBM will be described in detail in Chapter 5.

Surrounding the ID is the ATLAS solenoid magnet, which produces a homogeneous magnetic field of 2 T strength inside of the ID in z-direction. By bending the trajectory of a charged particle within the magnetic field, its transverse momentum $\vec{p}_T$ can be reconstructed. The total momentum is then given by $|\vec{p}| = \frac{|\vec{p}_T|}{\sin(\theta)}$, with θ the angle of a track with respect to the z-axis.

The Pixel Detector

The Pixel Detector is composed of a barrel part and a disc part and sketched in Figure 4.4.

The Pixel Detector barrel consists of concentrically aligned cylindrical layers. From inner to outer these are the *Insertable B-Layer* (IBL) [40], the *B-Layer*, *Layer 1* and *Layer 2*. Their radii can be found in Figure 4.3b. The IBL covers a pseudo-rapidity of $\eta \leq |3|$ and the remaining Pixel Detector components combined of $\eta \leq |2.5|$.

The three Pixel Detector discs are installed around the beam-pipe on each side of the

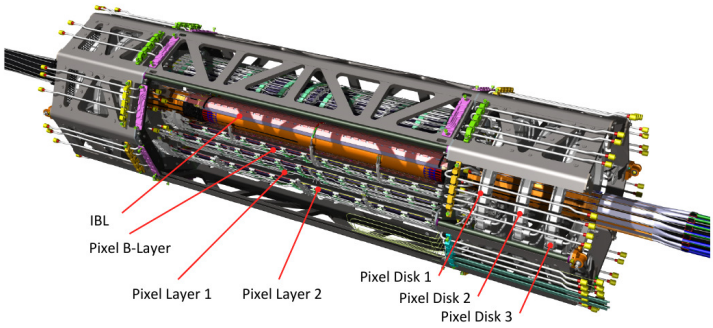

Figure 4.4.: Schematic drawing of the ATLAS Pixel Detector.

interaction point, each covering 88.8 mm $< r <$ 149.6 mm.

All components of the Pixel Detector are hybrid Silicon type. The pixels of the IBL, B-Layer, Layer 1 and Layer 2 are granular in $\phi \times z$, the pixels of the discs in $r \times \phi$. In all components but the IBL, planar Silicon hybrid pixel detectors are used with a minimum pixel pitch of 50 µm × 400 µm. The IBL uses planar and 3D hybrid pixel detectors of 50 µm × 250 µm pitch, which are aligned with the long edge in z-direction. Planar sensors have flat, pixel like charge collection electrodes at the top of the sensor, while 3D sensors have pillar like charge collection electrodes permeating the entire sensor thickness.

The Pixel Detector was designed to offer precise tracking. This requires optimising several parameters, such as the material budget to reduce deflection of particles by multiple scattering or the increase of granularity towards lower r to allow for high track densities.

The SCT and the TRT

The SCT and the TRT consist of barrel layers installed in concentric cylinders around the beam-pipe and of discs, called *end-caps* installed around the beam-pipe beyond the scope of the barrel.

The SCT is a Silicon strip detector. It has a set of stereo strips in each layer, which means that two strips are installed at an angle, the *stereo angle*, with respect to each other. This leads to two dimensional track points in each layer. In the SCT, the stereo angle is 40 mrad. The strips have a pitch of about 80 µm and are directed in z-direction in the barrel and in r-direction in the end-caps.

The TRT is a straw tube detector made of 4 mm diameter straw tubes. In the barrel region, straw tubes run in parallel to the beam axis and are split into two at about $\eta = 0$. In the end-caps, the straw tubes are aligned in r-direction. The TRT only provides an $(r \times \phi)$-coordinate.

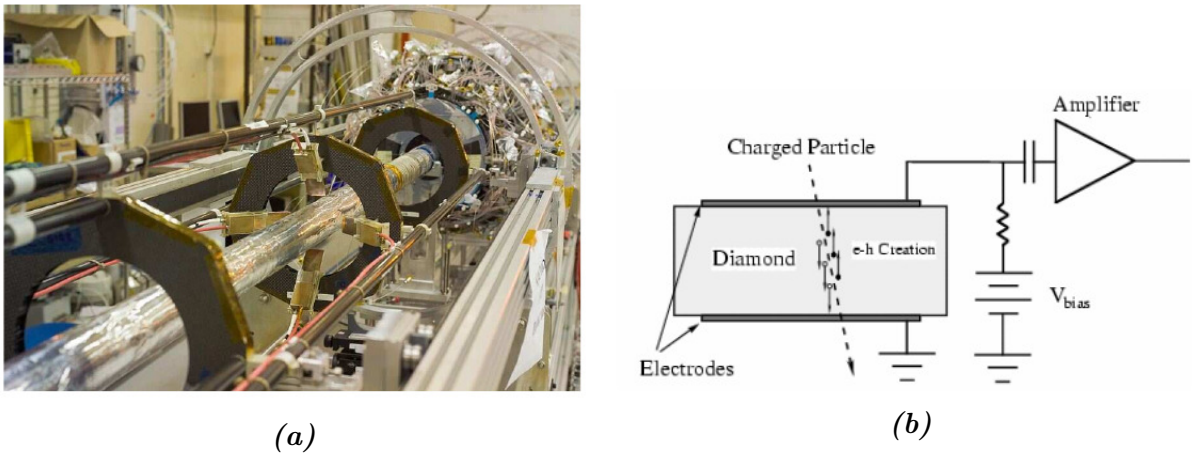

Figure 4.5.: (a) The position of the BCM behind the Pixel Detector before installation in Atlas. (b) The general setup of the diamond sensors and read-out.

The BCM

In case of multiple proton bunches hitting the Atlas collimators, a large flux of particles could traverse Atlas, leading to high instantaneous doses. In the worst case, this could damage detector components. The idea of the BCM is to identify such dangerous events and to prevent potential damages. Besides, the BCM measures the beam halo (particles that are produced close to the beam-pipe and form a "halo" of particles around the beam in the beam-pipe) and the instantaneous luminosity. The BCM is constructed of four single pad diamond sensors installed around the beam pipe on either side of the interaction point, as shown in Figure 4.5a. One pad is one read-out channel and has a sensitive area of 8 mm × 8 mm. The general setup of a sensor and read-out are shown in Figure 4.5b. The BCM electronics are radiation hard and have a signal rise time of 1 ns [41].

The distance between the two BCM stations is chosen such that the travel time from one station to the other (at the speed of light) is 12.5 ns. Together with the fast timing, beam background and particles from a collision can be distinguished. The idea is that if a collision takes place, particles will be found in both BCM stations with a timing difference of 0 s. Particles that do not emerge from a collision and traverse the two BCM stations will not produce a coincidence, but have a timing difference of at least 12.5 ns. This allows the beam background to be estimated.

The luminosity is measured with the BCM by counting the hits on either side of the BCM which arrive between $t-6.25$ ns and $t+6.25$ ns, where t is the time at which particles emerging from a collision are expected to arrive at the BCM. The principle of luminosity measurements is described in Section 4.2.6.

4.2.3. Calorimeters

To get the full 4-momentum information of a particle, momentum and energy have to be measured. Momentum is measured by the ID for all charged particles and more precisely for muons by the muon system. *Calorimeters* measure the energy of all particles, but muons and neutrinos. They use very dense material to slow particles down and in the best case stop them, depositing all of their energy. The deposited energy is then measured. ATLAS uses so-called sampling calorimeters. These have one layer of high density passive material to slow particles down and one layer of active material to carry out the energy measurement. The main calorimeters of ATLAS are shown in Figure 4.6a. Because the calorimeters stop particles to measure their entire energy, particles other than muons are prevented from arriving at the muon chambers.

The *Electromagnetic Calorimeter* (ECal) of ATLAS consists of a barrel and two end-caps. It uses Lead as passive and liquid Argon as active material. In the ECal, electrons and photons trigger electromagnetic showers. By measuring the deposited charge of the shower particles, the energy of the original particle is obtained.

The Hadronic Calorimeter (HCal) in ATLAS is built around the ECal. As hadrons interact differently with matter (also via the strong force), other absorption materials are needed. Hadrons create hadronic and electromagnetic showers, whose energy is measured. The hadronic showers mainly consist of pions. The HCal comprises the *Tile Calorimeter*, the *Tile Extended Barrel*, the *Liquid Argon (LAr) Hadronic End-Cap* (HEC) and the *LAr Forward Calorimeter* (FCal). The Tile Calorimeter is situated in the barrel, the others are built into the end-caps. The Tile Calorimeter and Tile Extended Barrel use Steel as passive and scintillating tiles as active material. The HEC uses Copper as passive and LAr as active material. It overlaps with the FCal in certain parts.

The FCal is specially designed to minimise the number of neutron back-splashes from the calorimeters into the ID. It consists of three layers, one using Copper as passive material, two using Tungsten. The active material of all three layers is LAr. The first layer is specified for electromagnetic, the other two for hadronic measurements.

4.2.4. The muon system

The ATLAS muon system is shown in Figure 4.6b. The aim of the muon system is to measure the muon momentum. To do so, the muon trajectories are bent by large air-toroidal magnets, reducing the amount of multiple-scattering, while providing sufficient magnetic fields. Different gas detectors, the *Monitored Drift Tubes* (MDTs) and the *Cathode Strip Chambers* (CSCs) are used for precision track measurements. *Resistive*

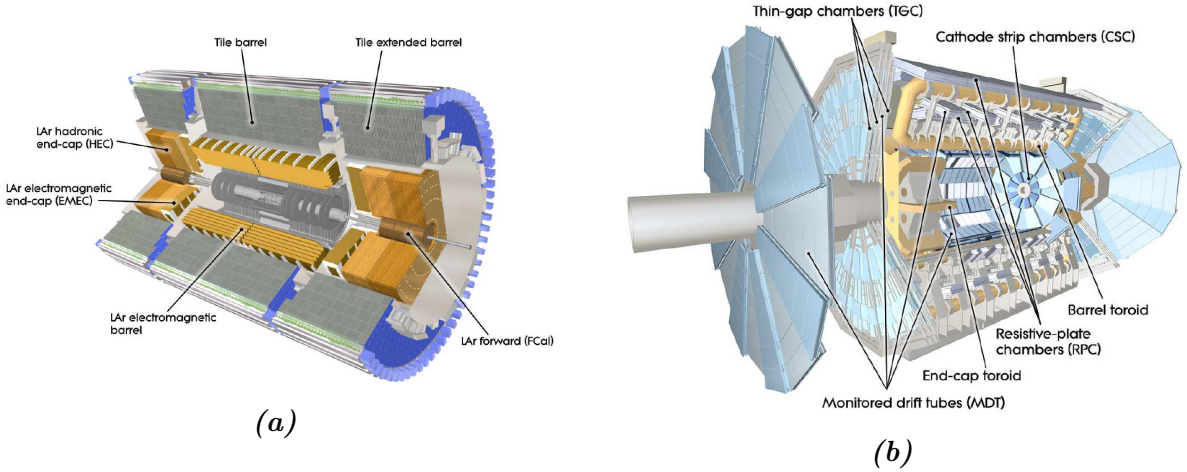

Figure 4.6.: (a) The main calorimeters of ATLAS. (b) The ATLAS muon system (Copyright: CERN).

Plate Chambers (RPCs) and *Thin Gap Chambers* (TGCs), both being gas detectors, are used for the trigger system and for complementary muon position information with respect to the other muon detectors. Within the trigger system their purpose is to deliver bunch crossing identification and p_T thresholds.

4.2.5. The trigger system

Collisions in the ATLAS detector take place (at most) every 25 ns or at a (maximum) frequency of 40 MHz. However, the ATLAS computing systems can only store data at about 3 GB/s, which corresponds to a detector read-out rate of ∼1 kHz. The ATLAS trigger system selects which events to write to disc. It consists of the *Level-1 Trigger* (L1) and the *High Level Trigger* (HLT). The L1 is a hardware trigger and uses information from the muon system and certain (largely segmented) parts of the calorimeters. It defines the *Regions-of-Interest* (RoIs), which appear to contain valuable information. The readout rate is reduced to about 100 kHz by the L1. The RoIs are passed on to the software HLT, which considers the full detector granularity in the RoIs and decides whether all available detector information shall be stored for an event [42]. This information is then available for physics analyses, for example.

4.2.6. Luminosity measurements

The instantaneous luminosity of a collider can be described by

$$\mathcal{L} = \frac{\mu n_b f_r}{\sigma_{\text{inel}}} = \frac{n_b f_r n_1 n_2}{2\pi \Sigma_x \Sigma_y} \tag{4.1}$$

with μ the average number of inelastic interactions per bunch crossing (pile-up), n_b the number of bunches, f_r the revolution frequency, σ_{inel} the inelastic scattering cross-section, n_1 and n_2 the number of particles in the two colliding bunches, respectively, and Σ_x and Σ_y the beam-width in x- and in y-direction.

When using a detector, one has a certain efficiency ϵ and measures $\mu_{\text{vis}} = \epsilon\mu$ and $\sigma_{\text{vis}} = \epsilon\sigma_{\text{inel}}$, the visible average number of inelastic interactions per bunch crossing and visible total cross-section. Thus,

$$\mathcal{L} = \frac{\mu_{\text{vis}} n_b f_r}{\sigma_{\text{vis}}}.$$

A detector can measure μ_{vis}, by counting events (see below). n_b and f_r are known. To calculate σ_{vis}, a so-called *van der Meer* scan is performed. The beam is thereby shifted first in x- and then in y-direction. Plotting the beam position in x and y against the number of hits yields bell-curves, from which the beam widths Σ_x and Σ_y can be calculated. Formula (4.1) then allows to calculate the luminosity. By taking the measured value of μ_{vis}, the visible cross-section σ_{vis} can be computed and the detector is calibrated to measure luminosity.

A detector dedicated to luminosity measurements is the ATLAS *LUminosity measurement using Cerenkov Integrating Detector* (LUCID) [43]. It is made of two stations positioned in the forward region of the ATLAS detector at $\pm 17\,\text{m}$ from the interaction point. The LUCID has 20 measurement units per side detecting penetrating particles. It uses different approaches to measure μ_{vis} and thus the luminosity. One is by counting the number of events that occurred with at least one hit in one of the measurement units on either side of the LUCID. This algorithm is called the `EVENT_OR`. The number of `EVENT_OR`-events N_{or} is related to μ_{vis} by

$$\mu_{\text{vis}} = -\ln\left(1 - \frac{N_{\text{or}}}{N_{\text{BC}}}\right)$$

with N_{BC} the number of bunch crossings which happened in the time that N_{or} was counted. Using upper procedure, the luminosity can then be calculated.

`EVENT_AND` describes a different luminosity measurement procedure. One counts the

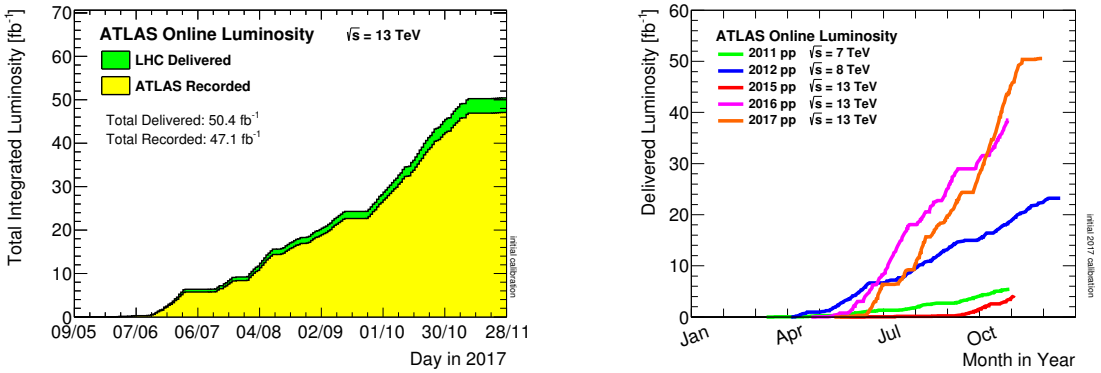

(a) *(b)*

Figure 4.7.: (a) The integrated luminosity in 2017. (b) The integrated luminosity for different years since 2011. There is no 2013 and 2014 data due to LS1 [45].

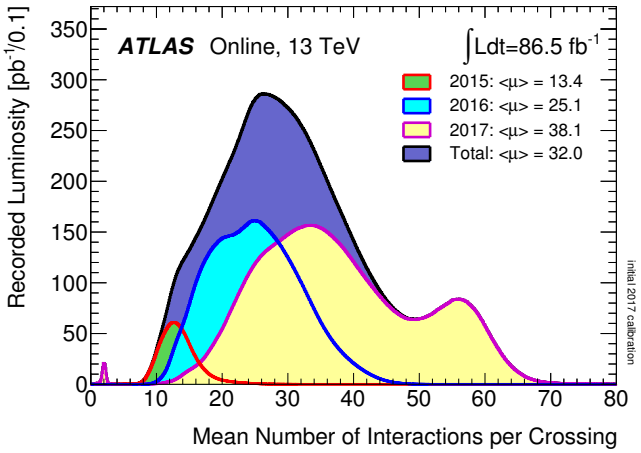

Figure 4.8.: The pile-up distribution μ measured in different years [45].

number of events, N_{and}, where at least one hit was observed in both sides of the LUCID. Calculating μ_{vis} is more complicated then and it is referred to [44] for more details. The `EVENT_OR` and `EVENT_AND` luminosity algorithms are also used by the BCM to determine the instantaneous luminosity.

During Run I, the *Minimum Bias Trigger Scintillators* (MBTS) were used for luminosity measurements as well. The scintillators are installed on the inward facing plates of the ECal end-cap and the purpose of the MBTS is to provide a trigger for low luminosity runs.

The integrated luminosity measured at ATLAS in 2017 and since 2011 are shown in Figure 4.7. Figure 4.8 shows the pile-up distribution measured with ATLAS for different years. In 2017, the average pileup was $\langle\mu\rangle = 38.1$ [45].

5. The ATLAS Diamond Beam Monitor (DBM)

The Atlas Diamond Beam Monitor (DBM) was designed to perform bunch-by-bunch luminosity, beam background and beam spot measurements. It consists of 18 pCVD diamond and 6 Silicon sensors, bump bonded to FE-I4B front-end chips. The FE-I4 is the front-end chip built for the Atlas IBL [40], which allows the DBM to use the same powering and read-out infrastructure the IBL uses. The DBM was installed during LS1 and was ready for operation in 2015 [46–48]. An image of the DBM installed around the beampipe can be seen in Figure 5.1.

5.1. Motivation

With increasing average number of collisions per bunch crossing μ, some luminosity algorithms (cf. Section 4.2.6) of the luminosity detectors LUCID and MBTS were approaching saturation in 2011 [44]. In principle, this was due to too little detector segmentation. As soon as the number of particles is high enough that these detectors show a hit in every bunch crossing, they become ineffective for measuring the luminosity.

Luminosity measurements are important for the determination of cross-sections of elementary particle reactions. Cross-sections in turn, give an important handle to test, for example the Standard Model and to look for physics beyond it. Their measurement is the ultimate goal of many particle physics experiments. Knowledge of the top-pair cross-section can allow measurement of the top mass for example. Further, accurate $W^{\pm}$ and Z^0 cross-sections can give more precise PDFs [49]. Consider some event $X \to Y$, then a particle detector usually counts the number of events N, rather than measuring its cross-section σ directly. However, with $\mathcal{L}$ the instantaneous and L the integrated luminosity, it holds

$$N = \sigma L = \sigma \int \mathcal{L}(t) \mathrm{d}t.$$

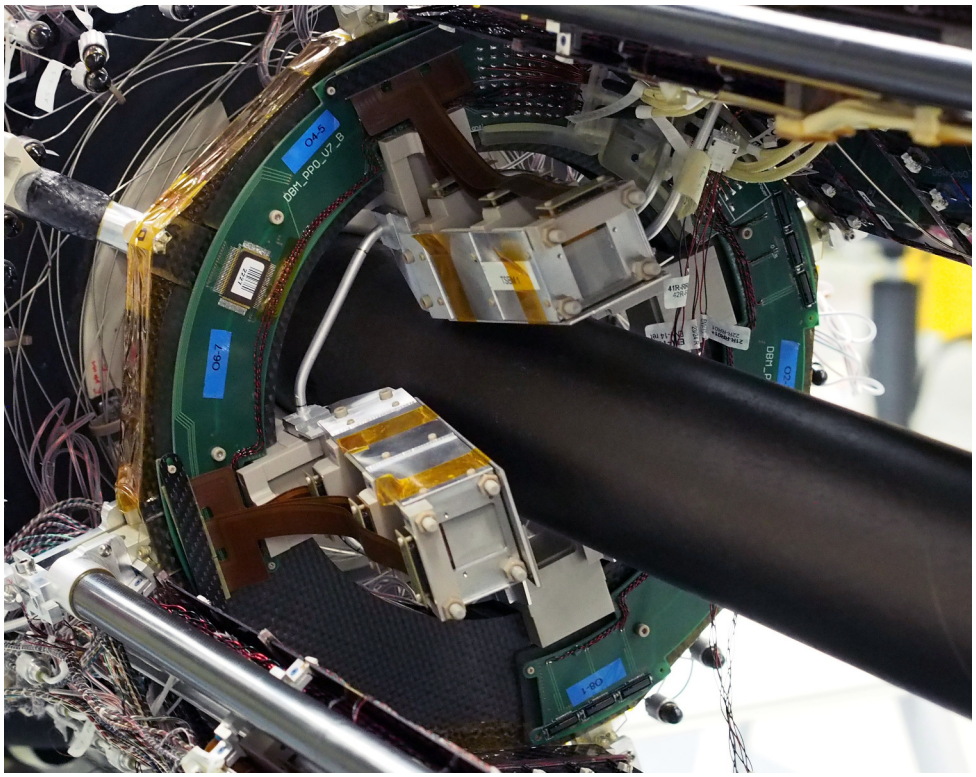

Figure 5.1.: The DBM installed around the beampipe.

Thus, accurate luminosity information is required for precise determination of the cross-section. ATLAS achieved a luminosity accuracy of 2 % in 2011, by combining results of several detectors using previously described luminosity determination techniques. In regard of upper saturation effects, this in turn meant that to maintain the luminosity accuracy, alternative luminosity measurements were needed. This was one reason to propose a new sub-detector for the ATLAS detector, the DBM. The second reason was to complement the Beam Conditions Monitor (BCM) [38] in its beam background determination [39]. Furthermore, the DBM was proposed to determine the beam spot, i.e. the position of the luminous region.

5.2. Setup and Design

The DBM consists of eight so-called telescopes, four on either side of the Pixel Detector, as sketched in Figure 5.2. The telescopes are distributed evenly around the beampipe. Each telescope is made of three pixelated sensors bump-bonded to FE-I4 front-end chips. Sensors and front-end chip will be further discussed below. The combination of sensor and front-end chip is called a *module*. Having three modules in a telescope allows track reconstruction of particles traversing the telescope to be carried out. This can be used

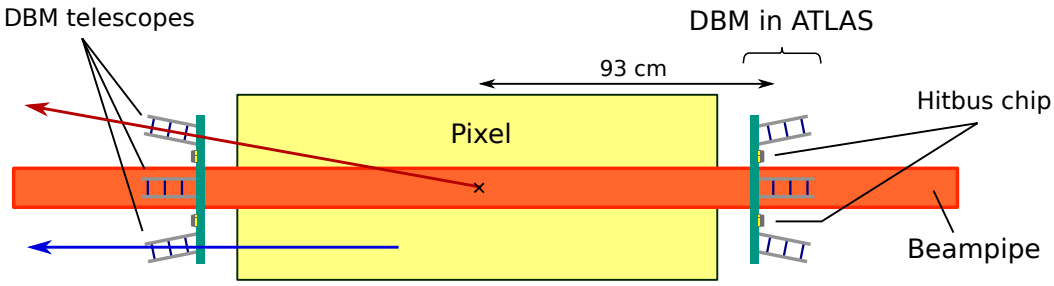

Figure 5.2.: Position of the DBM within ATLAS on the left and on the right of the Pixel Detector. The cross symbolises the interaction point.

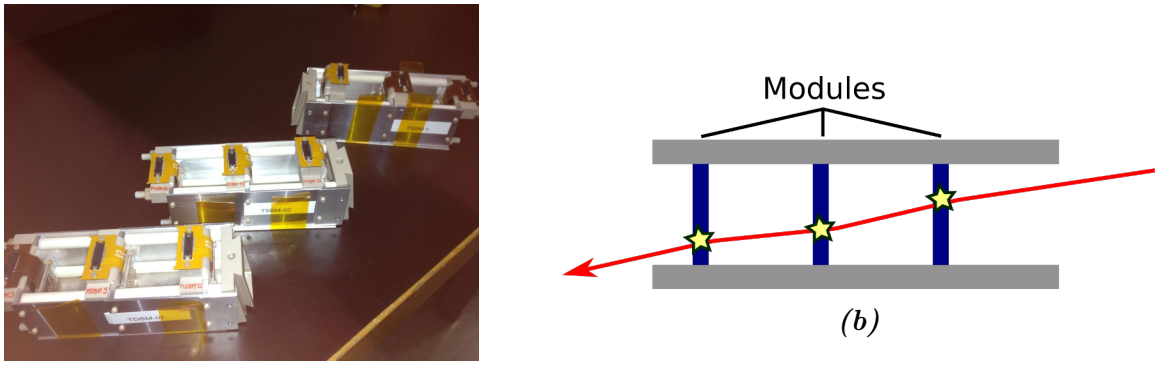

Figure 5.3.: (a) A photograph of some DBM telescopes and (b) a sketch of a DBM telescope with particle track.

for luminosity measurements, beam background studies and beam spot determination. Some DBM telescopes are shown in Figure 5.3a and a telescope and a particle track are sketched in Figure 5.3b.

The telescopes are installed at an angle of 10° with respect to the beampipe in ATLAS, as illustrated in Figure 5.2. This rather small angle was chosen in order to suppress so-called *erratic dark currents*, which can form in diamond sensors [50]. These can be damped by installing a magnetic field in parallel to the direction of the electric field applied to the diamond sensor. Since the magnetic field in ATLAS is directed along the beampipe, the sensors would most ideally be installed perpendicular to the direction of the beampipe. Yet, particle reconstruction from the vertex and hence all kind of measurements would be more difficult in this case. Therefore, an inclination of 10° was chosen to compromise the two requirements.

The η region covered by the DBM is $3.2 < |\eta| < 3.5$ and a module's active area is $20.0\,\text{mm} \times 16.8\,\text{mm}$ in size.

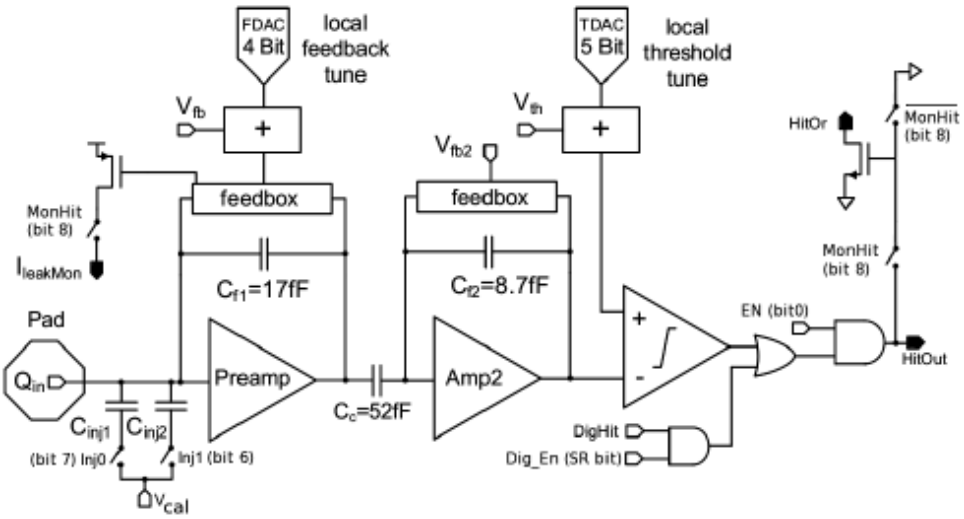

Figure 5.4.: The circuit diagram of an FE-I4 pixel.

5.2.1. Sensor and front-end chip

As previously stated, 18 sensors are pCVD diamond, while the remaining ones are planar Silicon sensors. The thickness of the diamond sensors is 500 µm and the charge collection distance is around 200 µm.

The front-end chip of the DBM is called the FE-I4B [51], which is also used by the IBL. It consists of a total of 26 880 pixels, divided into 336 rows of 50 µm and 80 columns of 250 µm pitch. The modules are installed in ATLAS, such that the finer segmentation is along η and the more coarse one along ϕ. The FE-I4 chip allows ToT measurements, giving the amount of deposited charge. The circuit diagram of an FE-I4 pixel can be found in Figure 5.4. The FE-I4 is a programmable chip in the sense that it contains registers which can be altered. For example the discriminator threshold can be adjusted globally by a register called *GDAC* and per pixel by a register called *TDAC*. Pixels can be enabled and disabled by registers. Data sent by the FE-I4 chip is 8b/10b encoded for engineering purposes[1].

5.2.2. PP0 and the hitbus chip

A picture of a DBM module can be found in Figure 5.5a. Visible in this picture is also the module flex, which is glued on top of a module. The module flex is a flexible *printed circuit board* (PCB) and connected to the FE-I4 via wirebonds. The wirebonds are thin Aluminium wires with a thickness of 25 µm. Figure 5.5b sketches the connection of sensor,

[1] In 8b/10b encoding the information of 8 bits is saved into 10 bits in a certain way.

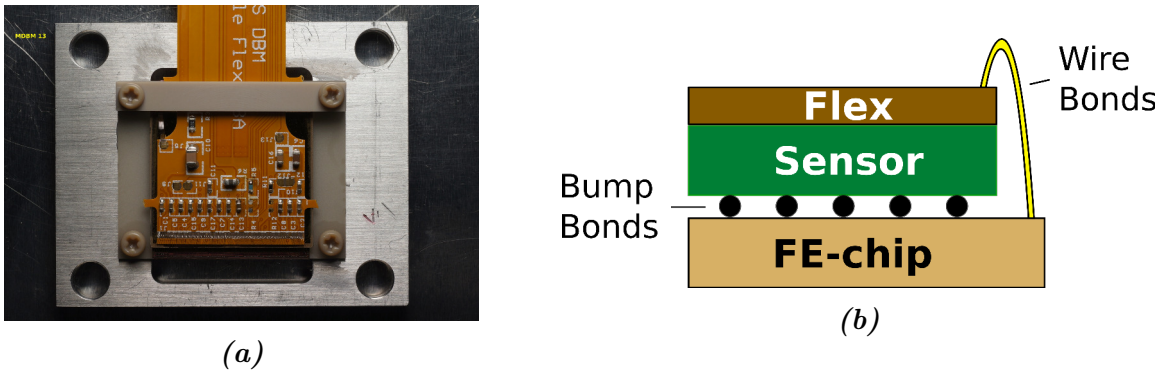

(a) *(b)*

Figure 5.5.: (a) A picture of a DBM module with module flex. (b) A sketch of the sensor, front-end and module flex.

front-end and module flex. Clock-, command-, (return) data- and power-supply lines of a module are connected via the module flex and an attached flex cable with *Patch Panel Zero* (PP0), which is a PCB. Two telescopes are mounted on PP0 and two different forms of it exist for the DBM in ATLAS to distribute the telescopes around the beampipe, while saving as many cables as possible. PP0 is connected to power supplies and further read-out devices.

On PP0, two telescopes are connected to the *hitbus chip*. The hitbus chip takes the *HitOr*-output of an FE-I4, which is the OR of a hit in any enabled pixel, and evaluates a programmable coincidence with the output of the other modules of one telescope [52]. The output of this logic is then used to trigger the three modules of the telescope. The logic carried out by the hitbus chip could have also been provided by a software off detector. However, the number of signals that would have had to be sent off and on detector made this infeasible. Therefore, the hitbus chip was developed.

5.2.3. Transport and handling of signals

Data coming from PP0, and clock and commands to it, go via electrical cables to the *opto-board*. The opto-board converts the electrical signals to optical signals and vice versa. About 80 m long optical fibres transport the optical signals to or from the *Back of Crate card* (BOC). The fibres to the opto-board are called *transmission-lines* (Tx-lines), the ones to the BOC *receiving-lines* (Rx-lines). A Tx-line is shared by 2 or 4 modules and there is one Rx-line per module. The BOC is situated in a VME crate and all connections to the modules pass through it, as well as all connections to further *Read-Out Subsystem PCs* (ROSes), which go via optical fibres, called *S-Links* [53]. The BOC decodes the 8b/10b signal coming from the FE-I4s and passes the data on via the VME back plane to the *Read out Driver* (ROD). The ROD further processes the data from the front-end

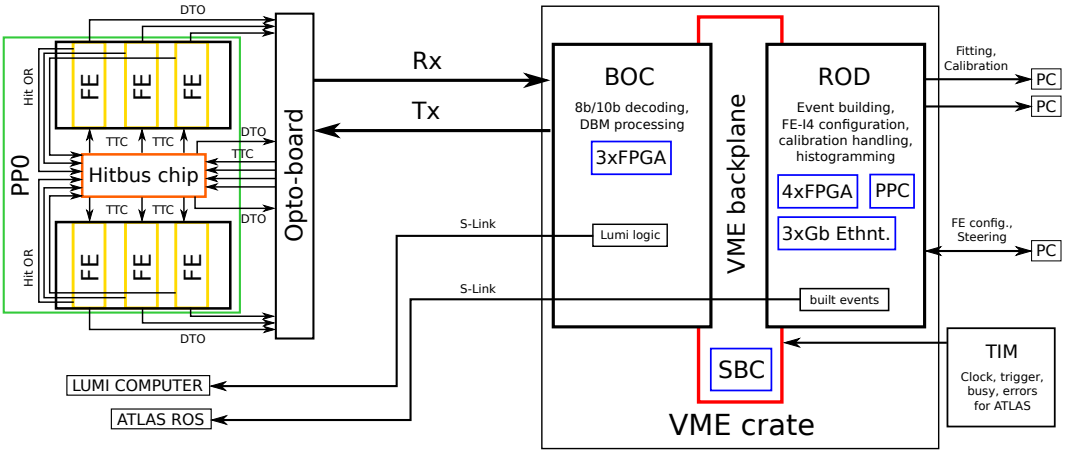

Figure 5.6.: Sketch of the DBM read-out chain. *Tx* stands for optical transmission and *Rx* for optical receiving lines.

chips. In normal data taking mode, it carries out event building and transfers the built events back to the BOC, which passes them on to the ROSes. It also forwards the trigger signals to the modules. In case of calibration, the ROD initialises the detector, generates clocks and triggers, collects the data, builds the events and carries out the calibration and monitoring. Histograms from calibration are shipped via Ethernet from the ROD to computers for fitting and storing. Module configuration works via the ROD. It hosts a *PowerPC* (PPC) and four *Field Programmable Gate Arrays* (FPGAs), while the BOC hosts three FPGAs.

A BOC-ROD pair can handle up to 32 read-out channels and for the DBM these are 24 at 160 Mbits/s from the DBM modules and 8 at 320 Mbits/s from the hitbus chips.

Because the DBM uses the same read-out and powering infrastructure as the IBL, it is operated as its 15th stave. Thus, the DBM utilises the BOC and ROD firmware and off-detector software are provided by the IBL. To allow dedicated luminosity measurements, a custom BOC firmware will be deployed in the future. As soon as the custom firmware is in place, operation of the DBM will allow two triggering modes. Firstly, the DBM will be triggered by the central ATLAS triggers and the resulting data will be shipped to ATLAS ROSes. Further, with secondary priority, the DBM will be self-triggered, as explained before. Data from self-triggering will be transferred to specific DBM luminosity handling computers.

A diagram of the complete DBM read-out chain can be found in Figure 5.6.

5.2.4. Powering

The powering of the DBM works per telescope. All modules of a telescope are connected to the same low voltage (for front-end chip powering) and high voltage (for sensor biasing) lines in parallel. The hitbus chip shared by two telescopes is powered separately. Powering lines are connected to PP0 by cables coming from *Patch Panel One* (PP1). PP1 is itself just a plug, from where cables are brought to *Patch Panel Two* (PP2). At PP2, the cables are plugged into regulator boards. The software system used for the control of the power supplies is called the *Detector Control System* (DCS). The graphical user interface used for the DCS is called the *Finite State Machine* (FSM).

5.3. Anticipated performance

5.3.1. Pointing resolution

To determine the orientation of the DBM modules, a simulation was done, calculating the pointing resolution in z-direction for particles in an energy range of approximately 0.5 GeV to 20 GeV emerging from pp-collisions [39]. This was done for two cases: finer segmentation in ϕ and finer segmentation in r. The results can be seen in Figure 5.7. They clearly indicate to orient the modules with the finer segmentation in r. The mean anticipated pointing resolution in z is then $\sigma_z = (5.9 \pm 0.7)\,\text{mm}$.

Because of a lever arm of about 10 cm in z and an even smaller one in r, curvature measurements are not possible with the DBM, cf. Equation (3.2). Therefore, a linear extrapolation was done in the presented simulation.

For an expression of the pointing resolution σ_p in $x \times y$, the following estimate is carried out. A DBM telescope is simplified by its first and last module located at radius r_1 and radius r_2 from the origin with position resolution $\sigma_1 = \sigma_2$, respectively. The FE-I4 is assumed to be a binary read-out device. With a pixel pitch of 50 µm in r-direction, the position resolution then is $\sigma_1 = \frac{50\,\mu\text{m}}{\sqrt{12}} \simeq 14.4\,\mu\text{m}$. Neglecting multiple scattering, using that the DBM is located about 1 m from the interaction point and that a telescope has a length of around 10 cm, the pointing resolution is estimated by Equation (3.3)

$$\sigma_p \simeq \sqrt{2} \cdot \sigma_1 \frac{r_1}{r_2 - r_1} \simeq \sqrt{2} \cdot 14.4\,\mu\text{m} \frac{100\,\text{cm}}{10\,\text{cm}} \simeq 200\,\mu\text{m}.$$

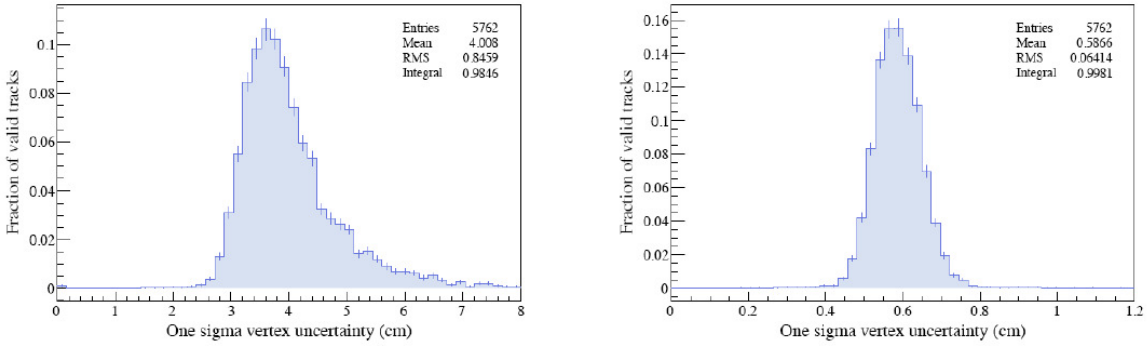

Figure 5.7.: The z-pointing resolution for different module orientations: on the left the finer segmentation is along ϕ, on the right along r. Curvature of tracks was not taken into account [39].

5.3.2. Luminosity precision

From the BCM efficiency and the larger $\eta \times \phi$-acceptance of the DBM, assuming a flat η distribution, there should be about 0.7 tracks detected in the total of eight DBM telescopes per proton collision.

The luminosity precision is estimated from this efficiency of 0.7 and the number of tracks in the DBM per second, which is conservatively estimated to 500 kHz at $\mu = 1$. These numbers yield 350 000 hits/s. Dividing this by the total of 3564 bunches gives 100 hits/BCID/s. Assuming a Poisson distribution of the hits per BCID, to get a relative statistical precision of $\frac{\sqrt{N}}{N} = 1\,\%$, 10 000 hits/BCID are needed. Thus, it takes about 2 min to reach a relative luminosity statistical precision of 1 %, which corresponds to the time of one ATLAS lumi(nosity) block[2]. At higher $\mu > 20$ (increasing the track rate), this should be reached within less than one minute. In 2017, the average pile-up was $\langle\mu\rangle = 38.1$ [45].

5.3.3. Beam spot resolution

For the determination of the beam spot, the usage of multiple track events is considered. At $\mu = 1$ more than about 15 % of all events are multiple tracks in the sensitive region of the DBM. The $x \times y$ beam position resolution within one lumi block is estimated to be smaller than 10 µm.

[2]When [39] was written; today a luminosity block is about one minute long.

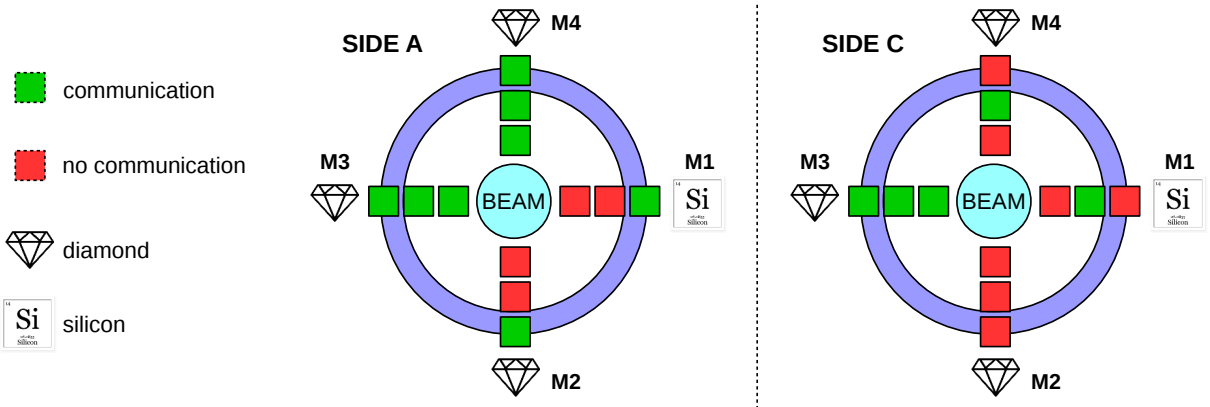

Figure 5.8.: The status of the DBM in ATLAS at the beginning of 2017. The clock-wise naming *M1* to *M4* of the telescopes can also be seen.

5.3.4. Radiation damage

The charge collection distance of the diamond sensors was expected to be more than 200 µm with an expected minimum signal charge of 7200 e prior to irradiation. To give values after irradiation, the expected flux is scaled from the IBL to the DBM by a factor of $\frac{1}{r^2}$, giving $2 \times 10^{15}\, n_{\mathrm{eq}}/\mathrm{cm}^2$. Taking this flux as a pion flux, a charge collection distance of more than 100 µm or 3600 e is predicted. The damage should not influence the data taking, as the FE-I4 should be tunable to thresholds of less than 2000 e.

5.4. Status of the DBM

The DBM was built and installed until the end of 2014. During the production, a total of 46 diamond sensors were produced and tested. Sensors that passed the requirements were installed in ATLAS. Due to too few diamond sensors passing the required quality criteria, two Silicon based telescopes were built and installed, leading to 18 diamond sensors and 6 Silicon sensors being used for the DBM [46].

Figure 5.8 summarises the status of the DBM in ATLAS at the beginning of 2017. It shows that 13 out of 24 modules are communicative, while 11 are not. First non-communicative modules were observed after low-voltage current drops shortly after the magnetic field of ATLAS was ramped, which are shown in Figure 5.9. The current drops were seen while the laser signal from the BOC was off. It was found that the opto-board sends random digital signals on the trigger and data lines to the modules in this kind of situation. A working hypothesis is that these random signals led to some kind of current oscillations. Within the magnetic field of ATLAS, current oscillations imply *wirebond oscillations*, as shown in Figure 5.10. The green arrows marked with "I" in Figure 5.10

show the direction of current flow, the blue arrows marked with "B-field" the magnetic field direction. Without a magnetic field, current simply flows through the bonds as shown in picture (1) in Figure 5.10. Picture (2) shows the bending of the wirebonds in a magnetic field with constant current flowing due to the Lorentz force. As current flow and magnetic field are about orthogonal for the DBM, the Lorentz force acts maximally. Picture (3) shows the situation when the current slighly increases – the wirebonds are bent more strongly. If current oscillations occur, the situation might be switching between picture (2) and (3). When reaching the resonance frequency, the wirebond may break, as shown in picture (4). Wirebonds breaking due to wirebond oscillations were studied, see Section 7.4. In addition to wirebond oscillations, a high current heats the wirebond and makes it even more fragile. Independently, a high current can lead to a wirebond fusing, as investigated in Section 7.3. It is supposed that communication to modules was lost due to wirebonds breaking in wirebond oscillations or wirebond fusing.

A broken wirebond can mean that communication is lost and that the power consumption of the FE-I4 is reduced. In contrast to the IBL, the DBM only uses one instead of three wirebonds for the powering connections, increasing their fragility. Figure 5.9 shows some current drops after the magnetic field was ramped. These fit into the picture of wirebonds breaking, in particular as communication was lost after these drops. Buried in the heart of Atlas, fixing or replacement of DBM modules is not possible until the next time the Pixel Detector including the DBM is brought to the surface. This will not be before the long shutdown for the HL-LHC upgrades in 2024 during which the whole ID will be replaced.

Multiple safety mechanism were installed to prevent wirebond oscillations and wirebond fusing for the future. These were interlocks in the powering system and adding the DBM to the IBL *fixed frequency trigger veto* (FFTV), which aims at suppressing wirebond resonance frequencies [54]. The IBL FFTV monitors the Atlas trigger frequency and stops triggers from being sent for a certain period of time to the modules, if they lie in a frequency range of 2 kHz to 40 kHz, in which the wirebond resonance frequencies of the IBL can be found. Additionally, it stops triggers from being sent, if large contributions of trigger frequency components in the wirebond resonance regime are found, originating from the Atlas trigger following the Lhc bunch filling scheme. The resonance frequencies of the DBM were studied and found to be very similar to the ones of the IBL. Carefully evaluating the next steps for safe operation, the DBM was not operated from April 2015 until 2017, with the exception of some small tests. Additionally, operation was limited by two issues

- in the DCS, some channels were swapped. In principle this meant that when turning

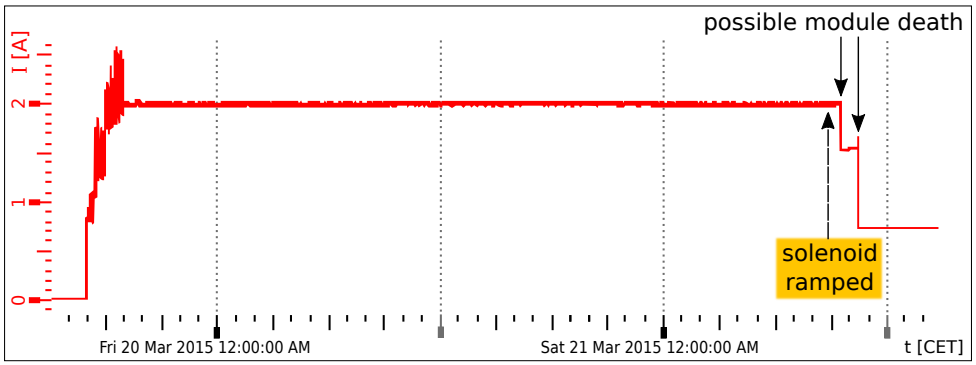

Figure 5.9.: Low-voltage current trend of side-C telescope M1 in March 2015. Communication with two out of three modules was lost after the current drops.

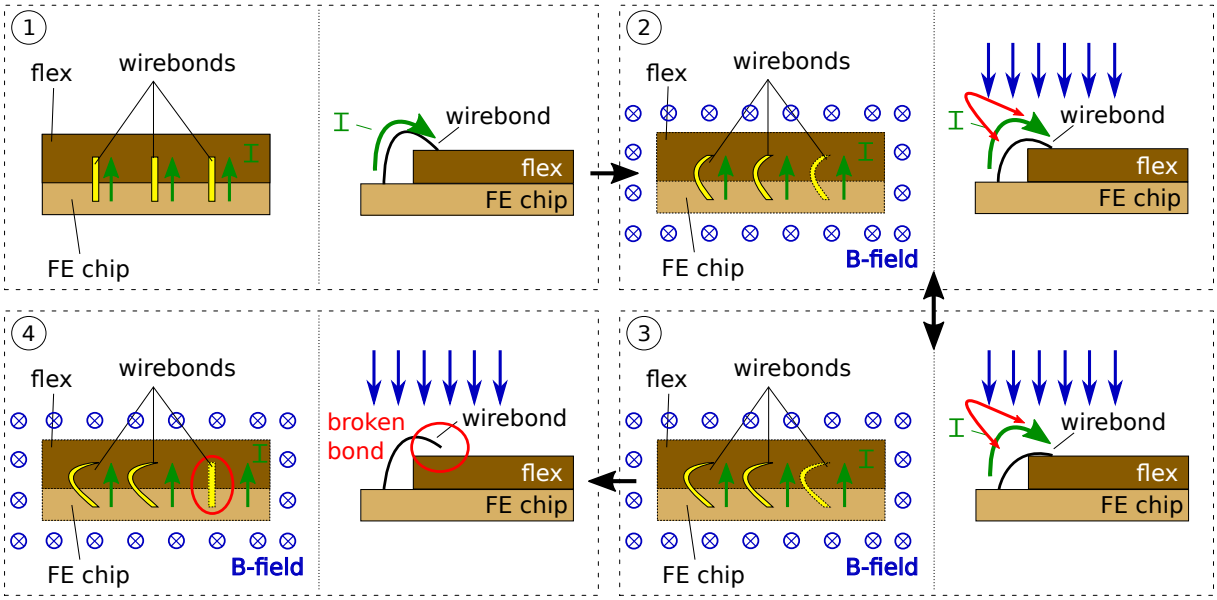

Figure 5.10.: Schematic drawing of wirebond-oscillations.

on what was labelled as channel 1 in the FSM, channel 2 showed an increase in voltage. This was identified as a software issue and it was unclear whether the problem was in the FSM or the DCS.

- as mentioned before, the DAQ is shared with the IBL. The IBL provided and installed some firmware and software updates, which were not adapted to the DBM.

6. Recommissioning of the DBM

Due to the *End-of-Year Extended Technical Stop* (EYETS), from December 2016 to May 2017 there was no magnetic field in ATLAS. This allowed the DBM collaboration to carry out tests and to recommission, without the fear of wirebond oscillations. The recommissioning effort at IP1 was aimed at powering connectivity issues, updating the state and alerts definitions in the FSM, and testing the safety interlocks. Furthermore, tests of the optical connections, of all of the modules, of the trigger propagation and run integration were foreseen.

The recommissioning will be described in Section 6.2 and the DBM operations 2017 will be summarised in Section 6.3.

6.1. The SR1 setup

First tests of the procedures for recommissioning were carried out on the DBM setup in SR1. The setup in SR1 is an exact copy of the setup in ATLAS, but consists of two telescopes only, with the intention of providing infrastructure for further development and testing of the DBM. A picture of the setup in SR1 can be found in Figure 6.1.

Since the setup was not working as expected, the following steps had to be taken to get it back into working order.

6.1.1. Cable tests

To ensure proper powering of the SR1 setup, the powering cables were tested. Therefore, the cable from PP0 to PP1 (the *type 1 cable*) was unplugged at PP1. Following the documentation, the resistance between a pad on PP0 and the documented pin on the PP1 plug was measured. The result was that some high-voltage lines, a redundant powering line for the hitbus chip, and a sense line for the FE-I4 low-voltage were open. A pin for the sense line of the hitbus chip voltage was damaged and potentially prevented a proper connection. Since the sense lines are crucial for operation of the front-end chips, the open line and the damaged pin were fixed. As no high-voltage was necessary for the planned tests in SR1, it was decided not to repair the lines rather than risking damage

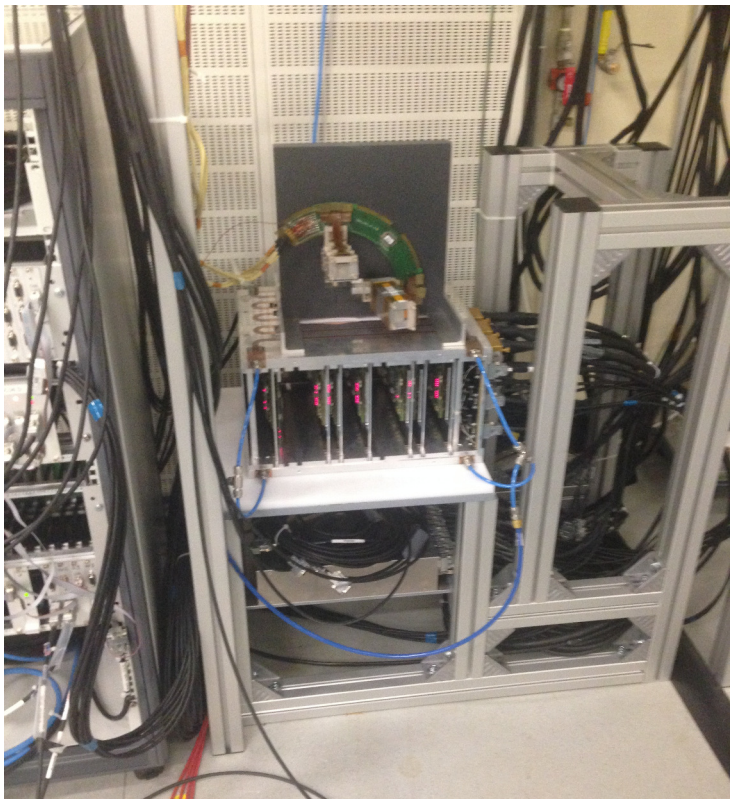

Figure 6.1.: The SR1 setup of the DBM inside of SR1 at the IP1 sight.

of other connections. During the process of testing and repairing the type 1 cable, the connector at PP1 was unplugged several times, damaging several more pins. The damaged pins on the connector could be repaired easily, however because of this fragility, it is not advised to unplug the type 1 cable at PP1 very often. Using the FSM, the setup in SR1 was powered. The voltages of all channels were cross-checked at the PP0 solder pads, which showed acceptable deviations from the set voltages. Fine-tuning of the calibration constants applied in the FSM to improve on these was postponed.

Testing the connectivity of the datalines between the FE and opto-board yielded six lines that were not connected at the opto-board. They concerned four of the six modules in SR1. Since most of the wires are hard to repair it was decided to replace PP0 altogether. Prior to the replacement, tests with the *Channel-Mapping tool* were carried out, because communication with two modules was expected, since the low-voltage powering and clock-, command- and data-lines to these were fully functioning. No module was found to reply.

The Channel-Mapping tool allows to test communication to modules on a very low level. It loops over all Tx-lines and broadcasts a configuration to all available modules. After sending a configuration on one Tx-line, the Channel-Mapping tool loops over all Rx-lines and attempts to read back the serial number of a module. Finally, it outputs

all tested Tx/Rx-combinations with the corresponding serial numbers found. Each FE-I4 has a *Geographical Identifier* (GeoID) between zero and seven, defined by the way certain wirebonds are connected. A module only reacts if addressed with its GeoID or with GeoID eight. For the DBM, an additional special version of the Channel-Mapping exists, in which the GeoID for each Tx/Rx-combination can be chosen. It is used for the setups in ATLAS and SR1.

Pictures of the cable tests can be found in Appendix A.2.

6.1.2. The square-board setup

As described above, the SR1 setup was modified by installing a newer version of the PP0 board together with the corresponding cables. A photograph of it can be seen in Figure 6.2a. In contrast to the previous setup in SR1, as well as to the setup inside ATLAS, the power services no longer break at PP1, but connect to PP2 directly. This eliminates the problems with damaged PP1 connector pins, making the test setup more reliable to operate. After installation, all powering lines, except the high-voltage ones, and clock-, command- and data-lines were tested with a multimeter and found to function. The powering via the FSM worked and the voltages measured across PP0 were in good accordance with what was set and shown in the FSM. However, still no communication with any module was possible. This was traced to the opto-board in SR1, which was broken. After replacement it was possible to communicate with some modules using a custom tool. When trying to read back the serial numbers with the Channel-Mapping tool though, it was not possible to communicate with any of the modules. As modules consume more power when configured, the Channel-Mapping tool was used separately for each GeoID on one telescope, and the current consumption was observed. For three GeoIDs a current step was seen, cf. Figure 6.2b, indicating that the modules of the telescope were configurable and that sending commands worked, but not receiving data.

To exclude the modules as the source of the problem, it was decided to test the modules of both telescopes in SR1 with a USBPix system [55]. A USBPix system allows an FE-I4 chip to be connected relatively easily to a computer via USB and run standardised tests of the module functionality. It takes care of both powering and data acquisition. In SR1, it was connected directly to the modules via the module flex, significantly reducing the complexity of the setup for debugging purposes. Each module was tested with the USBPix system, by carrying out a register test and running a set of scans (digital, analog, threshold, FE-I4 tuning). A scan is a procedure, during which each pixel of the chip is tested regarding a specific feature. In a digital scan, hits are injected into the digital part of the FE-I4 and the response of the chip is recorded. In an analog scan, a fixed amount of

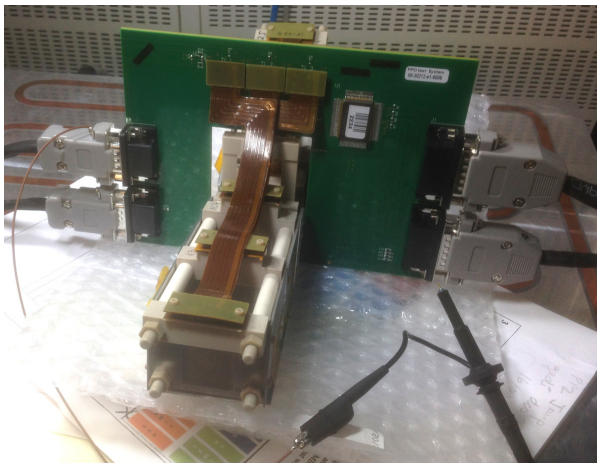

(a)

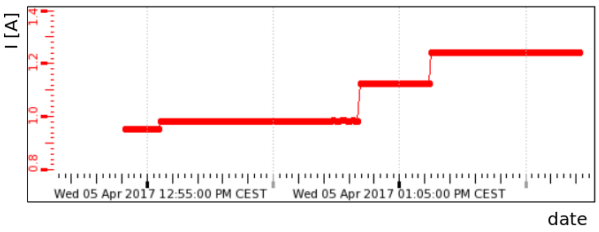

(b)

Figure 6.2.: (a) The square-board PP0 in SR1 with two telescopes installed. (b) The current increasing in three steps after individual GeoID configuration.

charge is repeatedly injected via the injection capacitor and the resulting response of each pixel saved. Digital and analog scan, allow one to understand, how well the individual pixels of a front-end chip are working. During a threshold scan, the amount of injected charge is varied and each charge is injected multiple times. Plotting the number of hits versus charge allows the discriminator threshold for every pixel to be deduced. In a tuning procedure, the registers of certain parts of the FE-I4 are altered, to yield a certain threshold or ToT distribution (for a fixed injected charge) for example.

The tests showed, that five out of six modules work fine when operated with the USBPix system. More details can be found in Appendix A.2.

To ensure the integrity of the opto-board, a specific test setup was used, confirming that it was intact. Using the Channel-Mapping tool, communication with all working modules in SR1 could be established at some point after the opto-board test, although it was somewhat unstable for most of them. This allowed the mapping of the Tx- and Rx-lines to the respective modules to be cross-checked. The only component that had not been tested for functionality so far were the flex cables. They were tested by connecting them to a USBPix system with a well-known, functioning FE-I4 in a lab and performing a set of scans. The tests indicated that one of the flex cables is broken. Back in SR1 the flex cables were attached such that the broken one was connected to the broken module. By swapping the order of how the flex cables of the fully functioning telescope were connected to PP0, it was found that if connecting a module to the middle flex cable plug on PP0, a response was reliably seen with the Channel-Mapping tool.

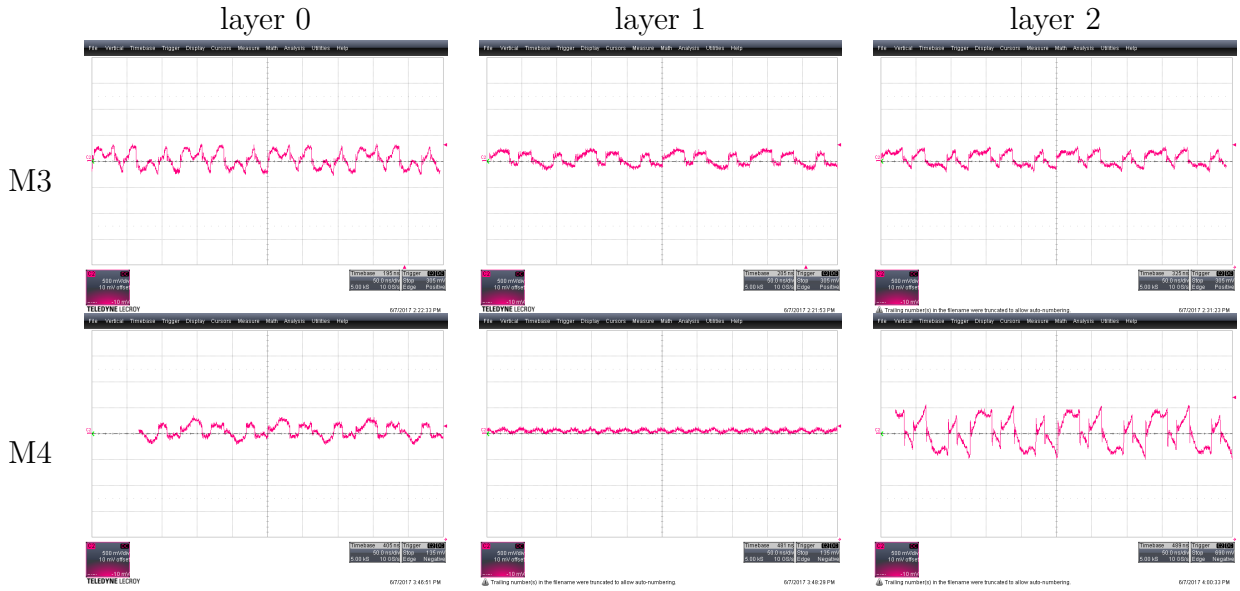

Figure 6.3.: The signal of the data-lines of the modules in SR1 measured with a differential probe on PP0 for telescopes M3 and M4. M4-layer 1 was broken. In `Chipscope`, M3-layer 1 reported the idle signal and all other functioning modules showed an idle signal with bit flips.

6.1.3. Oscilloscope tests

To improve the stability of the communication with the modules, the signal integrity was tested with a differential probe. The signal of the clock-, command- and the data-lines were probed on PP0. With help of the Channel-Mapping tool, a configuration was sent to all of the modules. The clock-line showed good signal quality and all of the command-lines showed a similar signal during configuration, see Appendix A.2. The data-line signal changed to a periodic signal after configuration, as shown in Figure 6.3. The 8b/10b encoded idle signal was expected to be observed. One of the modules shows a sine wave on its data-line after configuration. This is the same module that had been found non-responsive during the USBPix tests. Further, it is visible in Figure 6.3 that the data-line signal is of different quality for the different modules. This is probably due to different impedances of the data-lines between PP0 and the opto-board. It indicates that all known good modules still work in the DBM test setup, albeit with varying reliability of the data connection.

The observation of distorted idle signals was verified at the BOC using a software called `Xilinx Chipscope Analyzer` and a command line tool called `RxDebug`. The software, referred to as `Chipscope` from here, allows the raw bit stream of all optical fibres connected to the BOC to be read. With `RxDebug`, the BOC Rx-line to be read out with `Chipscope` can be selected. The bit stream from each module was read several times, also as a

function of the phase shift between the optical signals from the opto-board and the BOC receiver. As a significant difference between the different phases was not always observed, this should be repeated. The presented results refer to the phase found, at which the signal was most similar to the idle signal. In accordance with previous observations, one module reported the idle signal after configuration; four modules showed a "distorted" idle signal, i.e. an idle signal with a sporadic or a continuous bit flip; and the remaining module's signal was not similar to the idle one, as this was the broken module. The typical output in `Chipscope` for the tested modules is written in the caption of the oscilloscope measurements in Figure 6.3.

The distorted idle signals in the oscilloscope and the `Chipscope` measurement strongly suggest that the Rx-lines from the modules to the opto-board are the reason for unreliable communication of four out of five modules. This is probably because of incorrectly matched impedances.

6.2. Reintegration of the DBM into ATLAS operations

This section deals with the recommissioning of the DBM setup inside of the ATLAS detector. The nomenclature for labelling is (side)-M(telescope number) for a telescope and (side)-M(telescope number)-(module number) for a module, where the numbers are taken from Figure 6.5.

6.2.1. Powering issues addressed

Modules unable to be powered

The low-voltage for some front-ends could not be turned on. This was because the `STARTUP` procedure did not take DBM specifics into account and it was adapted accordingly. The `STARTUP` procedure turns on the PP2 boards and configures them. Furthermore, if not being locked out, a test voltage is applied to all telescope low-voltage channels and the sense line response is probed. During this procedure the hitbus chip is turned off, which transports clock and commands. It was shown in SR1 that the hitbus chip outputs a well defined, constant signal when being off and hence does not potentially endanger any modules during the sense line tests.

Swapped powering channels

As mentioned previously, some powering channels were swapped. This concerned the setting of the low-voltage value of all telescopes on side C. Correcting some FSM routings and clearing the FSM cache resolved the issue.

Redefining the FSM state and alert limits

The DBM FSM allows for alerts. Alerts are defined by limits on the current or the temperature of an object and the available alerts are `OK`, and in order of severity from lowest to highest, `WARNING`, `ERROR`, `FATAL`. For the DBM, the FSM is configured such that a component going into `FATAL` will be switched off immediately. This is used, for example, to prevent a current consumption on the low-voltage lines which is too high, potentially causing wirebond fusing. Thus, careful alert settings for the telescope low-voltage channels was required. The alert current limits were defined tightly above the current consumption during data-taking such that the `FATAL` limit was less than 100 mA above it. During operations, the alert limits had to be adjusted continuously, in particular in regard to the TID-effect, see Section 6.3.2. An SMS notification was configured to inform the DBM/BCM on-call shifter about occurring alerts.

6.2.2. Reintegration into the ATLAS read-out stream and module tests

Large parts of the recommissioning dealt with the reintegration of the DBM into the ATLAS Pixel DAQ, and with module tests. To do so, a fully functioning copy of the ATLAS Pixel DAQ software was set up for the DBM, permitting independent and more specific tests. Because the ATLAS Pixel DAQ had been updated since the last time the DBM was operated, the command propagation through the DAQ to the modules and their response was tested, to ensure full compatibility with the DBM. The structure of the DAQ is shown in Figure 5.6.

Testing of optical connections

For tests on correct optical line addressing of the ATLAS Pixel DAQ software, the `Pixel Console` and a tool called `IblBocMon` were used. The `Pixel Console` is a GUI to configure, run scans on and tune individual and multiple modules of the ATLAS Pixel Detector. Only the modules marked as communicating in Figure 5.8 are available in the `Pixel Console`. The command line tool `IblBocMon` allows for multiple operations in the BOC.

For example, supervision of the number of commands sent to a Tx-line, and changing of the BOC Rx-line phase shifts are possible.

By trying to configure a certain module with the `Pixel Console` and looking at the number of commands sent to the Tx-lines with `IblBocMon`, the propagation of FE-I4 commands from software to BOC was tested. The same procedure was carried out while running various scans. The Tx- and Rx-line of each module are known from installation and were compared to the output of `IblBocMon`. A bug in the Tx-line masking of the ATLAS Pixel DAQ software was found and removed. Thus, the command propagation to the Tx-lines was validated.

For the Rx-lines, the following test was carried out for one module: an analog scan was executed with the `Pixel Console` and the returned data-stream checked with `Chipscope` and `RxDebug`. The Rx-line and the format of the returned data of this module were found to be as expected. Since the `Pixel Console` throws an error if a module does not return the idle signal after being configured, this test was only repeated with other modules during recommissioning, if unforeseen communication problems occurred.

Configuration Database

The *configuration database* of the ATLAS Pixel Detector contains the configurations of all modules and connectivity information. All actions on modules from the `Pixel Console` rely on this. Two DBM modules had corrupted entries in this database and were therefore not operable. Multiple actions were required, including the repeated creation of new database entry `Root` files, re-establishment of internal database links and the manual change of certain database entries regarding the modules' connectivity, to recover the two modules.

Module tests

All modules were tested intensively during the recommissioning phase. For the communicating modules from Figure 5.8, a set of scans (digital, analog and threshold) was run with the `Pixel Console` to ensure full functionality. Adaption of some Rx-line phase shifts in the BOC was necessary, identified by certain errors in the `Pixel Console` and a signal different from idle in `Chipscope`. Some analog scans showed unexpected results with more than 1000 hits, when only 50 had been injected, see Figure 6.4. This was due to a very low threshold in the configuration. To avoid such undesired configurations, all configurations in the configuration database were compared to known configurations and corrected accordingly. Finally, all modules except for C-M3-7 were found to be in perfect working condition.

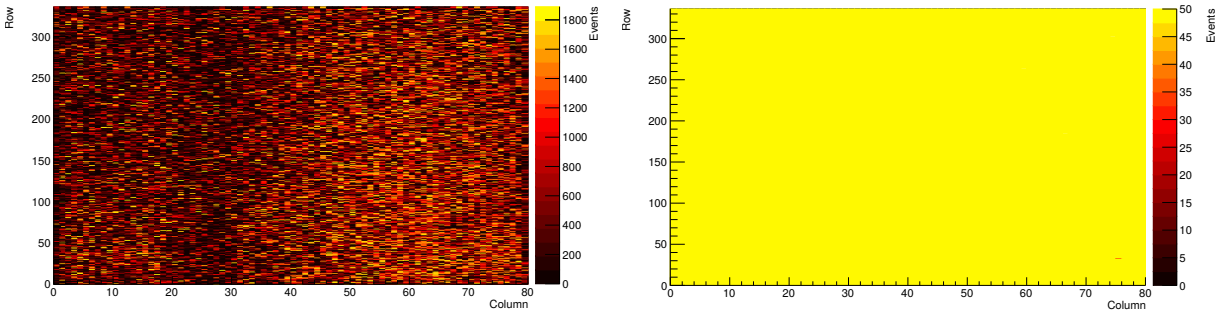

(a) *(b)*

Figure 6.4.: Two dimensional hitmap corresponding to each individual pixel in a module, with the columns on the x-axis and the rows on the y-axis. Colour coded indicates the number of hits resulting from an analog scan with 50 injections and (a) a too low threshold leading to noise hits, (b) the expected output.

For all of the non-communicating modules and for C-M3-7, the serial number could not be read back with the Channel-Mapping tool. The Channel-Mapping tool at IP1 has fixed GeoIDs for all module Tx/Rx-combinations and was able to read back all serial numbers during initial commissioning in 2015. It sends a configuration to all available modules. Using `Chipscope` and `RxDebug`, the response of the non-communicating modules and C-M3-7 before and after configuration with the Channel-Mapping tool were compared. A change could hint to modules receiving commands correctly, but their reply being distorted somehow, for example by a bad BOC phase shift. In that case, an Rx signal similar to the idle one is expected. For some of the modules, the returned bit-signal changed after configuration. However, no particular similarity to the expected idle signal was observed. The response after configuration was studied for three hitbus chip voltages for telescope C-M2, without modules changing their signal in `Chipscope`. No low-voltage current increase after configuration was seen for C-M2 in any situation, either. A current increase after configuration is expected and would have shown that commands are received by the modules. Special effort was devoted to C-M3-7, which had been communicating until 2017. It was, therefore, unclear whether the lack of communication to C-M3-7 was due to the user or the module. A higher low-voltage supply current did not change the responsiveness. In contrast to all of the other non-communicating modules, a configuration could be sent to only C-M3-7 through the `Pixel Console`, because it had been communicating until 2017. For the other modules, the Channel-Mapping tool had to be used, which sends a configuration to all available modules. Consequently, an attempt was made to send a configuration to just C-M3-7. Despite making sure that commands were sent to the correct Tx-line, that the intended Rx-line was considered, that the con-

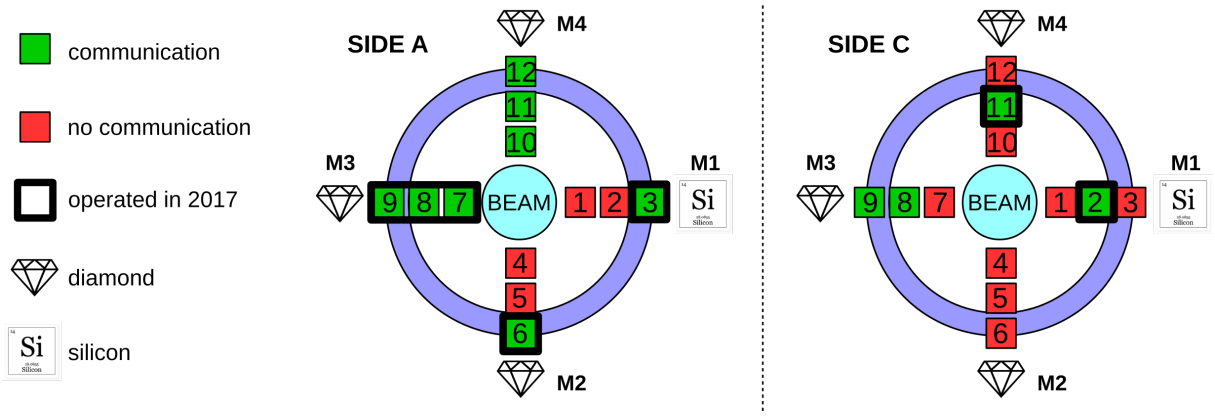

Figure 6.5.: The status of the DBM in ATLAS in June 2017. This drawing shows the modules that were included in ATLAS data-taking in 2017.

figuration in the configuration database was correct, and that the module was potentially powered, no increase in the low-voltage current consumption was observed. Hence, it was concluded that C-M3-7 has to be classified as non-communicational. The status of the DBM after these tests can be found in Figure 6.5.

No general conclusion could be reached as to why modules stop communicating. Should the issue be broken wirebonds, then a non-increasing low-voltage current can mean broken powering, clock or command wirebonds. Because clock and commands are transported via the hitbus chip, also a wrong configuration, a too low operating voltage or other user faults concerning the hitbus chip could prevent communication. Furthermore, if a current increase can be observed after configuration with the Channel-Mapping tool, a (return) data wirebond can be broken. The FE-I4 itself, opto-board, optical fibres or the optical components of the BOC could further be an issue.

Trigger tests

To assure smooth integration into the ATLAS data-taking, trigger and stop-less removal tests were done. The former meant issuing a trigger from a central ATLAS instance and checking whether data from the correct DBM modules was returned and that no trigger related error messages were shown. Stop-less removal means excluding a module or a ROD and all devices connected from ATLAS data-taking, without having to hold the ATLAS trigger. The stop-less removal tests were necessary to ensure that the DBM modules could be excluded from data-taking without causing dead time in ATLAS.

Two types of trigger tests were performed: one with a local Pixel Detector trigger (Local Trigger Processor, LTP) and one with a central ATLAS trigger (Central Trigger Processor, CTP). Both tests showed that the trigger propagation works and that the returned data

is transported correctly. During the LTP tests a mismatch of the BCIDs reported per trigger by the front-ends to the ROD was found. It could be reproduced that this occurred, since the DBM was operating one module on one side of the interaction point only. As a solution, it was proposed to operate more than one module per interaction point side.

During both, LTP and CTP tests, stop-less removal of the DBM ROD was carried out, without any issues observed. The stop-less removal was requested manually in these cases. However, it can also happen automatically if the ROD or a front-end go busy. They are then removed from data-taking to prevent further issues. Automatic stop-less removal worked when the whole ROD was in the busy state, but not when one front-end went busy.

6.3. Operations

After successful recommissioning of the DBM, it was decided to take part in ATLAS data-taking. First stable beams were on the 23rd of May, with module C-M1-2 being included.

6.3.1. General issues

Read-out window

The FE-I4 chip supports triggering itself up to 16 times with a time distance of 25 ns between each trigger, after an external trigger signal has arrived. Additional triggers by the FE-I4 are needed for timing scans (see below). They further allow small charges just above threshold to be read out because their signals take longer to reach the threshold. This is a property of the amplifier of the FE-I4, which is illustrated in Figure 6.6. Small charges appear, for example for diamond sensors or during calibration. If no additional triggers are issued by the FE-I4, hits of small charges might be lost and the efficiency of diamond sensors, for example, is reduced. Conversely, the more consecutive FE-I4 triggers are executed, the higher the current consumption of the FE-I4 becomes after a trigger arrives. Wirebond oscillations with larger amplitudes and more destructive potential could be the consequence. Furthermore, if an ATLAS trigger arrives, while the FE-I4 is still initiating triggers, the ATLAS trigger will be ignored. The number of consecutive triggers issued by the FE-I4 is called the *read-out window* and measured in units of 25 ns, which corresponds to the time interval between two LHC bunch-crossings. Therefore, the unit is abbreviated BC. For the DBM operation a read-out window of 1 BC was chosen after initial operation and timing (see below), to assure safe operation and consistency with the other ATLAS subdetectors.

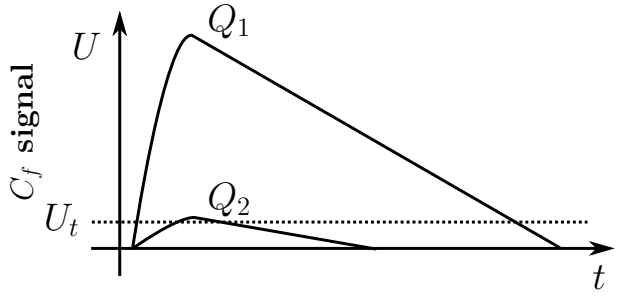

Figure 6.6.: A smaller charge yields a signal that crosses the threshold later than a larger charge arriving simultaneously at the FE-I4.

Timing

The central Atlas clock is synchronised to the Lhc bunch-crossings in Atlas. When reading out the DBM with a read-out window of 1 BC, synchronisation of the modules' clocks to the central Atlas clock is necessary to not miss hits, to associate hits in the DBM to hits in other Atlas subdetectors, and to associate hits from the modules of one telescope to each other. The latter is required if tracking is intended to be carried out with the DBM. That hits can be missed is illustrated in a simplified situation in Figure 6.7. In the top, hits from a collision occur between two module clock cycles. Since there may be some small jitter in the interaction time and the clock signal supplied to the readout chips, some hits will occur in the clock cycle before the trigger arrives and be missed. In the bottom situation, the module clock and Atlas clock are synchronised and hardly any hits occur outside of the clock cycle in which the trigger arrives. The clock of each module can be delayed with respect to the central Atlas clock in the BOC and TIM. The modules' clocks and the central Atlas clock are synchronised in so-called *timing scans*. In a timing scan, the delay parameters for each module are varied during a run and the number of hits per setting recorded. Broadly speaking, the delay parameters with the most hits is the one where the modules' clocks is synchronised to the central Atlas clock. A timing scan is a standard, automatised IBL procedure, which requires special Atlas trigger settings or Lhc fills, and typically a read-out window of 3 BC. Timing scans were performed and the module timing adjusted accordingly for some of the modules.

DQ plots and naming

The *Atlas Data Quality group* (DQ) provides plots for shifters and experts showing the performance of an Atlas subdetector. For the DBM for example, ToT histograms, reported module and ROD errors, module occupancy and many more are provided for an entire Atlas run. The DQ histogramming was adapted to the DBM during initial

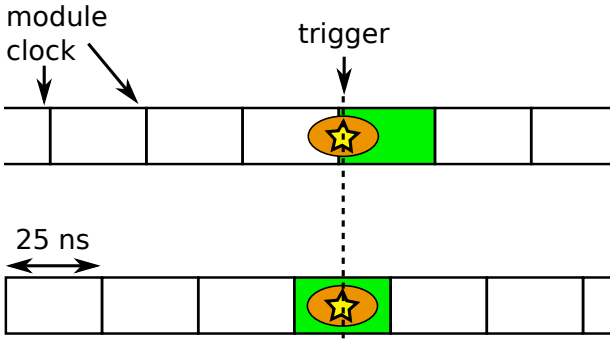

Figure 6.7.: The drawing shows how the hits are distributed over the module clock before synchronisation of the module and ATLAS clock (top) and after (bottom).

operation to improve usability for shifters. Continuous enhancement is ongoing.

ToT=0 problem

At initial operation, DQ histograms filled with the ToT of each hit showed entries with ToT=0. A ToT of zero represents no hit and should not be reported by the FE-I4. The ToT=0 entries were caused by a bad configuration of the FE-I4[1], which was corrected for all modules.

De-synchronisation errors

A mismatch of the BCIDs or the L1IDs returned by the modules of one side of the interaction point causes the ROD to throw an error message, called *de-synchronisation error*. Minimizing the number of de-synchronisation errors is important for good tracking performance. In comparison to the IBL, the DBM had orders of magnitude more de-synchronisation errors. Because these were initially traced back to operation with one module per side of the interaction point, a change of the ROD firmware was made to solve this. However, the error was not removed and still apparent when operating with multiple modules per side.

6.3.2. The TID-effect

During operation, the DBM observed a significant increase in the telescope low-voltage current consumption if the available modules from this telescope were operated for a longer period of time. This can be seen in the current trends in Figures 6.8a–6.8c. The IBL has observed a similar effect in 2015 and 2016, as shown in Figure 6.9 [56]. It shows the mean

[1] `HitDiscConf`=0 should always come with `SmallHitErase`=1.

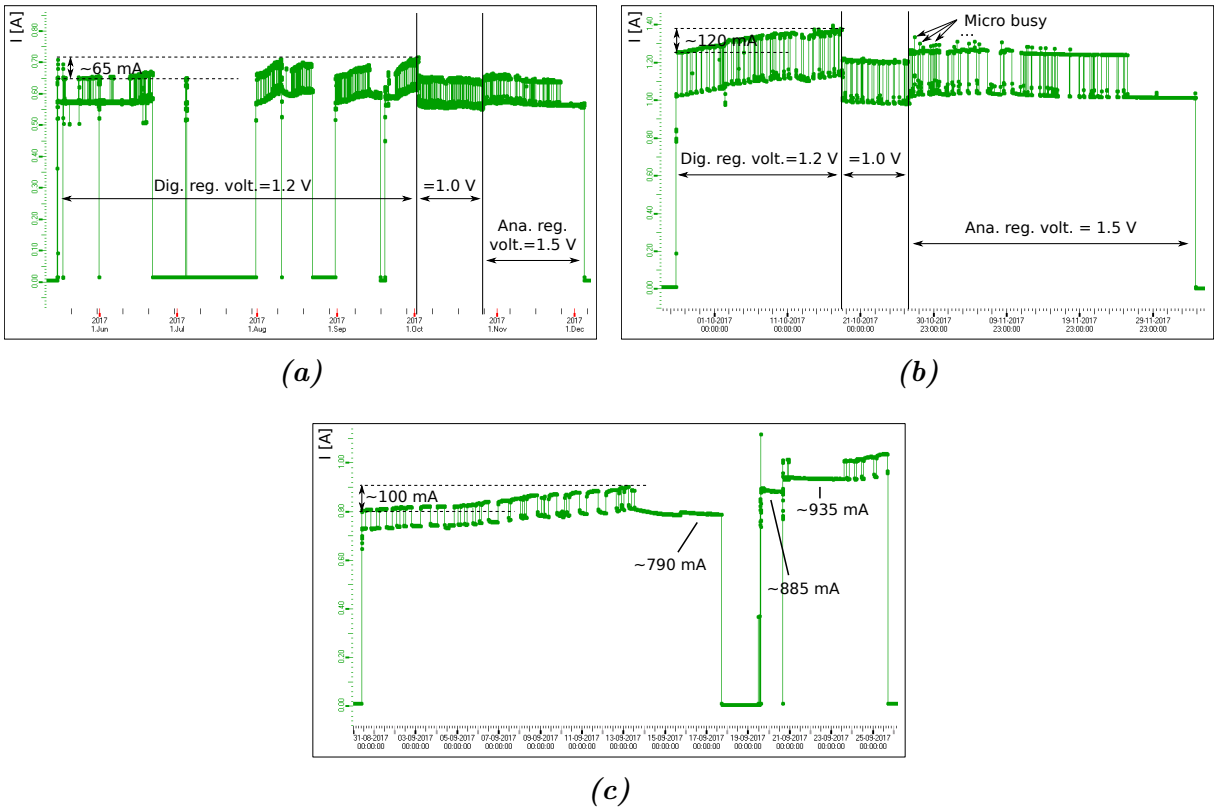

Figure 6.8.: The current trend of (a) C-M1 and (b) A-M3 for their entire operation period and (c) A-M2 between the 31. of August and 26. of September 2017.

IBL low-voltage current as a function of integrated luminosity for 2015 and 2016. The low-voltage current increases initially and is reduced after brief periods without operation, but then rises again. After longer operation, the current consumption generally stabilises and slightly decreases. Studies were conducted for the IBL to understand the origin of the current increase and propose a method to reduce it [57, 58]. The current increase was found to depend on the Total Ionising Dose (TID).

During irradiation, positive charges resulting from ionisation are trapped inside of the shallow trench isolation (STI) oxide layer of the NMOS transistors used inside of the FE-I4. They increase the leakage current of the transistors. This effect is countered by traps that form at the Silicon oxide – Silicon boundary through radiation, predominantly trapping negative charges formed by ionisation. The negative charges arise with more TID than the positive ones. At large TID, the traps filled with negative charges dominate. It is therefore expected that the low-voltage current increases with TID, peaks and then decreases again [59]. The different charges forming with TID in an NMOS transistor are shown in Figure 6.10. A parametrisation of the low-voltage current dependence on

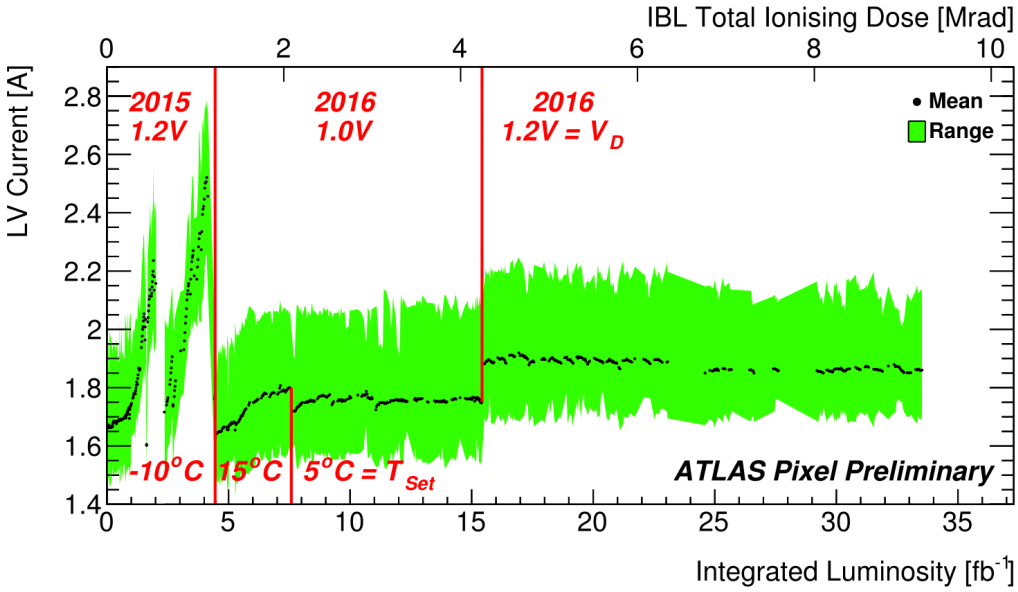

Figure 6.9.: The mean and range of the IBL low-voltage current versus integrated luminosity and TID for 2015 and 2016. Operation temperature and digital regulator voltage are marked [58].

the TID is presented in [60]. Since most of the NMOS transistors on the FE-I4 can be found on the digital part of the chip, the current consumption peak of the digital part is expected to be more pronounced than of the analogue part.

The IBL studies on the current increase showed two main dependencies: the low-voltage current peak is higher, the lower the temperature and the higher the dose-rate, as shown in Figure 6.11. The change of the digital and analogue supply current with TID are shown in Figure 6.12. Irradiation was done in this case at room temperature and a dose rate of 3 Mrad h^{-1} until 7.5 Mrad had been accumulated and at 4 Mrad h^{-1} for the remaining time. As expected, the figure shows that the current increase is dominated by the digital

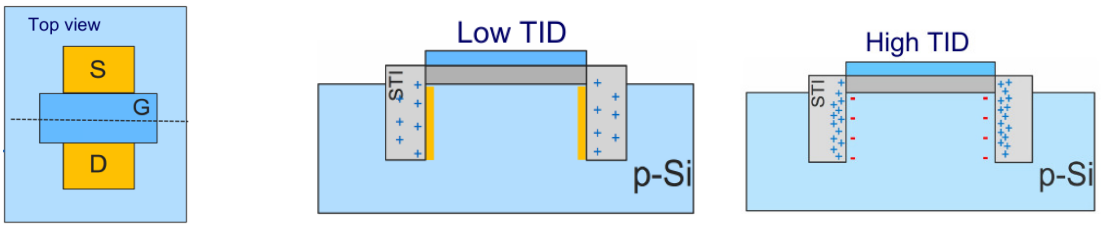

(a) *(b)* *(c)*

Figure 6.10.: (a) Top view of an NMOS transistor. S, G and D abbreviate source, gate and drain. (b) Irradiation leads to positive charges filling the traps in the STI. (c) With higher TID, traps form in the Silicon bulk, which are predominantly filled with negative charges.

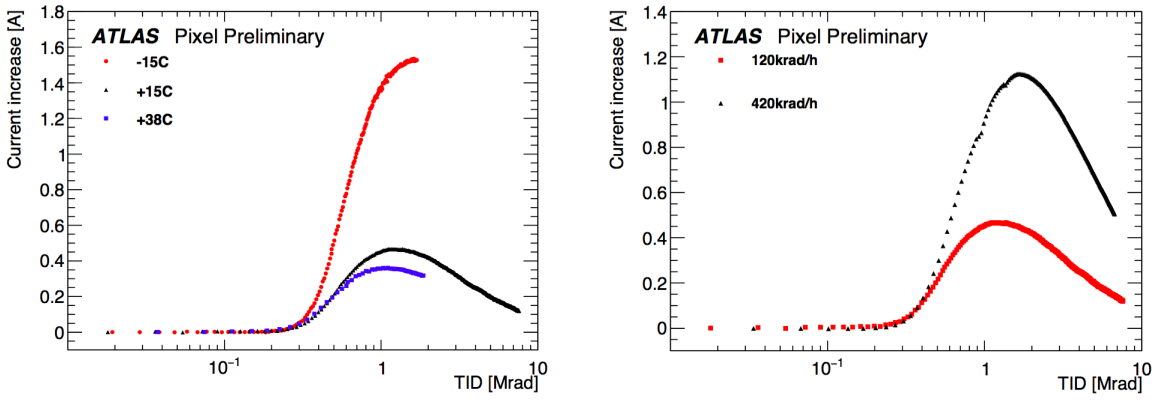

(a) *(b)*

Figure 6.11.: (a) The low-voltage current increase as a function of TID for different temperatures at a constant dose-rate of 120 krad h^{-1} [57]. (b) The low-voltage current increase as a function of TID for two different dose-rates at a temperature of 15 °C [58].

current. In the first irradiation period, irradiation was done in intervals, yielding the successive parabola shapes in the current trend. Following these results, the IBL lowered the digital regulator voltage and increased the operation temperature, which is marked in Figure 6.9, to reduce the current consumption during operation.

For the DBM, because of the peculiar wirebond situation, keeping the current as low as possible was paramount. In comparison to the IBL, the DBM has a lower dose rate (being further away from the interaction point) and a higher operation temperature of approximately 10 °C, which cannot be altered. Therefore, modification of the digital and analogue regulator voltage was the sole possibility to reduce the low-voltage current consumption. To ensure full functionality of the FE-I4 charge collection, only the digital regulator voltage was lowered, as marked in Figure 6.8a and Figure 6.8b. For telescopes with one communicating module a maximum low-voltage current of 1 A was defined.

The IBL studies indicate that the low-voltage current peaks at a TID of 1 Mrad to 3 Mrad, when a module is operated. To anticipate the behaviour of operated DBM modules, it was estimated, when this point will be reached. Using an ATLAS TID simulation [61], the dose rate was crudely estimated to between 0.1 Mrad/fb^{-1} and 0.15 Mrad/fb^{-1}. Thus, the current peak of a module should be reached at an integrated luminosity of about 10 fb^{-1} to 30 fb^{-1}. The peak low-voltage current value for the DBM is difficult to estimate, since the damage of a module when being switched off is not understood quantitatively.

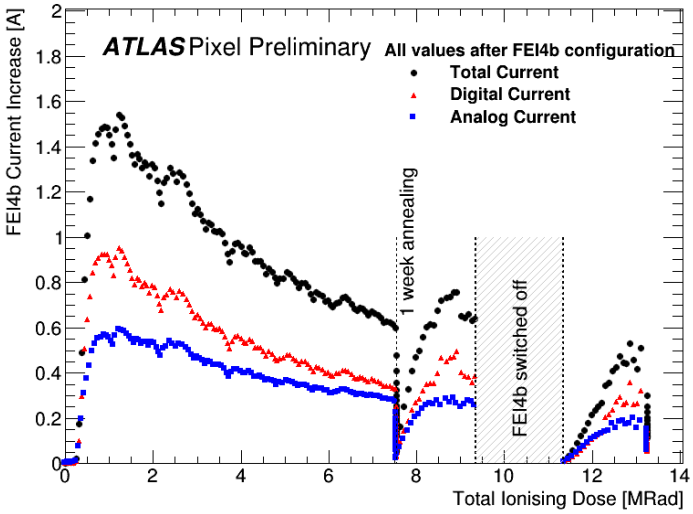

Figure 6.12.

Figure 6.13.: The digital and analogue regulator current and total low-voltage current consumption as a function of the TID [58].

Module	Sensor	Op. from...	...until	Op. stopped, because	Timing scan?
A-M1-3	Si	19.09.2017	02.10.2017	Spikes in current trend	Yes
A-M2-6	Diam.	31.05.2017	25.09.2017	Current consump. above 1 A	Yes
A-M3	Diam.	25.09.2017	05.12.2017	–	No
C-M1-2	Si	15.05.2017	05.12.2017	–	Yes
C-M4	Diam.	19.09.2017	14.10.2017	Spike in current trend	Yes

Table 6.1.: The operated modules in 2017. A-M3 stands for all three modules of the telescope.

6.3.3. Operated modules in 2017

The modules operated in 2017, with operation time, stopping reason, and whether a module was part in a timing scan or not, are shown in Table 6.1.

Current increase due to TID

If only one module of a telescope was communicating and operated, the change of the low-voltage current consumption of a telescope was associated with this module, to ensure maximum safety. The influence of the TID on the low-voltage current consumption was observed for all operated modules. The current consumption peaked at an increase of 65 mA for C-M1-2 and 120 mA for A-M3, compare Figure 6.8a and Figure 6.8b. The digital regulator voltage was decreased to 1 V for these modules to lower their current consumption. The digital regulator voltage of A-M3-8 was thereby lowered too far, which

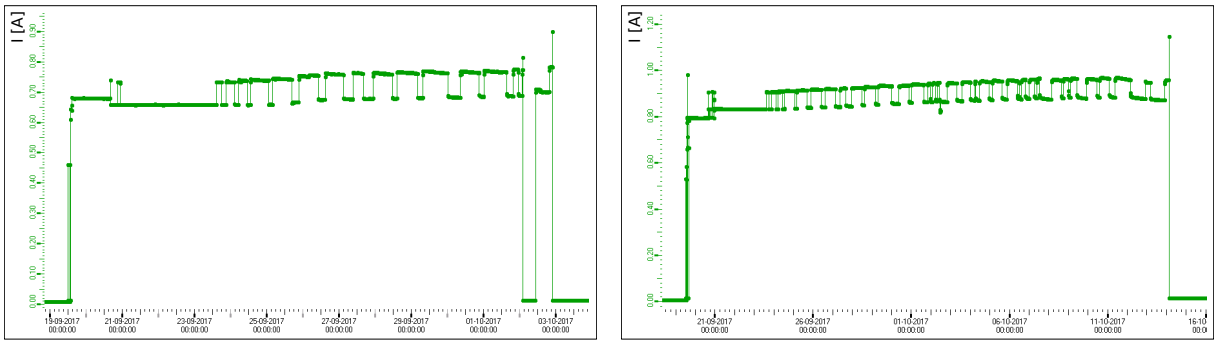

(a) *(b)*

Figure 6.14.: The current trend of (a) A-M1 and (b) C-M4.

prevented proper functioning and led to lost hit information. As this was noticed in the last weeks of operation, fixing it was postponed to the *End-of-Year Technical Stop* (EYTS) from December 2017 until February 2018.

For A-M2-6 the low-voltage current consumption increase because of the TID was so large that the telescope current exceeded the defined maximum of 1 A and was turned off, see Figure 6.8c. Special attention shall be drawn to the two current plateau steps of 95 mA and 50 mA after power-cycling A-M2. These kind of steps were not observed with any other DBM module. Relation to non-communicating modules of telescope A-M2 seems likely.

Current spikes

Both A-M1-3 and C-M4-11 were removed from operation after a few weeks, due to a spike in the low-voltage current, see Figure 6.14.

Current drops

During operation, low-voltage current drops of about 70 mA on telescope C-M1 were seen without apparent cause. For an example of these current drops, accompanied by a change in temperature with temperature sensor on C-M1-2, see Figure 6.15. To ensure that the current drops did not influence the data-taking of C-M1-2, the number of hits over the number of events of one luminosity block was plotted for selected luminosity blocks of run 327265. An obvious change in the occupancy during a current drop was not visible. However, the analysed period did not cover many events without current drops. Therefore, the occupancy analysis should be repeated for a longer period of time, such as the entire run.

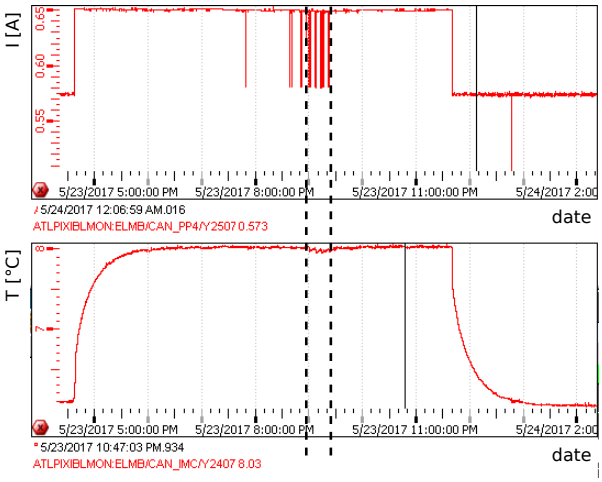

Figure 6.15.: Low-voltage current and module temperature versus time for telescope C-M1 with current drops of approximately 70 mA for run 327265.

Micro busies

Micro busies occurred during the operation of telescope A-M3 and are marked in Figure 6.8b. The hypothesis is that they result from *Single Event Upsets* (SEUs). During an SEU, a bit flips in a register of the FE-I4. SEUs originate from radiation damage. Reconfiguration of all modules when the ATLAS *Event Counter Reset* (ECR) signal arrives every 5 s was set up for the IBL to solve SEUs and thus micro busies.

Other issues

In contrast to all other operated modules, the modules of A-M3 were not part of a timing scan. For two modules, the timing parameters had to be adjusted manually to see any hits at all.

Together with the IBL, the analogue regulator current was increased to its maximum of 1.5 V for C-M1-2 and all modules of A-M3 to minimise a possible increase of the electronics noise.

6.3.4. Module occupancy comparison

The occupancies of all modules included in data-taking are shown colour coded in Figure 6.16 for run 336567. The labels in the squares identify the modules and the sensor type is given in brackets. The threshold resulting from a threshold scan is given in electron charges. That Silicon sensors typically yield more electrons per penetrating particle than diamond sensors is visible. For the Silicon modules, the occupancy is further dependent

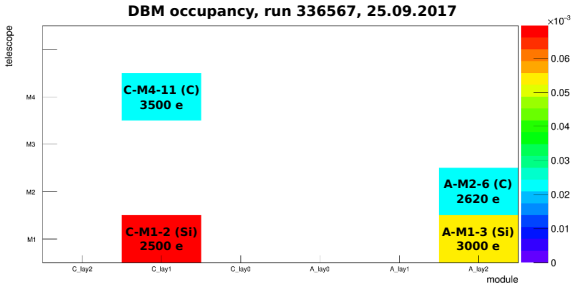

Figure 6.16.: The occupancies of the DBM modules included in run 336567.

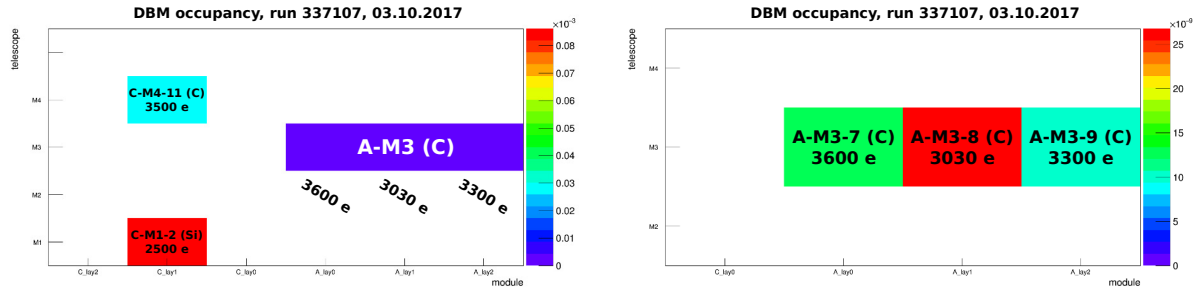

(a) ***(b)***

Figure 6.17.: The occupancies of the DBM modules included for (a) run 337107 and (b) a magnification of the occupancies of the modules of telescope A-M3 of run 337107.

on the threshold. Occupancies of the modules of telescope A-M3 are shown for run 337107 in Figure 6.17.

For the modules A-M2-6 (diamond) and C-M1-2 (Silicon) a pixel granular hit map at comparable thresholds for run 325713 was made, see Figure 6.18. It again confirms that diamond sensors yield far fewer hits than Silicon sensors, since fewer charges are created, see Table 3.1. An increase of occupancy for diamond modules can hence be achieved by lowering the FE-I4 threshold, for example to about two to three times the noise floor. A dedicated tuning procedure to lower the threshold of an FE-I4 to that level will be discussed in the next section.

6.4. Implementation of a Low Threshold Tuning for the DBM at the ATLAS detector

The idea of the *Low Threshold Tuning* (LTT) is to bring the threshold of the FE-I4 to just above the noise floor. The LTT tuning algorithm was developed in 2017 [62]. It is not available yet in the `Pixel Console`. This section describes the implementation of it

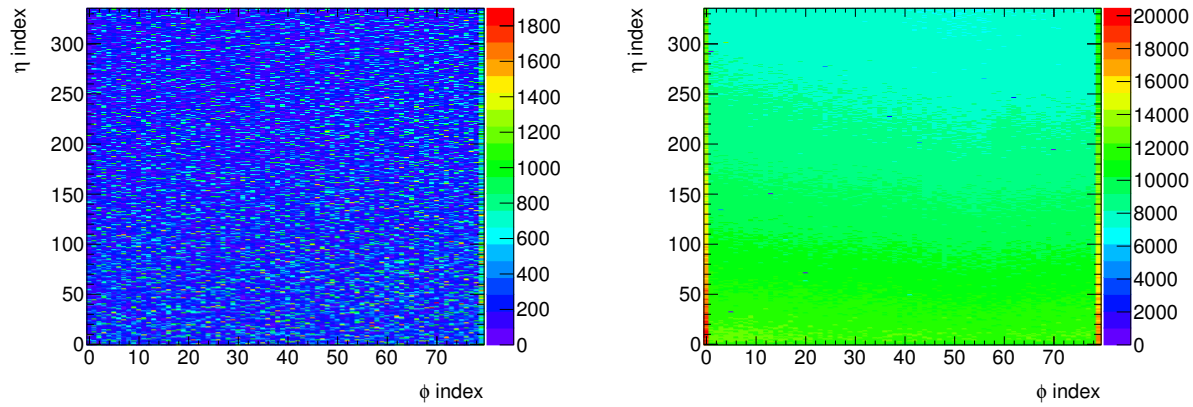

(a) *(b)*

Figure 6.18.: The hits per pixel for run 325713 and module (a) A-M2-6 and (b) C-M1-2. Both were tuned to a threshold of approximately 2500 e.

in the `Pixel Console`.

6.4.1. The Algorithm

To lower the threshold of the FE-I4 to just above the noise floor, the standard tuning techniques are not suitable, as they rely on charge injection. At the noise floor, noise hits become large in number and cannot be distinguished from injected ones. Charge injection based tuning consequently becomes unusable. The LTT makes use of the noise hits close to the noise floor and tunes the FE-I4 accordingly. It relies on the existence of a *Noise Occupancy Scan* (NOS). An NOS triggers the front-end chip for a certain number of times and reports the total number of hits per pixel. As it is not injecting any charge, it measures pure noise contributions to the occupancy, if no source of radiation is apparent. In the FE-I4, the global threshold is defined by two 8-bit registers, `Vthin_AltFine` and `Vthin_AltCoarse` and GDAC := `Vthin_AltCoarse` + 256 × `Vthin_AltFine`. In most applications (such as the DBM), `Vthin_AltCoarse` = 0 and GDAC is used as synonym for `Vthin_AltFine`. The FE-I4 further offers the 5-bit threshold register TDAC per pixel. A lower GDAC means a lower threshold, while this is opposite for the TDAC in the FE-I4. The LTT adjusts the threshold by changing GDAC and TDAC.

A flow chart of the LTT can be found in Figure 6.19. The LTT starts with a high GDAC and a maximum TDAC for all pixels. Then, the inner loop is executed. The inner loop carries out an NOS at first. Pixels with a number of hits above a limit N_h are denoted as noisy and those with a minimum TDAC as disabled. Disabled pixels are not classified as noisy. After the NOS it is checked, whether the number of noisy pixels is

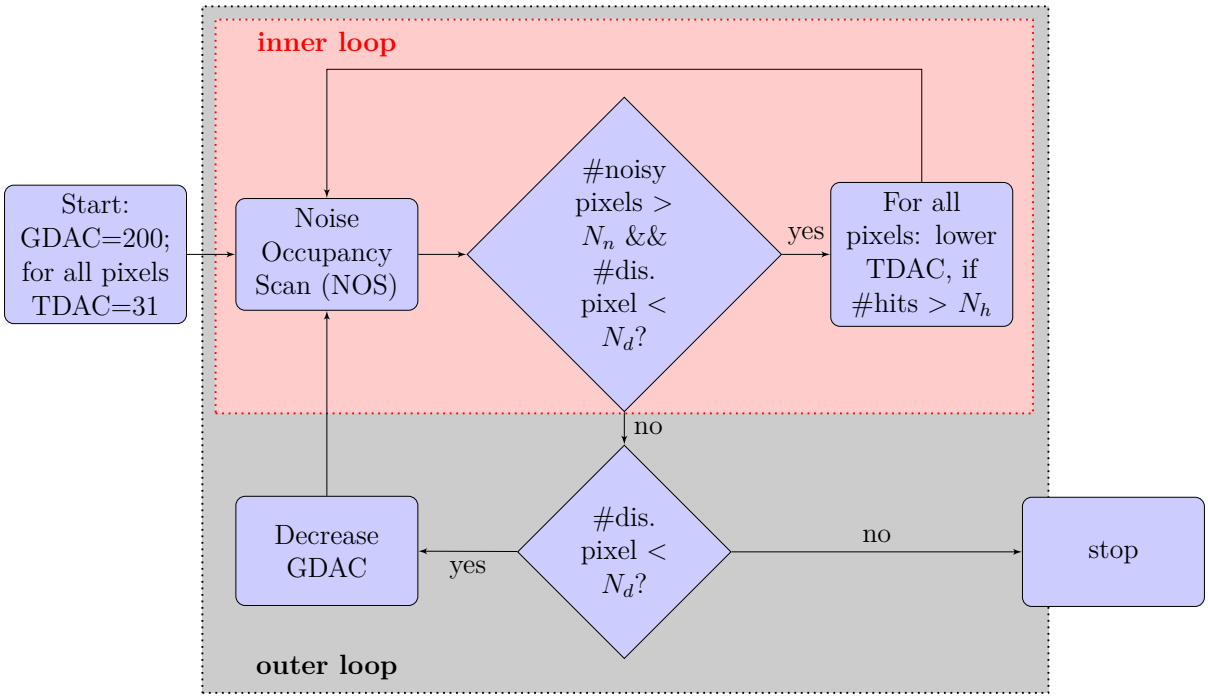

Figure 6.19.: Flow chart of the LTT.

above a certain limit N_n and the number of disabled pixels below a certain N_d. If both are true, the TDAC of all noisy pixels is lowered, increasing the threshold and the inner loop starts again. Else, the inner loop is terminated and the outer loop continues. It checks how many disabled pixels are apparent. If this is below N_d, the GDAC is lowered and the inner loop starts again. Otherwise, the tuning is finished. In the final state, the number of disabled pixels is greater or equal to N_d. Careful choice of N_h, N_n and N_d are required, as they define the tuning point and may cause the algorithm not to converge.

6.4.2. Implementation

The development of the LTT was carried out at the ATLAS Pixel DAQ test environment in SR1.

The NOS

An NOS was not available in the `Pixel Console`. A preliminary version could easily be implemented, by modifying an analogue scan to trigger a module without injecting charge[2]. Since noise is flat both, in time and space, a read-out window of 1 BC and

[2]The "self-trigger" option in the `Pixel Console` yields triggering a front-end without injecting charge.

reading out the entire chip at once was chosen[3]. Since an NOS has to be executed very often during the LTT, it was further optimised, by minimising the time between two triggers.

The time between two triggers is defined by the parameter `m_sleepDelay` in µs in the software. A non-zero `m_sleepDelay` is required, because of bandwidth limitations of the read-out chain. Minimising `m_sleepDelay` was not done before in the calibration framework of the FE-I4. The minimum was found by running analogue scans with 50 injections (= triggers) per pixel for decreasing values of `m_sleepDelay` and checking at which `m_sleepDelay` the number of hits in the scans became lower than the number of injections. At this point the bandwidth limitations are reached and some hits are not transmitted any more. This is shown in Figure 6.20. Stripes with less than the injected 50 hits are visible on the right. The minimum `m_sleepDelay` was found to be 80 µs. Analogue scans with up to 500 injections at this minimum `m_sleepDelay` also finished without lost hits and were taken as proof that the minimum `m_sleepDelay` is independent of the number of triggers.

Finally, an `m_sleepDelay` of 1000 µs was chosen for the NOS. This was done since the execution time was not significantly altered with respect to an `m_sleepDelay` of 80 µs. Furthermore, the corresponding trigger frequency is outside of the FFTV damped frequencies (2 kHz to 40 kHz), considered dangerous in regard of wirebond oscillations. During the process of finding the minimum `m_sleepDelay`, an unused function adding execution time was found in the software. Its removal reduced execution time of an analogue scan with 50 injections by about 30 %.

The functionality of the NOS was tested by varying the GDAC of a module from 100 to 30 and executing an NOS after each step. It was found that the occupancy increases when decreasing the threshold, which was taken as confirmation of proper functioning of the NOS. This is shown in Figure 6.21.

Tests showed that reading out the front-end chip as one, and not in several parts, does not change the occupancies returned by the implemented NOS, as expected. This was achieved by lowering the GDAC of a module to a noisy level and studying the outcome for different scenarios.

A standalone NOS with 10 000 triggers takes around 35 s. It was shown that most of this is due to an initialisation process of a scan in the `Pixel Console`. When running multiple NOS directly after each other without this process in between during the NOS functionality test, the execution time per NOS was less than 15 s.

[3]Typically, the front-end chip is read out in several steps in calibration, because of charge-injection issues.

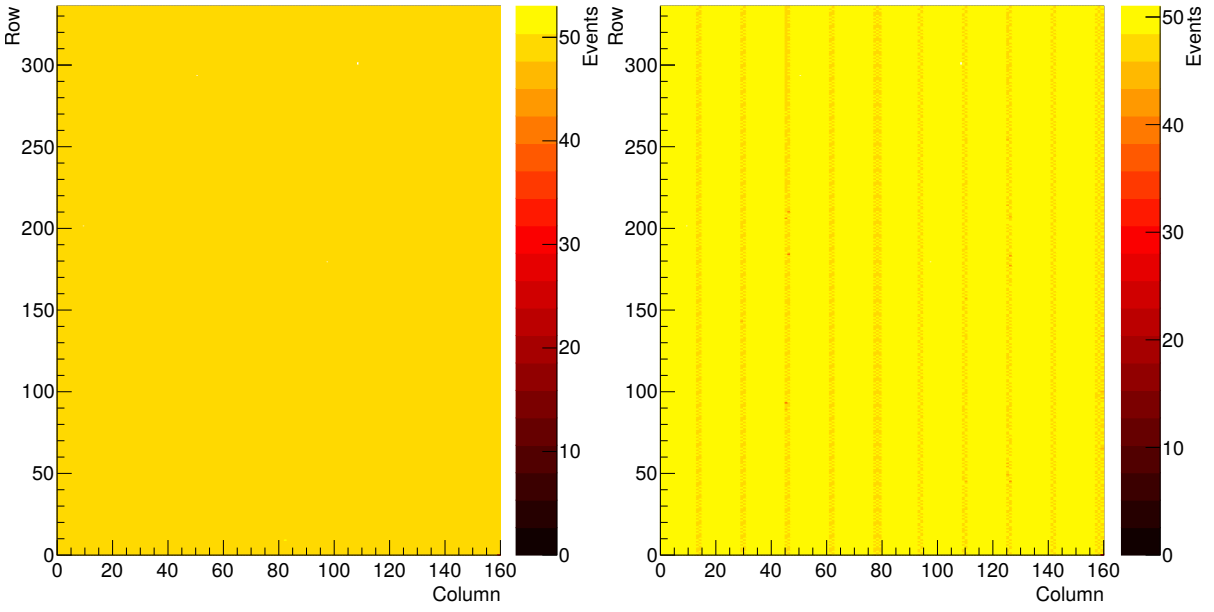

Figure 6.20.: Analogue scans with 50 injections, showing (a) the expected homogenous occupancy pattern with an `m_sleepDelay` of 80 µs and (b) unexpected stripes with fewer hits at an `m_sleepDelay` of 70 µs.

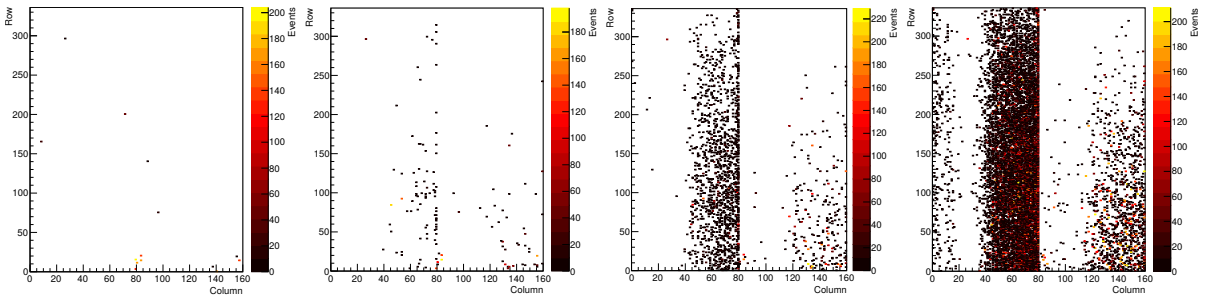

Figure 6.21.: Occupancy measured by an NOS for a GDAC of (a) 80, (b) 70, (c) 67 and (d) 64 for an IBL module in SR1. The increase in occupancy with lowering GDAC can be seen.

Scan ID	Init. GDAC	NOS triggers	`m_sleepDelay` [µs]	N_h / NOS triggers	N_n	N_d	Converged in previous implementation
68648	130	10 000	1000	0.0002	150	10	
68666	130	10 000	1000	0.0001	100	10	For Init. GDAC = 210
68739	130	100 000	100	0.0001	200	10	For Init. GDAC = 210, $N_d = 20$
68761	130	100 000	100	0.0001	50	10	

Table 6.2.: LTT parameters tested for which no convergence was achieved.

The LTT

A previously developed version of the LTT [63] was ported to the `Pixel Console`. After various bugs had been fixed, the number of noisy pixels decreased after each inner loop execution, as expected, and the inner loop was exited on correct condition. GDAC was modified according to the algorithm. However, the tuning never converged, since the required number of disabled pixels was not reached. The maximum number of disabled pixels observed was five, which was less than all tested values of N_d. The combinations of N_h, N_n and N_d shown in Table 6.2 were tried for the latest version of the LTT. The `Pixel Console` SR1 scan ID, the number of triggers executed by each NOS, the `m_sleepDelay` value for the NOS and the starting GDAC are also given. The trials with `m_sleepDelay` = 100 µs were done to reduce the NOS execution time with 100 000 triggers. The Noise Occupancy Scans might have reached the bandwidth capacities in these cases, though, which should be studied further, if their use is desired. Some settings in Table 6.2 led to convergence in a previous implementation of the LTT. Concluding, the entire implementation of the LTT, from the NOS to the parameter choice, has to be revised in the future. Some technical details on the LTT implementation can be found in Appendix A.3.

7. Wirebond fusing and oscillation tests

To find the maximum operation current height of the DBM, wirebond fusing tests with a specially designed board, the *Wirebond Test Facility* (WTF) board, were done. Furthermore, wirebond oscillations were reproduced, to gain a deeper understanding of how modules stopped communicating in the DBM.

7.1. Wirebond fusing

Wirebond fusing describes the process when a wirebond becomes hot, melts, and is split into two, because of a current that is too high. In [64] it is shown that the current I_f, at which fusing is reached, depends on the wire cross-section A and its length L. In the model presented therein, the wirebond is described to melt when the heat supply by the current equals the heat loss by heat conduction along the wire. The authors neglect heat loss by convection of the surrounding air and radiation, which they assume to be dominated by conduction losses. Further assumptions are that both wirebond ends are at ambient temperature (298 K) by the pads on which they are installed, which act as perfect heat sinks, and that fusing appears at the middle of the wirebond. They then perturbatively solve a steady state heat equation, incorporating a second order non-linear approach for the resistance as a function of the temperature and find

$$I_f = \frac{A}{L} M. \tag{7.1}$$

Here, M is a constant that describes the heat propagation along the wire, which is $M = 3.489 \times 10^4\,\mathrm{A\,cm^{-1}}$ for Aluminium. For the wirebonds used in the experiments described below, which were of 25 µm thickness and about 4 mm length, the formula results in a fusing current of $I_f = 428\,\mathrm{mA}$.

7.2. The Wirebond Test Facility (WTF) board

The WTF board is a custom-built PCB, dedicated to wirebond tests. A picture of the board can be found in Figure 7.1a. The WTF board accommodates up to 256 wirebonds, sorted into a 16×16 matrix. A power supply can be connected to the board to source a current through individual wirebonds. The rows and columns are connected via transistors to the respective poles of the power supply. The transistors act as switches and are steered by shift registers. For a gate-source voltage of below 1 V to 2 V, the transistors behave like diodes, but become conductive in both directions for higher voltages. LEDs indicate which transistors are open. The shift registers are powered by an external power supply and are controlled by an `Arduino`, which is steered by a set of `Python` scripts. The wirebonds are installed on pads of 0.9 mm width and a spatial separation of 2 mm on the board. The pads on one side of a row are connected to each other, as can be seen in Figure 7.1a. One end of a wirebond is installed on one of these "row-pads" and the other end of a wirebond is attached to the opposite "single-pad", visible in Figure 7.1a, too. Due to the design of the board, a maximum of 31 wirebonds can be attached simultaneously and addressed one by one. The installation of the maximum number also requires a specific order of the wirebonds, preventing 2×2 "nets": if there are two rows in which two wirebonds are attached at the same column, then there will be unexpected current paths in parallel to the wirebond under study, as shown in Figure 7.1b. These reduce the current through the considered wirebond with respect to the intended current. The wirebonds that were installed were made of Aluminium and had a thickness of 25 µm, as for the DBM wirebonds. Their length was about 3–5 mm.

7.3. Wirebond fusing investigations

The wirebond fusing current was investigated in two kinds of tests. In stability tests, the current sourced through a wirebond was increased from 100 mA to 1000 mA in steps of 10 mA without switching the output of the power supply off when changing the current. One current was kept for 11 s. Aim of the stability tests was to find the wirebond fusing current. In endurance tests, a certain current was sourced through a wirebond for a certain period of time. The endurance tests were made to study whether the wirebonds fused at a lower current as well, when being subject to it for a longer time. During both tests, a `GPIB` controlled power supply "Keithley 2410" was used for current sourcing and voltage and current were monitored with this device. Both type of tests were automated, continuing with the next wirebond, if one had fused (identified by no current flowing

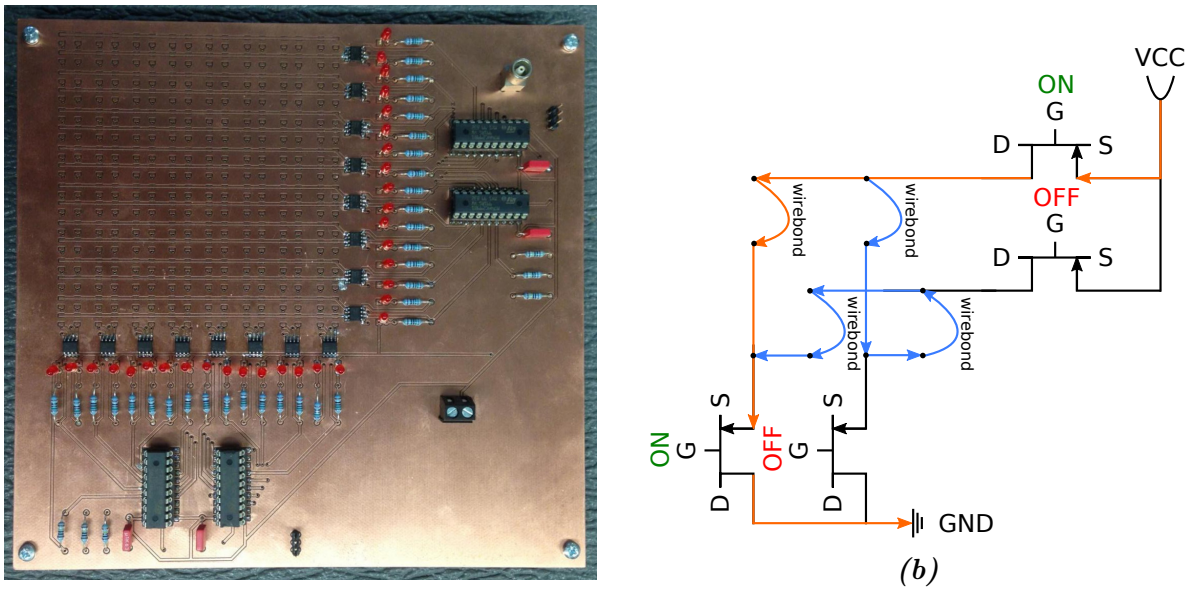

(a) *(b)*

Figure 7.1.: (a) The WTF board. (b) The current loop occurring in a 2×2 matrix of wirebonds, reducing the current flow through the single wirebond addressed.

through a wirebond any more).

7.3.1. Stability tests

For the stability tests, 15 wirebonds were used and the currents at which they fused is shown in a histogram in Figure 7.2a. All wires fused immediately after this value had been set. The average fusing current was found to be $\widetilde{I}_f = (711 \pm 8)\,\mathrm{mA}$. Because of the characteristics of the transistors used and the design of the WTF board, the current measured by the power supply and the current flowing through the wirebond under test might be different, if there is more than one wirebond installed in one row. Because the wirebonds tested here broke successively and were installed in one row only, this kind of effect should be visible in an increase of resistance of the WTF board. Within the given statistics, this was not observed.

A broken wirebond directly after the fusing is shown in Figure 7.2b. For many wirebonds, the mechanical breaking point was difficult, or not possible, to see. That they were broken could be told by their infinite resistance and the wirebonds glowing before breaking. To enhance the visibility of the breaking points, all wirebonds were poked with a pair of tweezers. All wirebonds were torn on the side of higher gradient, which was located on single-pads; six of them very close to the foot and the remaining ones well

above the foot at around 30 % of its length, as shown in Figure 7.3. This observation is not in accordance with the one by [64] (see [65] for details on the measurement procedure). They observed that the wirebonds broke roughly in the middle. The wirebond breaking in the middle was assumed in the theoretical calculation and the ratio of the experimental and upper theoretical fusing current is $\frac{\widetilde{I}_f}{I_f} = 1.66$. That the breaking point is shifted with respect to other experiments and the theoretical prediction might be due to the different sizes of the surfaces on which the wirebonds were installed. All wirebonds fused closer towards their single-pads. The single-pads have a much smaller surface than the row-pads. The hypothesis is therefore that less heat can be carried away via the single-pads, making the wire melt closer towards them. This reasoning is supported by the observation that the wirebonds, shortly before fusing, started glowing entirely and that the part of the wirebonds that stopped glowing at last, was at the single-pads, i.e. the heat dissipation towards the single-pads is least. The glowing behaviour is shown in Figure 7.4. The hypothesis would mean that one wirebond foot has a different temperature than the other. Equation (7.1), based on the assumption that both feet are at ambient temperature, would not be applicable any more.

The comparability of the found fusing current to the fusion current for the wirebonds in ATLAS must be questioned, since the pad sizes and corresponding heat sinks in this experiment were larger, increasing the fusing point. Furthermore, the air-circulation around the wirebonds in this experiment was larger than in the DBM, i.e. there was more cooling by convection. Conversely, the ATLAS wirebonds are shorter than the ones used here [66], leading to a potentially higher fusing current, because the heat can be transported away from the wire more quickly. The impact of these factors should be studied separately.

7.3.2. Endurance tests

In the endurance tests, 16 wirebonds were exposed to 600 mA successively for 4 h. Since none of the wirebonds broke, the same scenario was repeated for the same wirebonds with a current of 700 mA. One wirebond was found to break immediately after the 700 mA were applied. For the other wirebonds, no fusing, but a change of the material was seen. The surface of the wirebonds was not as shiny as before, showing significant corrosion, and the wirebonds were deformed. The resistance of the wirebonds was measured with a multimeter via the installation pads after the endurance tests. For the 15 intact wires, an average resistance of $(0.91 \pm 0.06)\,\Omega$ was found. This is more than double of the typical resistance of about $0.3\,\Omega$ to $0.4\,\Omega$. In pull tests, some of the current exposed wirebonds were seen to tear along the wire. Wirebonds not exposed to any current always broke

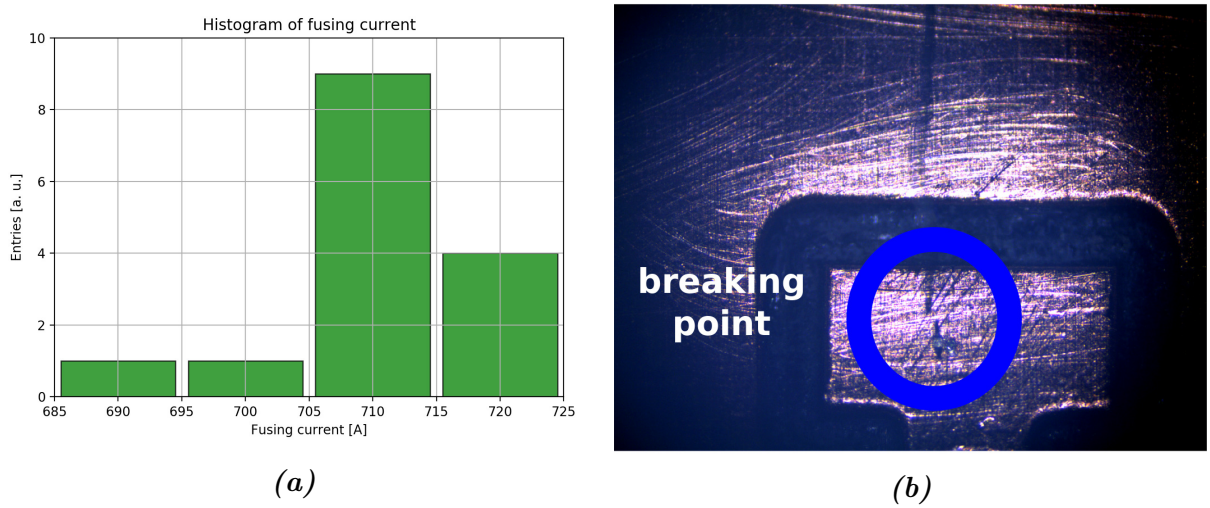

Figure 7.2.: (a) Histogram of the fusing currents found during the stability tests of 15 wirebonds. (b) A broken wirebond after fusing.

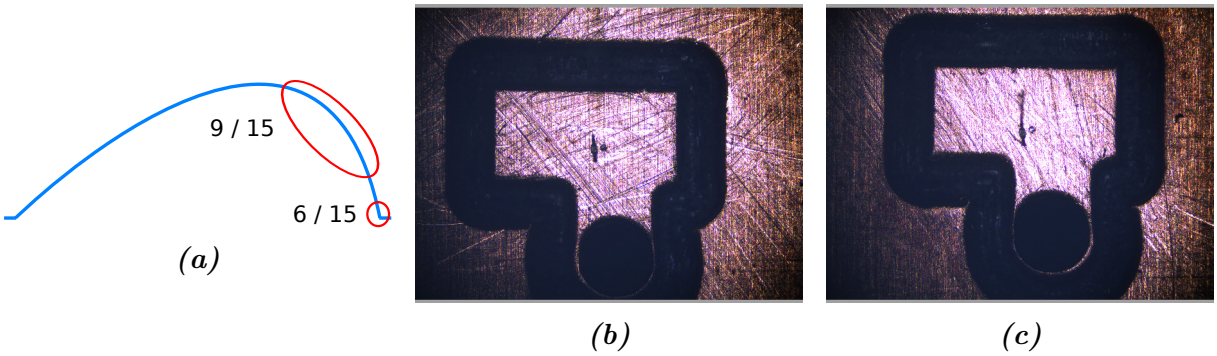

Figure 7.3.: (a) The points at which wirebonds fused. Characteristic microscope pictures of fused wirebonds are shown in (b) at the foot and (c) above the foot, after being poked with a pair of tweezers.

at one of the feet. This indicates that the wire material was weakened in the endurance tests. No glowing of the non-fused wirebonds was observed. The endurance tests showed that four hours at 700 mA do not necessarily break the wirebonds, but do deform them and change their form, surface, resistance and pull strength.

7.3.3. Pulsed power tests

To test a more realistic scenario for the wirebonds in ATLAS, a function generator was connected to the constant current power supply. Current pulses occur from triggering during data-taking and this situation was mimicked for one wirebond. The function generator was AC coupled to the power supply, as shown in the circuit diagram in Figure 7.5. An oscilloscope was connected right at the wirebond, to monitor the signal. A current

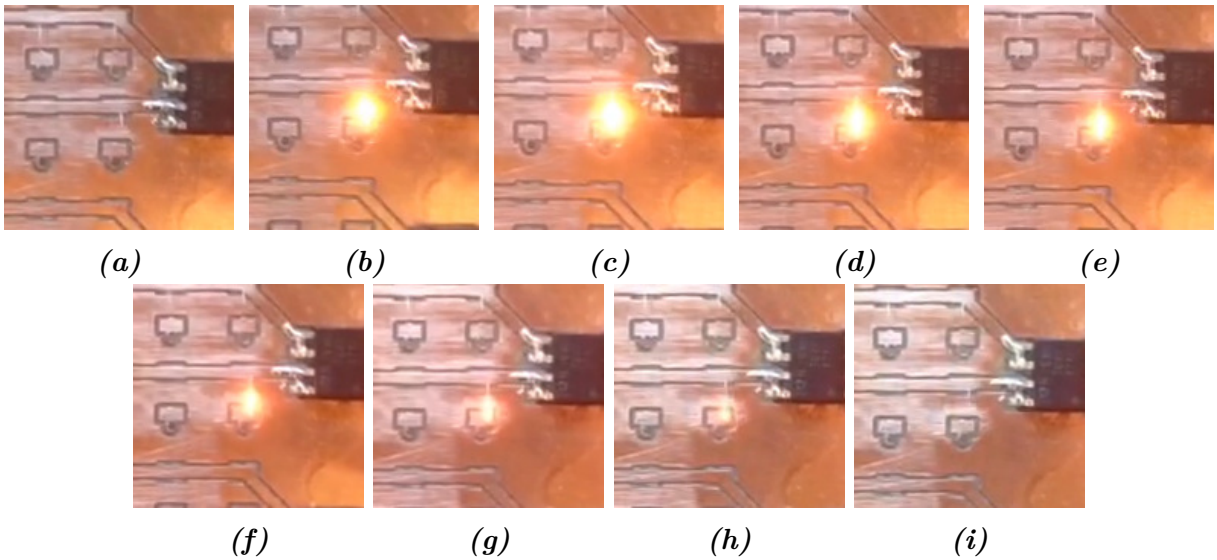

Figure 7.4.: (a) The current is not high enough for fusing, yet. (b) The fusing current is reached, the wirebond starts glowing. (c) The glowing continues for about 4 s, then (d)–(h) decreases towards the pad within 3 s and (i) stops glowing.

of 700 mA was sourced by the power supply. The function generator was set to output pulses of 500 mV amplitude, at a duty cycle of 99 %. The frequency was set to different values between 1 kHz and 40 MHz. The current added by the function generator was about 60 mA at its peak, resulting in a total current of about 760 mA. The wire did not fuse. Since all previously tested wirebonds had fused at this current value, it can be deduced that the time a certain current is sourced is of importance. Taking the lowest frequency of 1 kHz and a duty cycle of 99 %, the current was applied for a maximum of about 1 ms here, not taking into account that actually the derivative of the pulse signal is seen by the wirebond, because of the AC coupling, reducing the time even further. This time does not seem sufficient to break the wirebond.

Another wirebond was left at a current of 700 mA plus 60 mA pulses with a frequency of 50 kHz and 99 % duty cycle for some hours, to study exhaustion breaking. This was not observed.

7.4. Wirebond oscillation tests

Destructive wirebond oscillation tests were carried out with the WTF board, complementing studies conducted for the IBL [66], to study the hypothesis of wirebonds oscillations causing non-communicating DBM modules. An electro magnet was used to generate a magnetic field of 450 mT. The wirebonds were exposed to the magnetic field in the same

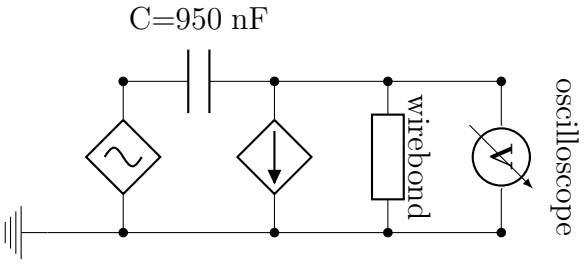

Figure 7.5.: The circuit diagram of the pulse generator connected to the constant current source, which itself is connected to the wirebond and an oscilloscope.

way as they are in the DBM. To observe movements of the wirebonds, a microscope was placed on top of the WTF board. A function generator was directly connected to the WTF board and configured to output an alternating square signal of 2.5 V peak amplitude at 50 % duty cycle. Due to the characteristics of the transistors and the design of the WTF board, the exact corresponding current peak amplitude cannot be given, but measurements indicate that it was somewhat less than 100 mA for the wirebond under test. In any case the current was way above the maximum signal current flowing through the clock-, command- and data-wirebonds at the front-end chips, which is at most 3 mA [67]. Two photographs of the setup can be found in Figure 7.6. Wirebonds were installed in several batches in different rows, to prevent row or re-bonding dependent systematics. For each wirebond, the frequency of the alternating square signal was adjusted by hand. It could be visually confirmed that the wirebonds oscillated in the magnetic field, if an alternating signal was applied.

A sweep and an endurance test program were run. In the sweep test program, the frequency of the function generator was changed, without turning the function generator output off between two frequencies. Taking all sweep tests together, the spectrum from 1 Hz to 50 kHz was covered. The tests showed that there are many frequencies at which a wirebond began resonating in the magnetic field. A list of destructive frequencies is given in Table 7.1. Only results from tests where the frequency was changed upwards or downwards but not a combination of the two, and immediate breaks when turning on the current pulses, are shown. Most wirebonds broke at a frequency of 9 kHz and neighbouring frequencies were also prominently destructive. A frequency of 3 kHz and neighbouring also caused many wirebonds to break. The function generator produced an alternating square signal $I(t)$ with peak amplitude I_0 and frequency ω, which can be Fourier decomposed into:

$$I(t) = \frac{4I_0}{\pi}\left(\sum_{k=0}^{\infty}\frac{1}{2k+1}\sin((2k+1)\omega t)\right) = \frac{4I_0}{\pi}\left(\sin(\omega t) + \frac{1}{3}\sin(3\omega t) + \frac{1}{5}\sin(5\omega t) + \ldots\right).$$

Thus, it seems reasonable, that the resonance frequency ω_0 of the first normal mode of the wirebonds is located around $\omega_0 = 9\,\text{kHz}$. The first normal mode resonance frequency can be calculated by

$$\omega_0 = \frac{kd}{l^2}$$

with k a constant depending on the wirebond properties, d its diameter and l its length. Since the lengths of the wirebonds differ, a spread of the resonance frequency, as observed, is plausible. For higher frequencies than 15 kHz, no strong wirebond oscillations were observed. That certain frequencies were destructive for some wirebonds, but not for others, may also be because the time interval a frequency was applied was irregular, due to the manual frequency change, causing sufficient time for destruction in some cases, but not in others. All wirebonds suffered heel breaks at one of the feet. From the 40 wirebonds tested, of which half had their first foot on the single-pad, 36 broke at the row-pads. The remaining wirebonds broke at the single-pads and all of them had their first foot on the single-pads.

Endurance tests of one wirebond running at frequencies between 10 kHz and 20 kHz and durations of at least 4 min, see Table 7.2, were not destructive. The output of the function generator was turned off when changing frequency. At a frequency of 9 kHz, the wirebond stopped resonating after about 5 s, but no mechanical damage was observed. The resistance directly after this incidence was measured in the order of MΩ, in comparison to the typical resistance of 0.4 Ω. Some hours later, the resistance was in the order of kΩ, and a day later the resistance was just 56 Ω. It seems like some sort of damage happened through the wirebond oscillations and annealed with time. More statistics could not be gained due to time constrains.

In past wirebond oscillation tests conducted by the DBM collaboration at CERN, no breaking wirebonds were found. That wirebonds were seen to break here, might be related to current pulses of larger amplitude being used.

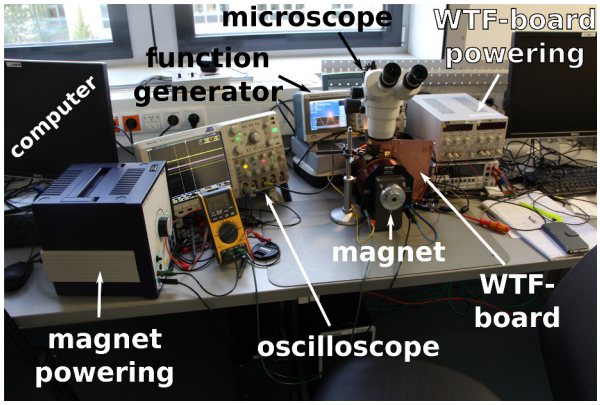

(a)

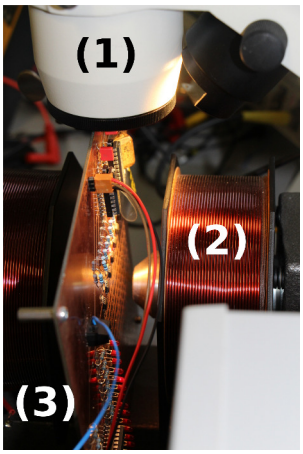

(b)

Figure 7.6.: (a) Overview of the experiment setup for the wirebond oscillation tests. (b) Close-up of (1) the microscope, (2) the magnet and (3) the WTF-board.

Frequency [Hz]	Wirebonds tested at this frequency	Broken wirebonds
1000	17	2
2000	15	3
3000	13	4
7000	9	2
9000	11	8
10000	9	3
11000	10	2
12000	11	1
13000	10	1
15000	9	1

Table 7.1.: Destructive current oscillation frequencies. The second column gives the number of wirebonds for which the exact frequency was scanned and the third column gives the number of wirebonds that broke.

Frequency [kHz]	Duration [min]
20	~ 8
15	~ 4
13	~ 8
11	> 30
10	~ 4

Table 7.2.: Amount of time one wirebond was exposed to certain frequencies without breaking.

8. Summary and outlook

The recommissioning of the DBM was the main part of this thesis. After a recommissioning period of six months all but one module in SR1 are configurable and return the expected idle signal. Because of unmatched impedances these signals are distorted and only one module consistently shows an idle signal at the BOC. Thus, one module can be operated reliably in SR1. As this was sufficient for the time being, it was decided to leave the DBM SR1 setup in this state in favour of the recommissioning effort at IP1.

The DBM in Atlas was recommissioned in 2017 with 12/24 communicating modules. Several issues were addressed when doing so. Before the EYTS in December 2017, the DBM was operating stably with one Silicon module and one complete diamond telescope. Further modules had been enabled during the year, but were disabled for various reasons. The main concern during operations was an increase of the module current consumption due to ionising radiation damage.

To increase the efficiency of the diamond modules, a special tuning procedure, calibrating the threshold of the front-end chip to just above the noise floor was implemented. A Noise Occupancy Scan was required to do so and was developed and optimised. Despite multiple efforts, no converging version of the tuning procedure could be realised. Revision of all involved steps and parameters is necessary.

In wirebond fusing tests, the average fusing current of 15 wirebonds was found to be $(711 \pm 8)\,\mathrm{mA}$. Whether the fusing current result is comparable to the DBM in Atlas was discussed. While the smaller pad sizes and less convection in Atlas would lower the fusing current with respect to the measurements presented here, the shorter length would increase it.

Further tests concerning the long-term stability of wirebonds with respect to a high current showed that 4 h at 600 mA were not destructive for the wirebonds used. When applying 700 mA for 4 h to the same wirebonds, one out of 16 broke immediately. After the long term tests form, surface, resistance and pull-test behaviour of the intact wirebonds had changed.

In pulsed power tests, applying a current of 700 mA plus pulses of about 60 mA height at frequencies between 1 kHz and 40 MHz, no wirebond was seen to break. Considering the

fusing current, this might have been possible. The fact that no destruction was observed, was accounted to the current being applied for a too short time to cause damage.

Wirebond oscillations could be reproduced. The first normal mode resonance frequency was found to be around 9 kHz.

8.1. Outlook

A future functionality test for the non-communicating modules in ATLAS is: first, configuration of the communicating modules of a telescope with the `Pixel Console`, then, configuration of the entire telescope with the Channel-Mapping tool and finally, configuration of the communicating modules with the `Pixel Console` again. The low-voltage current after the first and last step shall be compared. If it is the same, then the Channel-Mapping tool only manages to configure the communicating modules. The Channel-Mapping tool was able to configure all of the modules during initial commissioning and has not been modified since. Therefore, it seems unlikely that communication with modules which are not configured by the Channel-Mapping tool, could be re-established. If the current consumption between the first and the last step does change, there might be a way to make the non-communicating modules responsive again, as they would receive commands. The problem would then be in the data-return chain.

After a ROD firmware change to solve the de-synchronisation errors during operations and setting the read-out window to 1 BC, some of the DQ error histograms were not filled any more. This impeded debugging. When operating more than one module per side some of the histograms showed entries again, but whether they are filled correctly is not understood yet. Investigation with `Chipscope` could reveal whether the histograms are filled correctly and what the reason for any of the reported errors, including the de-synchronisation errors, might be.

From the beginning of September until November 2017, calibration of modules was not possible for the DBM, as all scan result histograms in the `Pixel Console` were empty. The modules added to data-taking after the 31st of August could therefore not be tuned. Tuning should be carried out during the EYTS 2017.

To follow up whether the current drops of about 70 mA on telescope C-M1 influence the data-taking of the operated module C-M1-2, correlation of occupancy and these drops should be studied for an entire run.

For 2018, tracking with the DBM telescopes is planned, which requires a timing scan of all involved modules. Furthermore, the de-synchronisation errors should be solved to ensure correct association of hits.

To potentially solve the micro-busies, automatic reconfiguration of the DBM modules at the ECR will be installed. For full integration into the Pixel DAQ, *Quick Status* (QS) will be implemented for the DBM, which allows for individual module reconfiguration during a run. To allow for luminosity measurements, a dedicated DBM BOC firmware has been prepared. Installation of the automatic reconfiguration, QS and the DBM BOC firmware are scheduled for the ongoing EYTS.

By investigating the fusing current of wirebonds, in short-term, long-term and pulsed tests, with pads, wirebond lengths and convection scenarios comparable to the DBM in ATLAS, more accurate operation guidelines concerning the current consumption of a telescope could be reached. This could also reveal, how likely wirebond fusing in the context of modules stopping to communicate is.

To test the hypothesis that wirebond oscillations make modules non-communicating further, oscillation tests with a high constant current plus pulses could be done. Studying oscillations as a function of the current pulses' height (in particular for small current pulses) could show at which threshold the wirebonds can be destroyed. With random pulses, the situation when first modules were seen to stop communicating could be reproduced.

A. Appendix

A.1. Documentation of the DBM

Documentation of the DBM concerning technical drawings can be found on the EMDS (`https://edms.cern.ch/`), by searching for "DBM". In general there is documentation of the DBM on the DBM TWiki page, `https://twiki.cern.ch/twiki/bin/view/Atlas/DbmWiki`. The TWiki contains specific pages for technical drawings, for powering and DAQ handling in SR1 and in ATLAS. When working on the SR1 setup very helpful technical drawings were the documents `ATL-IP-ES-0189` and `ATU-SYS-ES-0025_DBM`, containing the type-I cable routing and PP0 to opto-board connectivity, and the type-II cable routing, respectively. It thereby has to taken into account, that the drawing of the PP1 plug might have to be mirrored with respect to the documentation, as a female plug is shown there. Also, the plug at the opto-board does not have the pin numbers 17 and 55, which led to confusion. In `ATU-SYS-ES-0025_DBM` the counting of the pins of the two Axon connectors is reverted in the connectivity table with respect to the drawing which explains it (from right to left, instead of from left to right).

Further documentation can be found in the sharepoint, `https://espace.cern.ch/ATLAS-DBM/`. William Trischuk can provide access to this webpage. There exists a table in the sharepoint ("Modules" → "Module_serial_numbers_mc.xls"), which lists some useful QA results from the DBM modules (for example serial numbers, GodIDs).

The section "New to DBM" on the DBM TWiki, `https://twiki.cern.ch/twiki/bin/view/Atlas/DbmNewUser`, provides valuable information for new DBM members.

A.2. Notes concerning SR1

A modification of the Channel-Mapping tool in SR1 exists, in which the GeoID that is supposed to be used for all Tx/Rx-combinations can be customised. Contact the author to obtain it.

A picture of PP1 in SR1 can be found in Figure A.1a, of the PP0 pads in Figure A.1b, and of the PP1 pins, of which one is damaged, in Figure A.1c. Unconnected wires at the

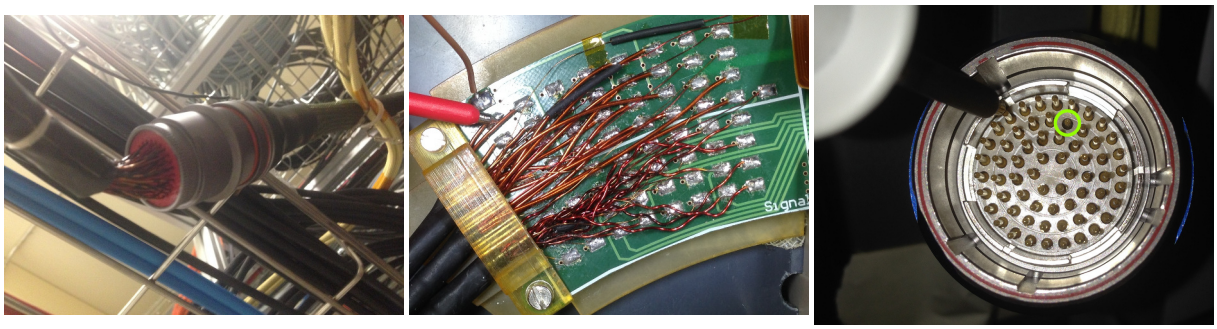

(a) *(b)* *(c)*

Figure A.1.: (a) PP1 of the DBM test setup in SR1. (b) The solder pads on PP0. (c) The pins of the connector of the type 1 cable. Marked in green is a pin that was found damaged.

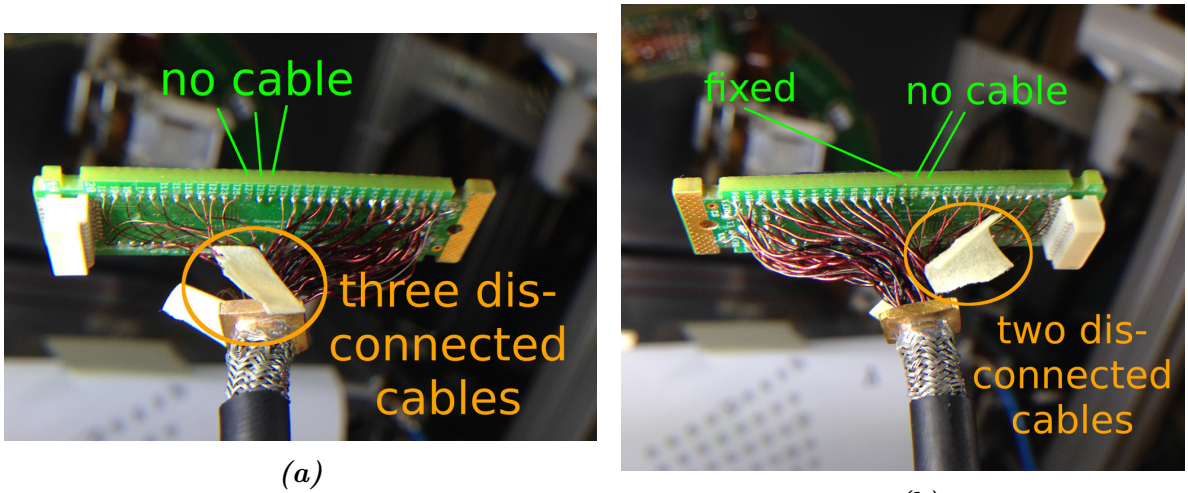

(a) *(b)*

Figure A.2.: Both sides of the opto-board connector.

opto-board can be seen in Figure A.2. One of the pins at the opto-board could be fixed easily, but the remaining ones were very difficult to repair, which is why it was decided to replace PP0 altogether.

The routing of the new cable in SR1 can be found here: `https://twiki.cern.ch/twiki/pub/Atlas/SatelliteRoom1/CableSr1.pdf`. With the new cable high voltage was never tested and is probably only available up to a maximum of 50 V. Boštjan Maček can provide further information if needed.

The setup during the USBPix system tests is shown in Figure A.3. The table of results can be found in Table A.1, together with further connectivity and module informations.

Figure A.4 shows the results from the oscilloscope tests concerning the clock- and command-lines when sending a configuration with the Channel-Mapping tool.

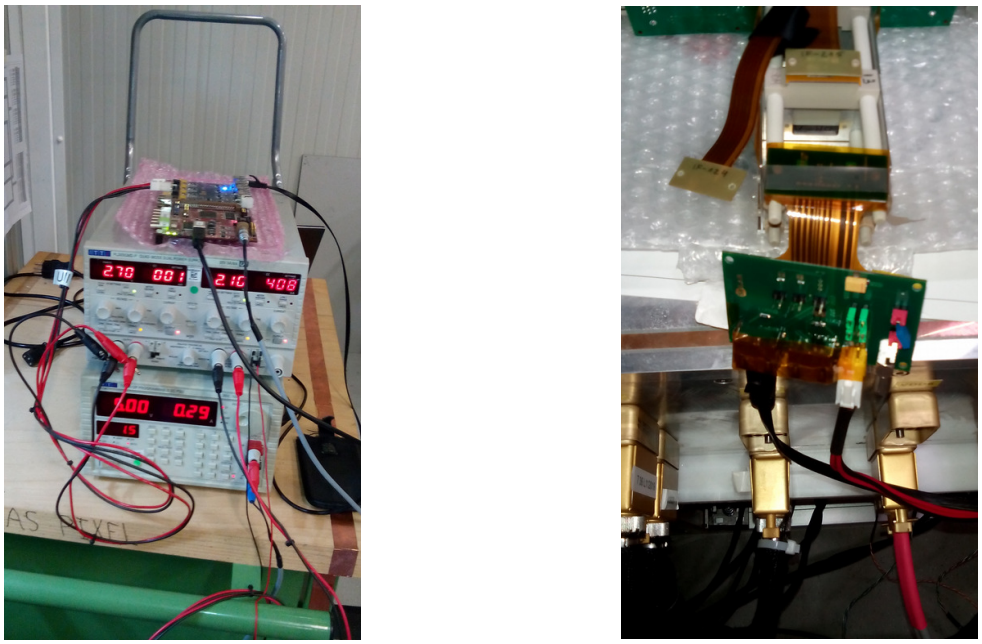

(a) *(b)*

Figure A.3.: (a) The USBPix board with power supplies. (b) Connection of the USBPix board to a module in SR1 using an adapter flex.

Name	Telescope	Layer	Sensor	S/N	GeoID	Tx	Rx	I_u [mA]	I_c [mA]	digital	analog	threshold	tuning
MSBM-25	M3	2	Si	972	7	7	11	273	415	OK	OK	OK	OK
MSBM-13	M3	1	Si	969	4	6	10	277	387	OK	OK	OK	OK
MSBM-28	M3	0	Si	982	6	5	9	400	400	OK	OK	OK	failed
MDBM-104	M4	0	C	1688	1	7	15	300	402	OK	OK	OK	OK
MDBM-13	M4	1	C	-	-	6	14	348	-	failed	failed	failed	failed
MDBM-101	M4	2	C	1686	3	5	13	290	420	OK	OK	OK	OK

Table A.1.: The modules in SR1, their location, sensor, connectivity and results of the USBPix system test. I_u denotes the unconfigured and I_c the configured current consumption.

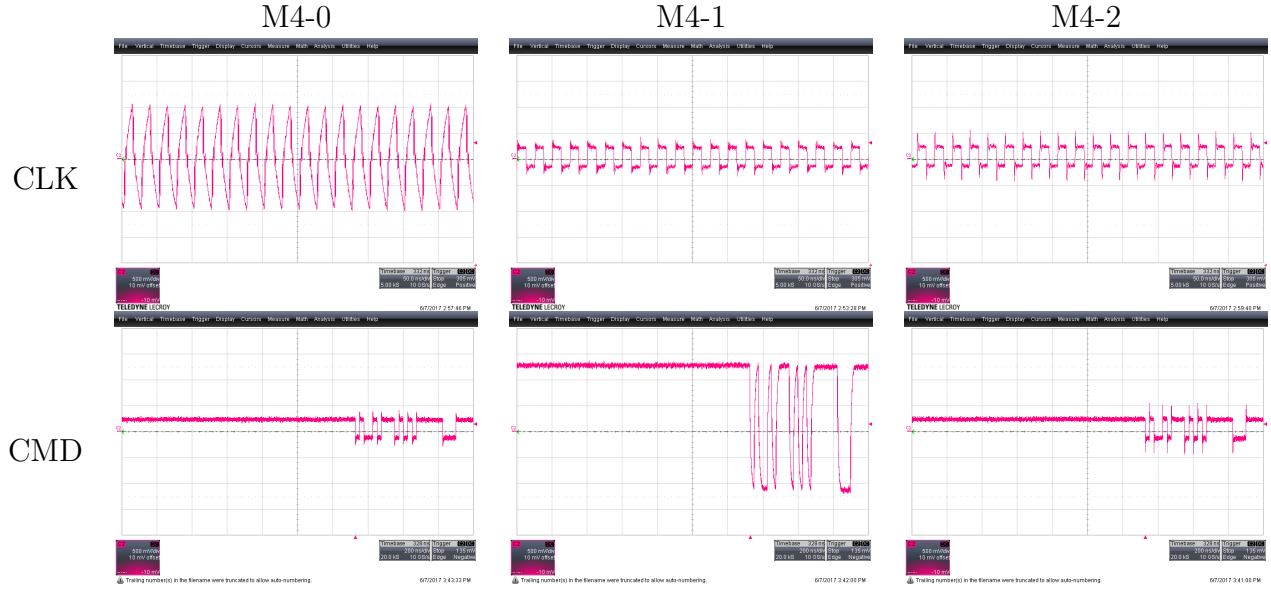

Figure A.4.: The clock- (CLK; above) and command-line (CMD; below) signal measured on PP0 during a configuration for the modules of telescope M4 in SR1. The y-axes are equal for all plots; the x-axes are the same in each row.

Four example cases of the output of `Chipscope` are shown in Figures A.5, A.6, A.7 and A.8, when trying to communicate with modules after installing the square board setup in SR1. The idle pattern can be identified by a "3C" signal in `dec_dout`.

It was mentioned in Section 5.4 that the opto-board outputs random patterns when the BOC laser is turned off. This was reproduced with the DBM setup in SR1. The opto-board was turned on and one clock- and command-line were monitored. Depending on the BOC laser, the results shown in Figure A.9 were found. The width of one time bin is 50 ns for the BOC laser on and 200 ns for the BOC laser off. Furthermore, the polarity of the differential probe is opposite for the BOC laser on and off. As can be seen, clock and command-line output random information when the BOC laser is off.

The DBM setup in SR1 did not posses a ROD until 2017. This was not needed, as all wanted tests and further development steps could be carried out without a ROD until then. Because of changed requirements, a ROD was installed on the 22nd of February 2017. The placement of the DBM BOC and ROD in SR1 are pointed out in Figure A.10. Together with the Pixel/IBL experts, the DBM ROD was included into the Pixel/IBL DAQ in SR1 in late November 2017. Before scans can be carried out though, some minor code modifications have to be done. Also, no local data taking is available, yet.

Archiving of the low-voltage current is available in the FSM in SR1 since mid-2017.

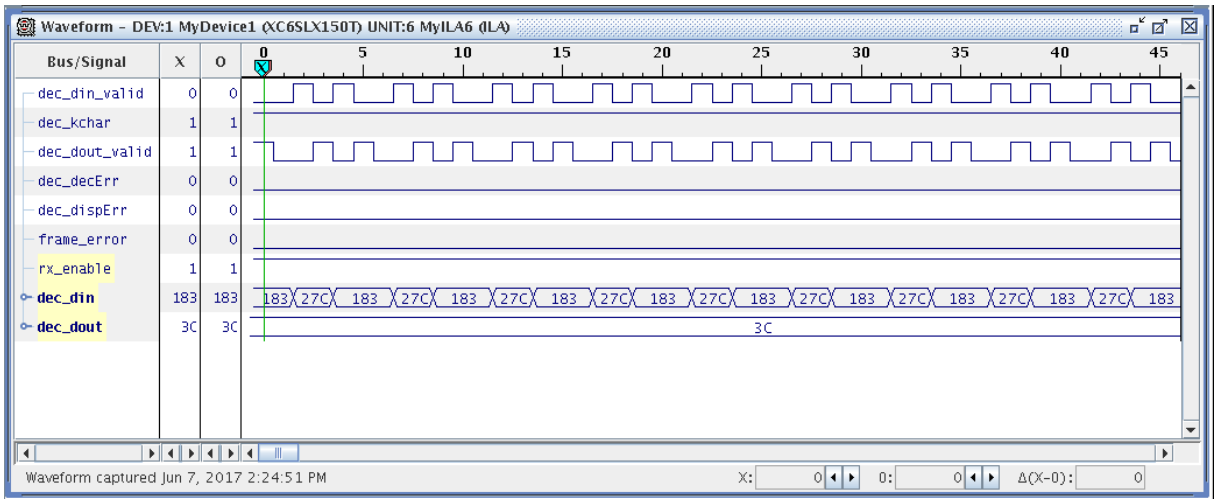

Figure A.5.: A `Chipscope` output showing the idle pattern.

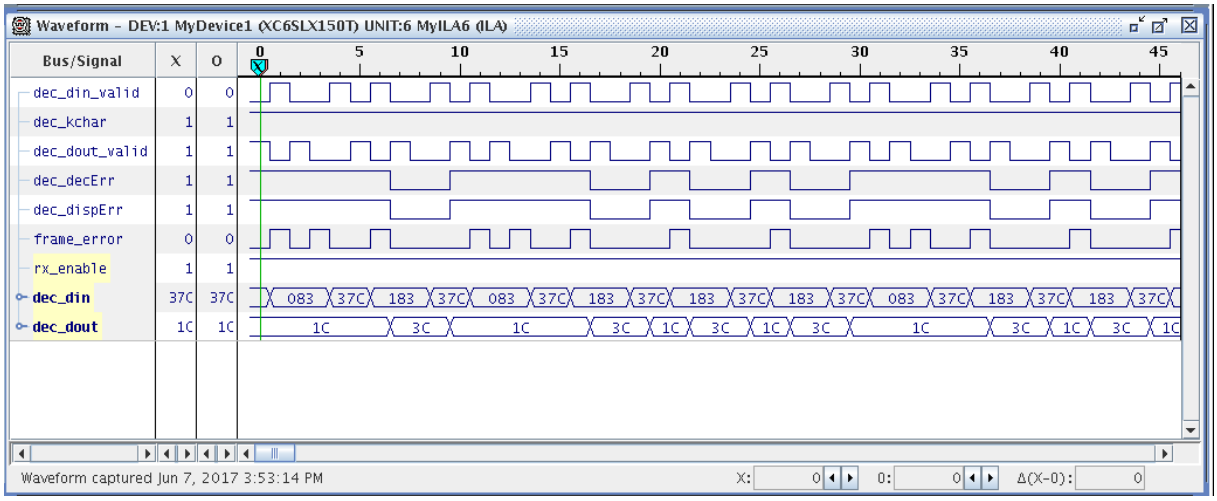

Figure A.6.: A `Chipscope` output showing a distorted idle pattern with sporadic bit flips.

A.3. Notes concerning the IP1 setup

Powering

The FSM allows for *alerts* and *states*. While states give quite specific status information (for example "the telescope is configured with preamps off"), the alerts give more general information and indicate potentially dangerous situations for the DBM. Alerts are defined purely via limits on the object they concern, for example on the current consumption or the temperature of a telescope. States can combine information from different objects and contain limits as well.

For all objects except the telescopes, the FSM states are `OFF` and `READY`. For the tele-

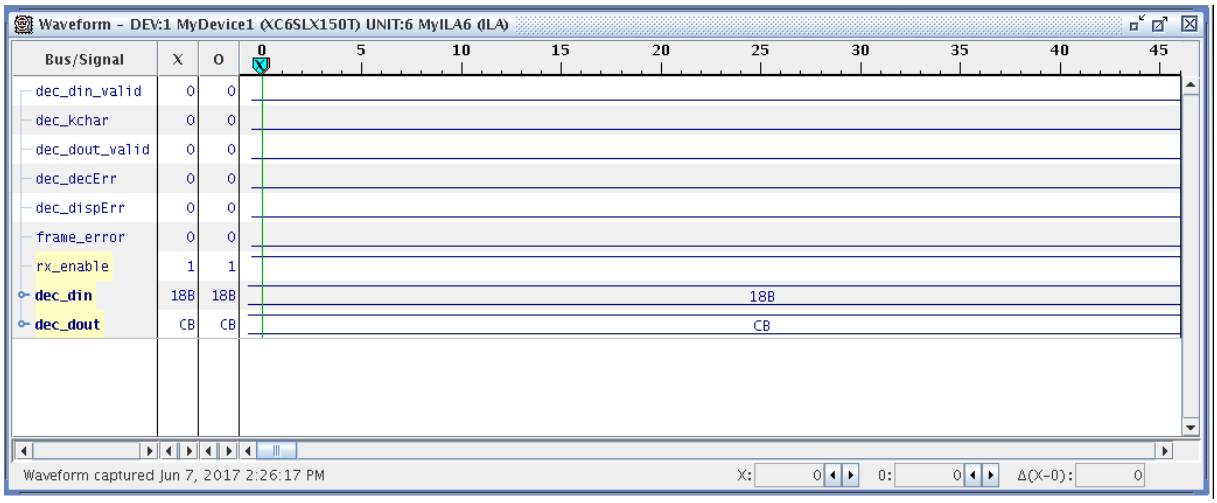

Figure A.7.: A `Chipscope` output showing a distorted idle pattern with a continuous bit flip.

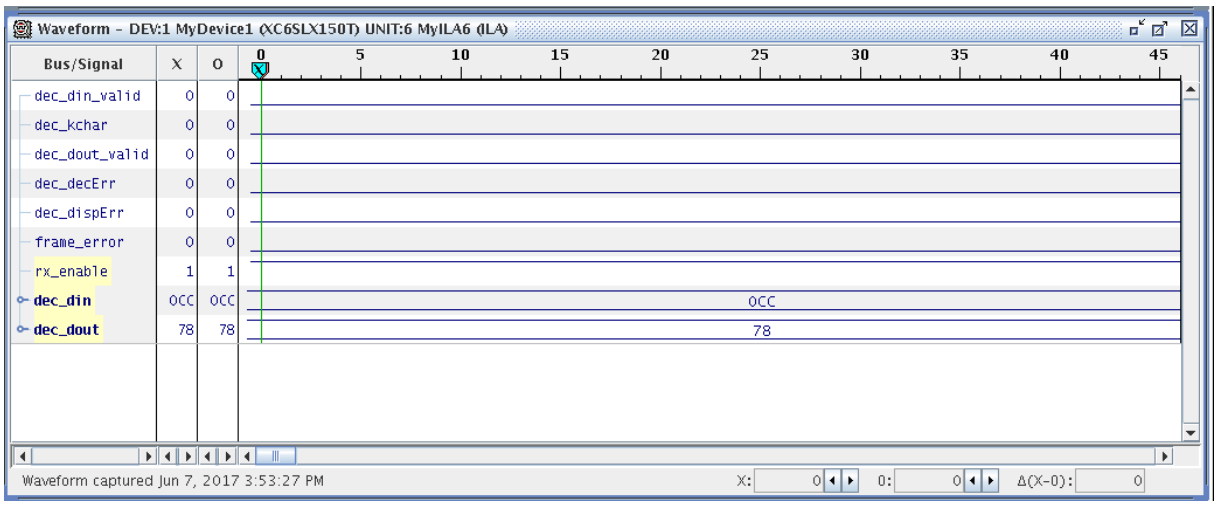

Figure A.8.: A `Chipscope` output showing a non-idle pattern from the broken module.

scopes, the available states are `OFF`; `LV_ON`, if the low voltage for the front-end chips is turned on; `STANDBY`, if the low voltage for the front-end chips is turned on and the modules are configured with preamps off (differentiated from the prior state by the current consumption); `ON`, if the modules are configured with preamps off and the high voltage for sensor biasing is turned on; and `READY`, if the high voltage is on and modules are configured with preamps on, i.e. they are ready for data taking (again, differentiated from `ON` by the current consumption).

All alerts except for `OK` are displayed on the error display of the ATLAS-ID shifter in the *ATLAS Control Room* (ACR).

The alert and state limits of the FSM can be set in a GUI, which is directly accessible

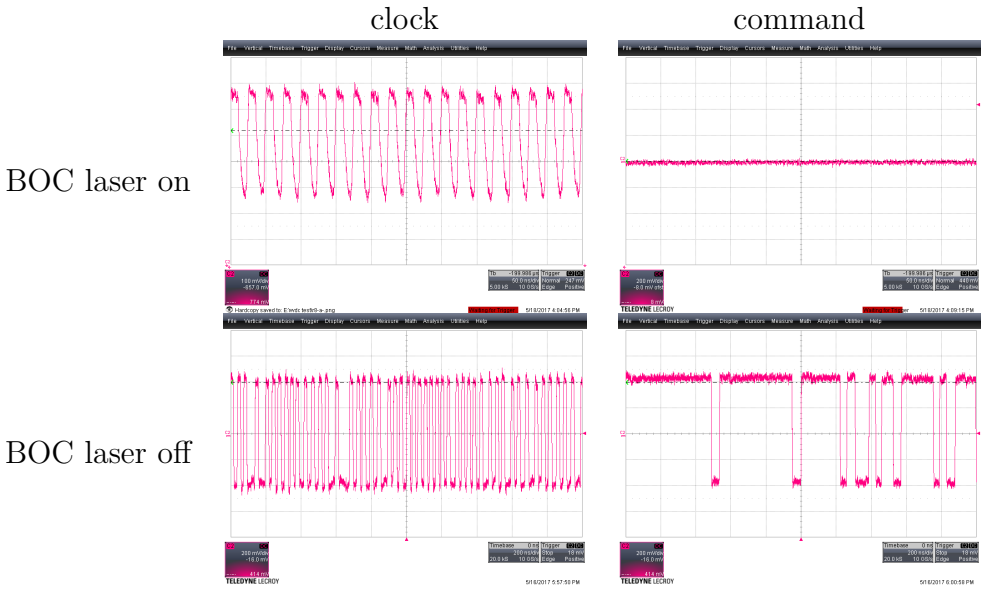

Figure A.9.: Output of a clock- and command-line for the BOC laser being on and off.

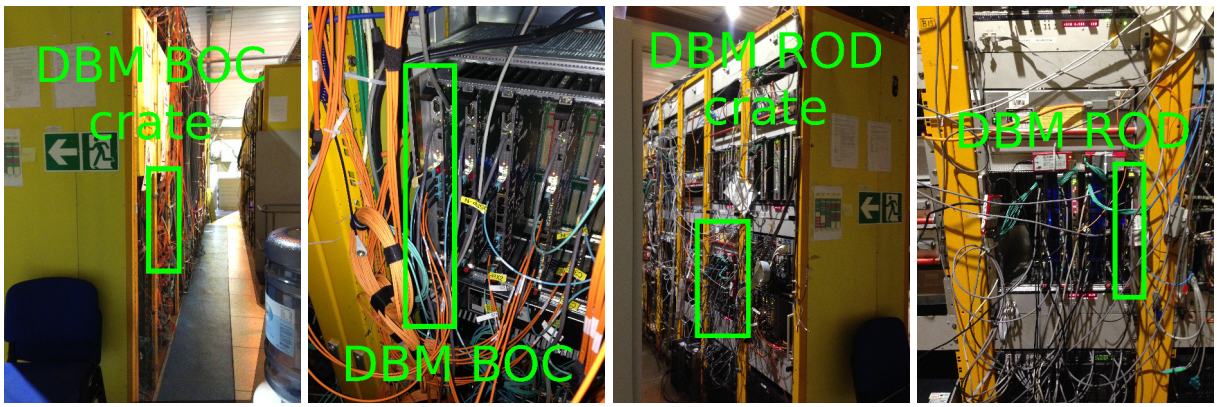

(a) *(b)* *(c)* *(d)*

Figure A.10.: The location of the BOC and the ROD of the DBM in SR1.

via the FSM now, making adjustments more flexible.

To prevent dangerous situations for the DBM inside of ATLAS, two software interlocks, a DCS watchdog and the FSM alerts, were installed. Such a situation could be the BOC laser, transmitting data to the opto-board, failing. The functionality of large parts of both safety instruments was verified during recommissioning in SR1 and in ATLAS.

DAQ Integration

The hitbus chip voltages that telescope C-M2 was tested with during the module tests are 1 V, 1.5 V and 1.6 V.

Operation

At the beginning/end of every ATLAS run, the high-voltage of the DBM has to be turned on/off. This was automated.

LTT

During the implementation and fixing of the LTT, several code modifications were carried out, mainly in `PixModuleGroup.cxx` and in the PPC code `IblScan.cxx`. The PPC code had to be modified for example to be able to run an NOS that only carries out one mask step and does no double column loops. The required files can be obtained from the author. The latest version of the NOS was saved as scan `ANALOG_TEST` with tag "Bbrueers_NOS" in SR1. The time between two triggers can be adjusted in the "Basic Par's" for an NOS, either by a field carrying the corresponding name, or by a field called "Super-grp. delay". The latest version of the LTT has the scan name `LOW_THRESH_TUNE` and tag "Base_bbrueers_noLoop0" in SR1. The LTT was modified to have a very verbose output. Therefore, the log files of the Pixel Actions Server might be very helpful for debugging or monitoring of the LTT.

Bibliography

[1] S. L. Glashow, *Partial-symmetries of weak interactions*, Nucl. Phys. **22** (1961) 579–588.

[2] S. Weinberg, *A Model of Leptons*, Phys. Rev. Lett. **19** (1967) 1264–1266.

[3] A. Salam, *Weak and Electromagnetic Interactions*, Conf. Proc. C680519 (1968) 367–377.

[4] F. Englert and R. Brout, *Broken Symmetry and the Mass of Gauge Vector Mesons*, Phys. Rev. Lett. **13** (1964) 321–322.

[5] P. W. Higgs, *Broken Symmetries, Massless Particles and Gauge Fields*, Phys. Lett. **12** (1964) 132–133.

[6] G. S. Guralnik, C. R. Hagen and T. W. B. Kibble, *Global Conservation Laws and Massless Particles*, Phys. Rev. Lett. **13** (1964) 585–587.

[7] J. Goldstone, *Field theories with «Superconductor» solutions*, Il Nuovo Cimento **19** (1961) 154–164.

[8] Y. Nambu, *Quasi-Particles and Gauge Invariance in the Theory of Superconductivity*, Phys. Rev. **117** (1960) 648–663.

[9] ATLAS Collaboration, *Observation of a new particle in the search for the Standard Model Higgs boson with the ATLAS detector at the LHC*, Phys. Lett. B **716** (2012) 1–29.

[10] CMS Collaboration, *Observation of a new boson at a mass of 125 GeV with the CMS experiment at the LHC*, Phys. Lett. B **716** (2012) 30–61.

[11] C. S. Wu et al., *Experimental Test of Parity Conservation in Beta Decay*, Phys. Rev. **105** (1957) 1413–1415.

[12] M. Goldhaber, L. Grodzins and A. W. Sunyar, *Helicity of Neutrinos*, Phys. Rev. **109** (1958) 1015–1017.

[13] J. H. Christenson et al., *Evidence for the 2π Decay of the K_2^0 Meson*, Phys. Rev. Lett. **13** (1964) 138–140.

[14] N. Cabibbo, *Unitary Symmetry and Leptonic Decays*, Phys. Rev. Lett. **10** (1963) 531–533.

[15] M. Kobayashi and T. Maskawa, *CP-Violation in the Renormalizable Theory of Weak Interaction*, Prog. Theor. Phys. **49** (1973) 652–657.

[16] C. Patrignani et al., *Review of Particle Physics*, Chin. Phys. **C40** (2016) no. 10, 100001.

[17] OPAL Collaboration, *Tests of the Standard Model and Constraints on New Physics from Measurements of Fermion-Pair Production at 189-209 GeV at LEP*, Eur. Phys. J. C **33** (2004) 173–212.

[18] LHCb Collaboration, *Observation of the Resonant Character of the $Z(4430)^-$ State*, Phys. Rev. Lett. **112** (2014) 222002.

[19] LHCb Collaboration, *Observation of $J/\psi p$ Resonances Consistent with Pentaquark States in $\Lambda_b^0 \to J/\psi K^- p$ Decays*, Phys. Rev. Lett. **115** (2015) 072001.

[20] R. L. Gluckstern, *Uncertainties in track momentum and direction, due to multiple scattering and measurement errors*, Nucl. Instr. Meth. **24** (1963) 381 – 389.

[21] W. Shockley, *Currents to Conductors Induced by a Moving Point Charge*, J. Appl. Phys. **9** (1938) 635–636.

[22] S. Ramo, *Currents Induced by Electron Motion*, Proc. IRE **27** (1939) 584–585.

[23] L. Rossi et al., *Pixel Detectors*. Springer-Verlag, Berlin; Heidelberg; New York, 2006.

[24] W. Schottky, *Über spontane Stromschwankungen in verschiedenen Elektrizitätsleitern*, Ann. Phys. (Berlin) **362** (1918) 541–567.

[25] M. Schreck et al., *Ion bombardment induced buried lateral growth: the key mechanism for the synthesis of single crystal diamond wafers*, Sci. Rep. **7** (2017) 44462.

[26] Hermann Kolanoski and Norbert Wermes, *Teilchendetektoren - Grundlagen und Anwendungen*. Springer Spektrum, 2016.

[27] J. Koike, D. M. Parkin and T. E. Mitchell, *Displacement threshold energy for type IIa diamond*, Appl. Phys. Lett. **60** (1992) 1450–1452.

[28] H. Pernegger, *High mobility diamonds and particle detectors*, Phys. Status Solidi A **203** (2006) 3299–3314.

[29] S. Zhao, *Characterization of the electrical properties of polycrystalline diamond films.* PhD thesis, Ohio State University, ocm31792981, 1994.

[30] J.-W. Tsung et al., *Signal and noise of diamond pixel detectors at high radiation fluences*, JINST **7** (2012) no. 09, P09009.

[31] L. Evans and P. Bryant, *LHC Machine*, JINST **3** (2008) no. 08, S08001.

[32] R. Aßmann, M. Lamont and S. Myers, *A brief history of the LEP collider*, Nucl. Phys. B (Proc. Suppl.) **109** (2002) 17–31.

[33] ATLAS Collaboration, *The ATLAS Experiment at the CERN Large Hadron Collider*, JINST **3** (2008) no. 08, S08003.

[34] CMS Collaboration, *The CMS experiment at the CERN LHC*, JINST **3** (2008) no. 08, S08004.

[35] ALICE Collaboration, *The ALICE experiment at the CERN LHC*, JINST **3** (2008) no. 08, S08002.

[36] LHCb Collaboration, *The LHCb Detector at the LHC*, JINST **3** (2008) no. 08, S08005.

[37] M. Lamont, *Status of the LHC*, J. Phys. Conf. Ser. **455** (2013) no. 1, 012001.

[38] V. Cindro et al., *The ATLAS Beam Conditions Monitor*, JINST **3** (2008) no. 02, P02004.

[39] H. Kagan, M. Mikuz and W. Trischuk, *ATLAS Diamond Beam Monitor (DBM)*, Tech. Rep. ATL-IP-ES-0187, CERN, 2012.

[40] ATLAS Collaboration, *ATLAS Insertable B-Layer Technical Design Report*, Tech. Rep. CERN-LHCC-2010-013, CERN, 2010.

[41] H. Frais-Kolbl et al., *A fast low-noise charged-particle CVD diamond detector*, IEEE Trans. Nucl. Sci. **51** (2004) 3833–3837.

[42] S. Schramm, *The ATLAS Detector: Status and Performance in Run-II*, Int. J. Mod. Phys. Conf. Ser. **43** (2016) 1660195.

[43] O. Viazlo, *ATLAS LUCID detector upgrade for LHC Run 2*, The European Physical Society Conference on High Energy Physics (2015).

[44] ATLAS Collaboration, *Luminosity determination in pp collisions at* $\sqrt{s} = 7$ *TeV using the ATLAS detector at the LHC*, Eur. Phys. J. C **71** (2011) 1630.

[45] ATLAS Collaboration, *Luminosity Public Results Run 2*, `https://twiki.cern.ch/twiki/bin/view/AtlasPublic/LuminosityPublicResultsRun2`. Website, accessed on the 30th January 2018.

[46] M. Červ, *The ATLAS Diamond Beam Monitor*, JINST **9** (2014) no. 02, C02026.

[47] W. Trischuk, *Diamond Particle Detectors for High Energy Physics*, Nucl. Part. Phys. Proc. **273** (2016) 1023–1028.

[48] D. M. Schaefer, *The ATLAS Diamond Beam Monitor: Luminosity detector at the LHC*, Nucl. Instr. Meth. Phys. Res. A **824** (2016) 459–461.

[49] M.L. Mangano in *Proceedings of the LHC Lumi Days, CERN-Proceedings-2011-001*, H. Burkhardt et al., eds., pp. 1–5. Geneva, Switzerland, Jan., 2011.

[50] A. J. Edwards et al., *Radiation monitoring with CVD diamonds in BABAR*, Nucl. Instr. Meth. Phys. Res. A **552** (2005) 176–182.

[51] M. Barbero et al., *Submission of the first full scale prototype chip for upgraded ATLAS pixel detector at LHC, FE-I4A*, Nucl. Instr. Meth. Phys. Res. A **650** (2011) 111–114.

[52] D. S. Smith et al., *Development of the hitbus chip platform for the ATLAS DBM detector at CERN*, in *2013 IEEE 56th International Midwest Symposium on Circuits and Systems (MWSCAS)*, pp. 1204–1207. Aug., 2013.

[53] A. Polini et al., *Design of the ATLAS IBL Readout System*, Phys. Procedia **37** (2012) 1948–1955.

[54] ATLAS Collaboration, *FFTV for IBL*, `https://twiki.cern.ch/twiki/bin/view/Atlas/FFTVforIBL`. Website, accessed on the 31st January 2018.

[55] M. Backhaus et al., *Development of a versatile and modular test system for ATLAS hybrid pixel detectors*, Nucl. Instr. Meth. Phys. Res. A **650** (2011) 37–40.

[56] A. La Rosa on behalf of the ATLAS collaboration, *The ATLAS Insertable B-Layer: from construction to operation*, JINST **11** (2016) no. 12, C12036.

[57] K. Dette, *Total Ionising Dose effects in the FE-I4 front-end chip of the ATLAS Pixel IBL detector*, JINST **11** (2016) no. 11, C11028.

[58] ATLAS Collaboration, *Radiation induced effects in the* ATLAS *Insertable B-Layer readout chip*, Tech. Rep. ATL-INDET-PUB-2017-001, CERN, 2017.

[59] F. Faccio and G. Cervelli, *Radiation-induced edge effects in deep submicron CMOS transistors*, IEEE Trans. Nucl. Sci. **52** (2005) 2413–2420.

[60] M. Backhaus, *Parametrization of the radiation induced leakage current increase of NMOS transistors*, JINST **12** (2017) no. 01, P01011.

[61] ATLAS Collaboration, *Radiation Background Simulations Run 2*, `https://twiki.cern.ch/twiki/bin/view/Atlas/RadiationBackgroundSimulationsRun2`. Website, accessed on the 31st January 2018.

[62] J. Janssen, *Test beam results of ATLAS DBM pCVD diamond detectors using a novel threshold tuning method*, JINST **12** (2017) no. 03, C03072.

[63] M. Mironova, *Implementation of a Threshold Tuning Algorithm for Silicon and Diamond Pixel Detectors*. Bachelor's thesis, Universität Göttingen, II. Physik-UniGö-BSc-2017/02, 2017.

[64] K. C. Chen et al., *Conductor Fusing and Gapping for Bond Wires*, Prog. Electromagn. Res. M **31** (2013) 199–214.

[65] J. D. Huff et al., *1 Mil Gold Bond Wire Study*, Tech. Rep. SAND2013-3715, SANDIA, 2013.

[66] D. Alvarez Feito, A. Honma and B. Mandelli, *Studies of IBL wire bonds operation in a ATLAS-like magnetic field.*, Tech. Rep. PH-EP-Tech-Note-2015-002, CERN, 2015.

[67] FE-I4 Collaboration, *The FE-I4B Integrated Ciruit Guide Version 2.3*, `https://indico.cern.ch/event/261840/contributions/1594374/attachments/462649/641213/FE-I4B_V2.3.pdf`. Website, accessed on the 1st February 2018.

Acknowledgements

There a very many people that accompanied me on my way through my Master's degree. First of all I would like to thank my parents for being so understanding, supportive and critical and enabling me to study.

I would like to thank Prof. Dr. Arnulf Quadt for offering me this Master's thesis topic and the opportunity to go to CERN and to spend the first 5 month of my thesis time there to work on my project. I am further grateful for the critical comments and questions throughout my thesis time, which helped to improve my work. Finally, I would like to say thank you for the support in several other occasions such as when applying to be a summer student, when going to Helsinki as an ERASMUS student or just during the every day life in the institute.

Thank you to Priv.Doz. Dr. Jörn Große-Knetter for being my second referee and for having very helpful advice in multiple occasions, in particular when it came to debugging the Low Threshold Tuning.

Without the clear mind, structured approach, high motivation and patients of Jens, my thesis would have never turned out the way it did. Thank you so much for your support and availability, also when I was at CERN and for the very valuable proofreading of my thesis.

Thank you Clara for proofreading not only parts of my Master's thesis, but also previous documents. Your feedback was very helpful indeed.

I would like to thank the various institute members, Helge and Erik, for the support in the lab, Tobias for being my office mate, for making me retest my assumptions and for helping me with making wirebond oscillations visible with the WTF board. Thank you Andreas and Diogo, for being my office mates and for the intense discussions concerning Particle Physics and loads of other topics. Thank you Fabian, for all the Pixel DAQ discussions. Thank you Benedikt for spending multiple coffee breaks together and for talking about everything. Thank you also to all others, which I did not explicitly mention.

Big thanks go to Kevin Adener for making the construction of the WTF board possible.

I would like to thank Andreas König, who helped me in constructing some parts for my experiments in Göttingen. I will always remember you as a kind, fair and motivated fellow,

just having the best for your students in mind. One of the last things you told me was that our institute would be the last professional address of your life, whether you retired or whatever else would happen. You certainly were right on that one, unfortunately.

Thank you to the DBM team for all your support, to Nicola and Enrico, for supervising me at CERN, to William and Marco for their input and to Bostjan and Grygorii for their help in multiple occasions. I would also like to thank the ATLAS Pixel IBL DAQ experts, who helped me a lot during recommissioning and operation of the DBM, thank you Marcello, Chris, JuanAn, PF, Alex, Kerstin, Martin, Didier and anyone who I might have forgotten. Without you, this would have not been possible! Thank you to Irmtraut, for putting up with me all the time while I lived in Geneva. Thank you Felix, Jacobus, Miko, Matteo, Silke, Oliver, Victoria and all the others for the skiing, climbing and just making my free time at CERN so much more fun. You certainly are some cool people!

A big thank you goes to all my fellow students who discussed, corrected, answered all my questions or just spent time with me and enriched the time. Finally, thank you to everyone else who made me come this far, it would have not gone without you!

Erklärung nach §17(9) der Prüfungsordnung für den Bachelor-Studiengang Physik und den Master-Studiengang Physik an der Universität Göttingen:

Hiermit erkläre ich, dass ich diese Abschlussarbeit selbständig verfasst habe, keine anderen als die angegebenen Quellen und Hilfsmittel benutzt habe und alle Stellen, die wörtlich oder sinngemäß aus veröffentlichten Schriften entnommen wurden, als solche kenntlich gemacht habe.
Darüberhinaus erkläre ich, dass diese Abschlussarbeit nicht, auch nicht auszugsweise, im Rahmen einer nichtbestandenen Prüfung an dieser oder einer anderen Hochschule eingereicht wurde.

Göttingen, den 20. März 2018

(Ben Brüers)